Low-Temperature Synthesis, Thermodynamic Properties, and Electrical Conduction Properties of Lanthanum Phosphates

by

Naoyuki Hatada

Department of Materials Science and Engineering
Kyoto University

2012

Contents

Chapter 1
General Introduction

Recently significant research efforts have been made to develop fuel cells operating at intermediate temperatures (200–750 °C) [1-3]. This temperature range may allow for the use of non-precious metal catalysts and eliminate the need for external reforming of fuels. It may also allow for the use of less expensive components and facilitate miniaturization. Several types of phosphate based proton conductors such as ammonium polyphosphates, pyrophosphates, and cesium phosphates have been proposed for use as electrolytes in intermediate-temperature fuel cells [3]. They exhibit proton conductivities greater than 10^{-2} S cm^{-1} at their operating temperatures. Nevertheless, there are several problems left to be solved, such as thermal decomposition at relatively low temperatures (~300 °C), mechanical instability, and water solubility.

In contrast, rare earth phosphates are attracting much attention due to their proton conduction and high-temperature chemical stability. However, further enhancement of the conductivity is still required for technological applications, while their proton conduction mechanisms are yet to be clarified. Also, knowledge regarding their optimum synthesis conditions and stabilities is insufficient. In this context, this work has focused on a comprehensive characterization of lanthanum phosphates with the objective of providing the fundamental information for developing new lanthanum-phosphate-based electrolytes for practical use. Systematic investigations were carried out on their optimum synthesis conditions, thermodynamic properties, and proton conduction properties. In this chapter, a brief overview of related work is provided.

1.1 Proton Conduction in Rare Earth Phosphates

Several rare earth phosphates doped with acceptors such as Sr have been shown to have proton conduction in the intermediate temperature range since the first report by Norby and Christiansen [4] in 1995. Norby and Christiansen showed that Ca- or Sr-doped $LaPO_4$ exhibits proton conductivities on the order of 10^{-4} S cm^{-1} at ~700 °C in wet air while those of undoped $LaPO_4$ are ~10^{-5} S cm^{-1}. Later, proton conduction was also found in many rare earth phosphates such as *RE*PO_4 (*RE*=Y, La, Ce, Pr, Nd, Sm) [5-8], $La_7P_3O_{18}$ [9], LaP_3O_9 [10], LaP_5O_{14} [11], and Nd_3PO_7 [12] doped with acceptors. A number of studies have been carried out to date on various aspects of the proton conduction behavior in these phosphates, especially *RE*PO_4 and LaP_3O_9. In these studies, $LaPO_4$ was found to be the most preferable host lattice among *RE*PO_4 in terms of the proton conductivity [5-7]. Similarly, Sr was found to be the best dopant among alkaline earth metals for $LaPO_4$ [13] and LaP_3O_9 [14]. Figure 1.1 presents the highest conductivities of each Sr-doped lanthanum phosphate reported so far. The conductivities increase in the order of $La_7P_3O_{18}$ < $LaPO_4$ < LaP_5O_{14} < LaP_3O_9, reaching 2 × 10^{-4} S cm^{-1} at 600 °C, though further improvement to ~10^{-2} S cm^{-1} will be required for practical applications.

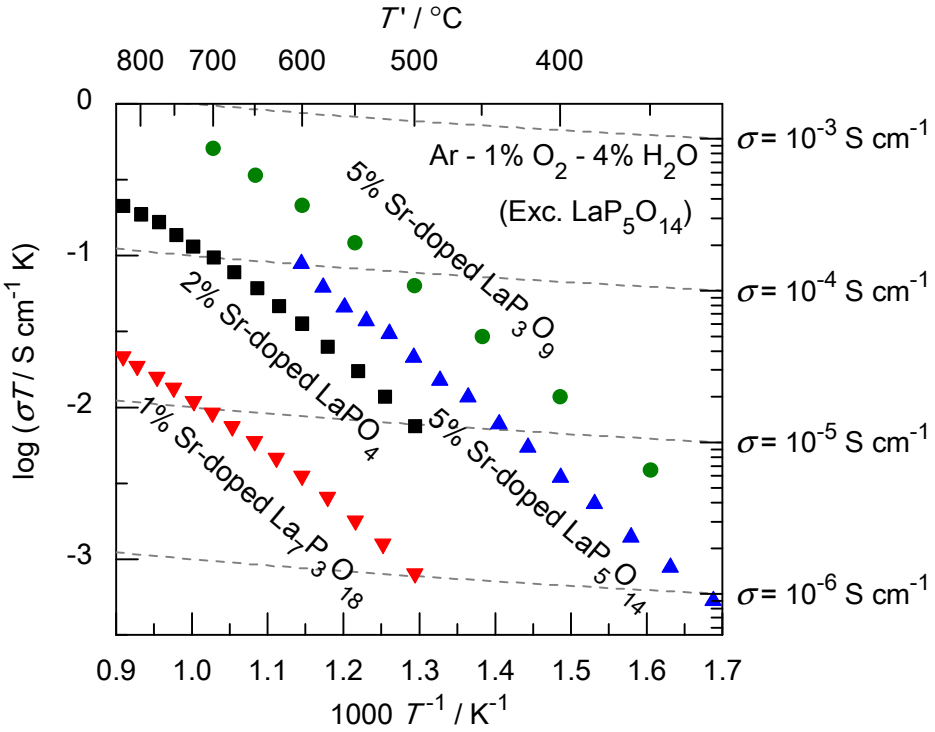

Figure 1.1 Electric conductivities of Sr-doped $La_7P_3O_{18}$ [9], $LaPO_4$ [15], LaP_3O_9 [16], and LaP_5O_{14} [17] as a function of reciprocal temperature.

1.1.1 Proton Conduction Mechanism

The defect structures in Sr-doped $LaPO_4$ were investigated by Amezawa *et al.* using conductivity, MAS-NMR spectroscopy and FT-Raman spectroscopy measurements [18]. Based on the results, they proposed the following proton incorporation mechanism into Sr-doped $LaPO_4$. When La is partially substituted with Sr, pyrophosphate ions written as $(P_2O_7)^{\bullet\bullet}_{2PO_4}$ are formed by condensation of orthophosphate ions as shown in Eq. (1.1).

$$\frac{1}{2}Sr_2P_2O_7 \rightarrow Sr'_{La} + \frac{1}{2}(P_2O_7)^{\bullet\bullet}_{2PO_4} \qquad (1.1)$$

Then protons can be incorporated into $LaPO_4$ from water vapor, forming hydrogen phosphate groups, $(HPO_4)^{\bullet\bullet}_{PO_4}$, as shown in Eq. (1.2).

$$\frac{1}{2}(P_2O_7)^{\bullet\bullet}_{2PO_4} + \frac{1}{2}H_2O(g) \rightleftharpoons (HPO_4)^{\bullet\bullet}_{PO_4} \qquad (1.2)$$

$$K = \frac{\left[(\mathrm{HPO_4})^{\bullet}_{\mathrm{PO_4}}\right]}{\left[(\mathrm{P_2O_7})^{\bullet\bullet}_{\mathrm{2PO_4}}\right]^{1/2} p\,(\mathrm{H_2O})^{1/2}} \tag{1.3}$$

Based on this mechanism, the proton concentration in $LaPO_4$ is determined by the equilibrium between the intrinsic positive effects and water vapor in the ambient atmosphere (Eq. (1.3)). As shown in Figure 1.2, it was observed that the electric conductivity of Sr-doped $LaPO_4$,as well as that of Sr-doped $La_7P_3O_{18}$, increased with increasing water vapor pressure. This dependency agrees well with the proposed proton incorporation mechanism.

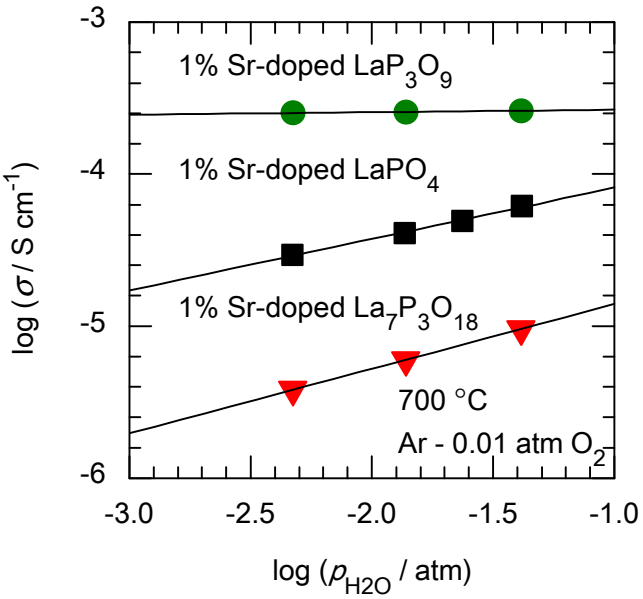

Figure 1.2 Water vapor pressure dependence of the conductivities of 1% Sr-doped $La_7P_3O_{18}$ [9], $LaPO_4$ [7], LaP_3O_9 [10].

On the other hand, Sr-doped LaP_3O_9 does not follow the rule, for its conductivity is almost independent of water vapor pressure. In addition, it is also difficult to apply the defect structure model described above directly to Sr-doped LaP_3O_9 from the viewpoint of crystal structure. Figure 1.3 shows the crystal structures of undoped $LaPO_4$ (monazite type) and LaP_3O_9. In the $LaPO_4$ lattice, the constituent PO_4 tetrahedra are isolated, and they are supposed to form dimers (P_2O_7) only when La is partially substituted with divalent dopants. It is reasonable to assume that $La_7P_3O_{18}$ also has

isolated PO_4 tetrahedra considering its La/P ratio, though the crystal structure of $La_7P_3O_{18}$ has not been reported so far. In contrast, the PO_4 tetrahedra in undoped LaP_3O_9 are already linked in chains along the c-axis in nature. LaP_5O_{14} was also reported to have cross-linking PO_4 chains [19]. Therefore, the defect structures proposed for $LaPO_4$ cannot be applied to LaP_3O_9 and LaP_5O_{14} without appropriate modification.

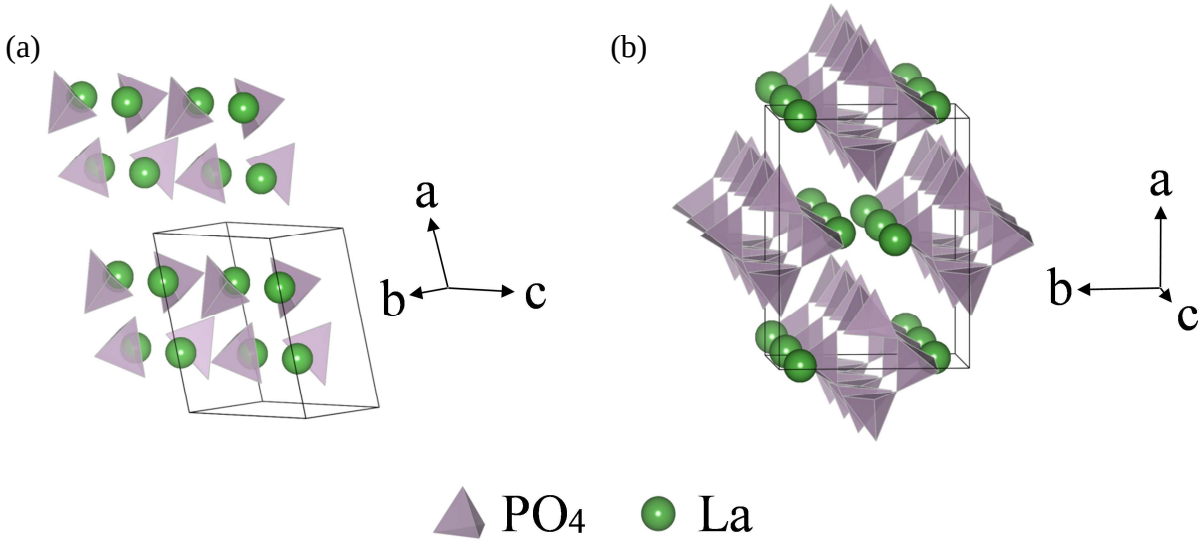

Figure 1.3 Structural arrangements of (a) undoped $LaPO_4$ (monazite type) [20] and (b) undoped LaP_3O_9 [21]. PO_4 groups in the crystal structures are shown as tetrahedra.

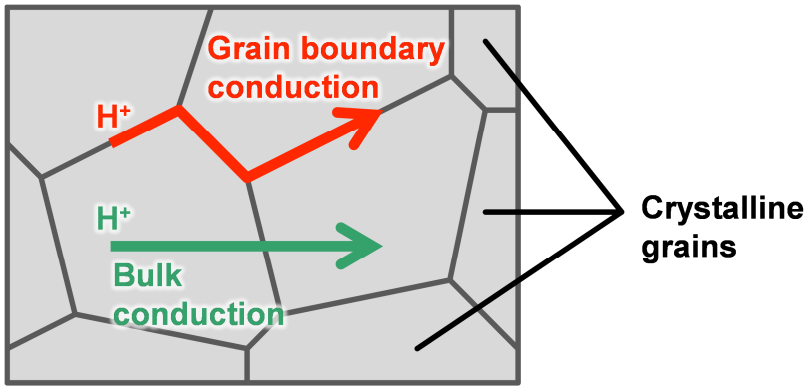

Figure 1.4 Schematic illustration of the proton transport paths in polycrystalline solid electrolytes.

Besides the defect structures, the proton conduction paths in undoped $LaPO_4$ have been studied

by several authors. Figure 1.4 schematically represents the two types of proton conduction paths in solid electrolytes. Jørgensen *et al*. observed that a part of phosphate excess during synthesis remained in the surfaces of $LaPO_4$ samples after sintering [22]. They suggested that the phosphorus-rich grain boundaries may enhance the proton conductivity. Harley *et al*. also reported the formation of phosphorus-rich amorphous grain boundary film by sintering of $LaPO_4$, because of residual hydrogen-phosphate-type compounds remaining from synthesis via precipitation in aqueous solutions [23]. The grain boundary conductivity was calculated to be as high as ~2.5×10^{-3} S cm^{-1} at 500 °C, from the analysis of the experimental conductivity data of the samples using the 'bricklayer' model. To demonstrate the effect of the presence of high conductivity grain boundary films further, they also investigated the conduction properties of a mixture of $LaPO_4$ – 15 mol% LaP_3O_9. The sample was heat treated at 1300 °C (higher than the melting temperature of LaP_3O_9) to form amorphous grain boundary film. The conductivity of the sample was measured before and after the heat treatment, and the increase in conductivity was observed with the appearance of the amorphous phases. Their work suggests that the grain boundaries provide the dominant proton conduction paths in $LaPO_4$. In contrast, theoretical calculations on the proton-transfer mechanism in $LaPO_4$ suggested there are proton transport paths in the $LaPO_4$ lattice with energy barrier of ~0.8 eV, close to experimentally measured activation energies [24]. Additionally, the above mentioned experimental work also suggests that amorphous LaP_3O_9 has higher conductivity than that of crystalline LaP_3O_9. However, the investigation of the conduction properties of LaP_3O_9 glass revealed the opposite behavior [25]. The conductivity of the Sr-doped LaP_3O_9 glass significantly increased with the crystallization, while that of the undoped LaP_3O_9 glass remained unchanged.

Taking into account these inconsistencies, it can be said that the proton conduction mechanisms in lanthanum phosphates, especially condensed ones (LaP_3O_9 and LaP_5O_{14}) have not been understood at all. Clarifying them will be highly desired for improving the proton conductivities in lanthanum phosphates. For example, if the dominant proton transport paths are determined, it will be

possible to improve the proton conductivities of lanthanum phosphates by synthesizing samples with desired micro structures (fine- or coarse-grained polycrystalline samples or single crystals).

1.1.2 Solubility of Sr in $LaPO_4$ and LaP_3O_9

As described above, the proton conduction in lanthanum phosphates is generated by doping divalent cations such as Sr. Therefore, it will be important to make the most of the doping effect for improving the proton conductivity. However, the solubilities of Sr in lanthanum phosphates have been reported to be relatively low. Amezawa *et al*. derived the solubilities of Sr in $LaPO_4$ and LaP_3O_9 by X-ray diffraction analysis and conductivity measurements in combination [15,16]. The reported solubilities of Sr, represented by the molar ratio Sr/(La+Sr) are ~2 mol% in $LaPO_4$ and below 5 mol% in LaP_3O_9. As shown in Figure 1.5, the conductivities of Sr-doped $LaPO_4$ and LaP_3O_9 increase with increasing the Sr concentration within the concentration range below the solubilities. However, with higher Sr mixing ratios, secondary phases, $Sr_2P_2O_7$ and $Sr(PO_3)_2$, appeared and the conductivities cease to increase or begin to deteriorate. Thus, the low solubilities of Sr are an obstacle to enhancing the conductivities of lanthanum phosphates.

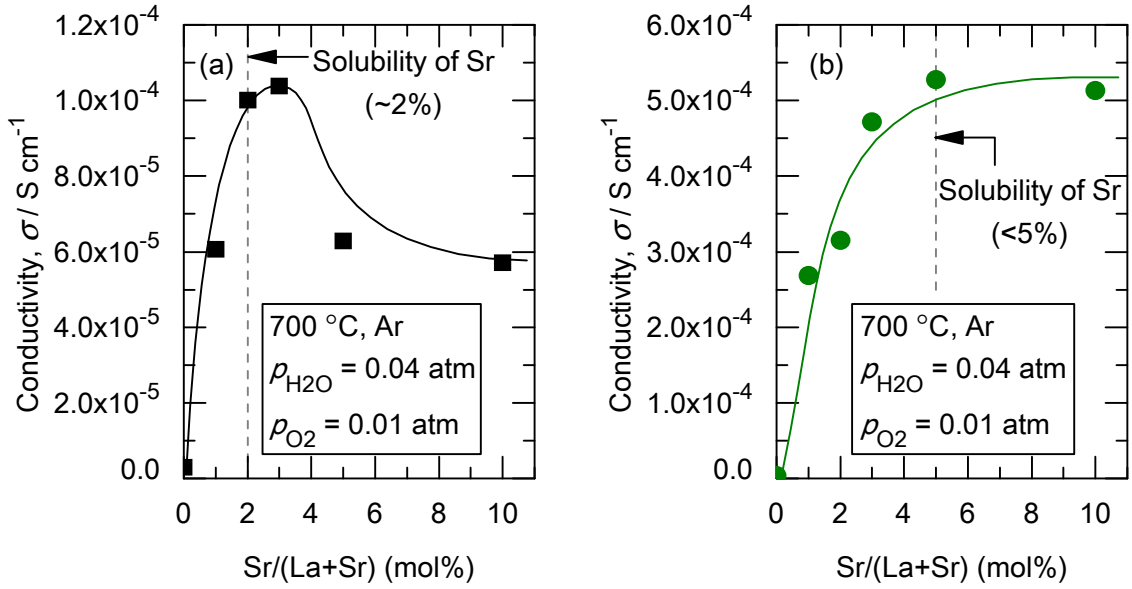

Figure 1.5 Conductivities of (a) Sr-doped $LaPO_4$ [15] and (b) Sr-doped LaP_3O_9 [16] as a function of the Sr-doping level.

While the above mentioned study on $LaPO_4$ was conducted with samples prepared by solid state reaction and sintered at 1200 °C [15], there are several reports of different Sr doping levels with different synthesis temperatures (Table 1.1). Tyholdt *et al*. reported the solubility of Sr in $LaPO_4$ to be ~1% using samples sintered at 1450 °C [26]. Gallini *et al*. prepared 5% Sr-doped $LaPO_4$ by combustion synthesis followed by calcination at 800 °C [27]. Schatzmann *et al*. synthesized Sr-doped $LaPO_4$ by adding $La(NO_3)_3{\cdot}6H_2O$ and $Sr(NO_3)_2$ to heated phosphoric acid at 150 °C, followed by precipitation of $LaPO_4$ within 30 minutes [28]. With this method, at least 4% Sr-doped $LaPO_4$ was obtained. These results suggest that the solubility of Sr would be higher at lower temperatures. Therefore, to obtain highly Sr-doped lanthanum phosphates, the development and optimization of synthesis methods avoiding high temperature heat treatments might be beneficial.

Table 1.1 Sr-doping levels in $LaPO_4$ attained at various synthesis temperatures.

Synthesis method	Max. temp. / °C	Sr-doping level (mol%)	Ref.
Solid state reaction	1450	~1	[26]
Solid state reaction	1200	~2	[15]
Combustion synthesis	800	5	[27]
Precipitation in hot phosphoric acid	150	≥ 4	[28]

1.2 Phase equilibria in the La_2O_3–P_2O_5 System and Stabilities of Lanthanum Phosphates

Various phosphates in the La_2O_3–P_2O_5 system have been studied not only as proton conductors, but also as laser and luminescent materials [29-32], phosphorus diffusion sources for semiconductors [33-35], debond materials in oxide composites [36], coating materials [37], and radioactive waste forms [38,39]. The information on the phase equilibria in the La_2O_3–P_2O_5 serves as the basic knowledge needed for synthesizing various lanthanum phosphates as well as assessing their stabilities and reactivity with other materials. Two phase diagrams have so far been reported for the La_2O_3–P_2O_5 system as shown in Figure 1.6 [40,41]. However, there are considerable differences in the compounds present. For example, one of the proton conductors referred to in the previous section, $La_7P_3O_{18}$, is only present in the phase diagram by Park and Kreidler [40]. Therefore, further inspection should be necessary on the existance and stability of $La_7P_3O_{18}$. In addition, LaP_3O_9 and LaP_5O_{14} have been demonstrated to decompose gradually at high temperatures by the following reactions [10,40,42-44]:

$$LaP_3O_9\ (s) \rightarrow LaPO_4\ (s) + 1/2\ P_4O_{10}\ (g); \quad (1.4)$$

$$LaP_5O_{14}\ (s) \rightarrow LaP_3O_9\ (s) + 1/2\ P_4O_{10}\ (g). \quad (1.5)$$

The decomposition temperatures have been reported to be ~800 °C [10] and ~700 °C [42], respectively. Because of these decompositions, it is difficult to obtain dense LaP_3O_9 and LaP_5O_{14} electrolytes by conventional sintering method. In fact, dense LaP_3O_9 samples with relative density

higher than 0.9 have only been obtained by spark plasma sintering [10]. Moreover, the instability of LaP_3O_9 and LaP_5O_{14} may limit the operating temperatures for the electrolytes, since the decomposition of the electrolytes during fuel cell operation may lead to the degradation of cell performance as well as corrosion of other components. However, very little quantitative information is available about the decomposition reactions. The only available experimental information, the vapor pressure of P_4O_{10} (p_{P4O10}) over LaP_3O_9, was given by Ashuiko *et al*. [44] as follows:

$$\log (p_{P4O10} / \text{mmHg}) = 8.5641 - 13613 \times (T / \text{K})^{-1}$$

$$(1219 \leq T / \text{K} \leq 1404). \qquad (1.6)$$

For accurate assessment of the stabilities of LaP_3O_9 and LaP_5O_{14}, further examination and refinement of their thermodynamic properties will be required.

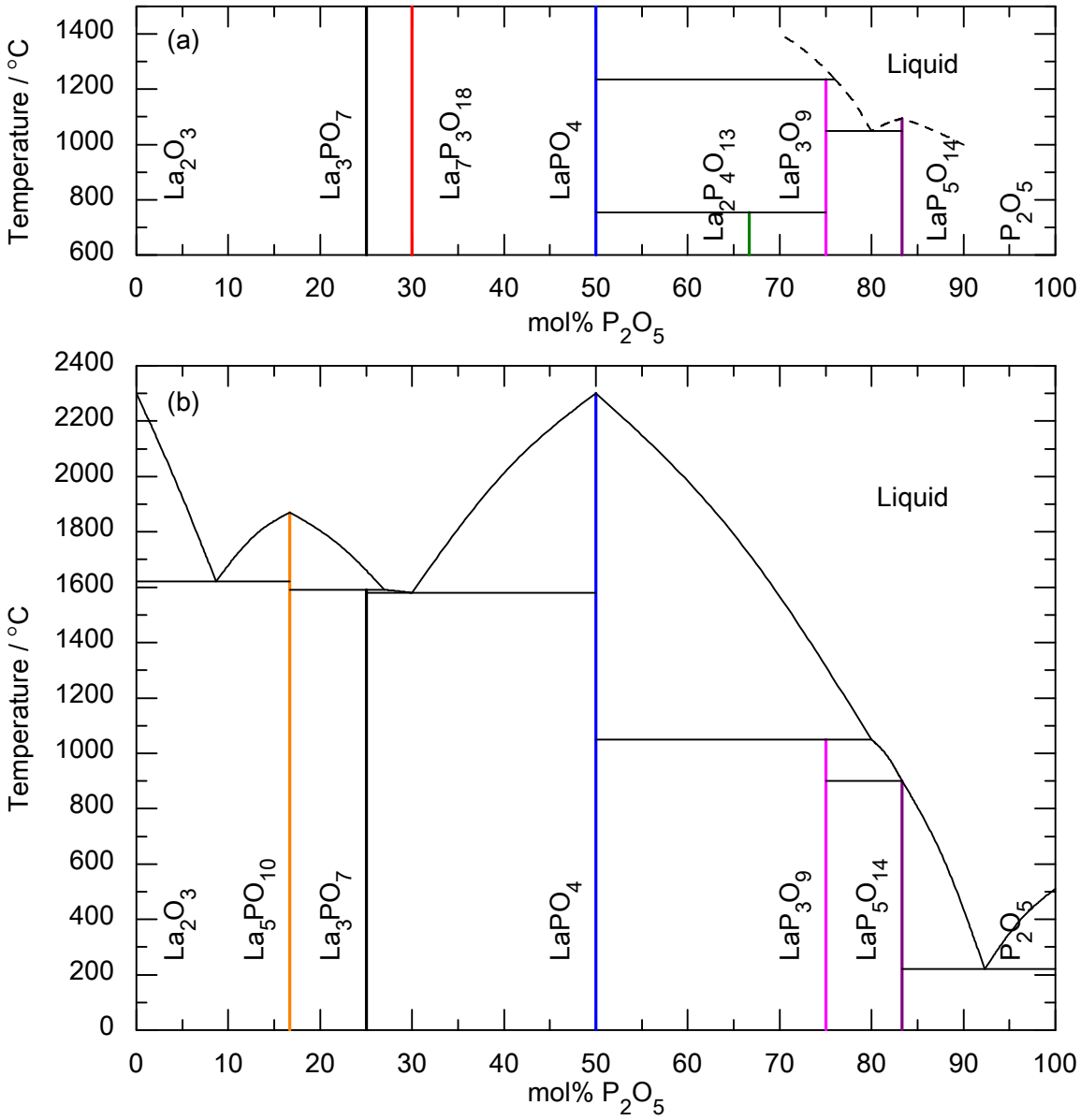

Figure 1.6 Phase diagrams of the La_2O_3–P_2O_5 system presented by (a) Park and Kreidler [40] and (b) Kropiwnicka and Znamierowska [41]. Solid-solid phase transitions are not shown for simplification.

1.3 Synthesis Methods of Lanthanum Phosphates

As referred to in section 1.1, selection and development of appropriate synthesis methods will be a key to understanding the proton conduction mechanisms and improving the proton conductivity in lanthanum phosphates. In this work, most of lanthanum phosphate samples were prepared by

precipitation in condensed phosphoric acid solutions. Here, a brief description of the synthesis methods of rare earth phosphates is provided.

Rare earth phosphates have been synthesized *via* a variety of methods such as precipitation in aqueous solutions [45-47], precipitation in condensed phosphoric acid solutions [48,49], hydrothermal synthesis [50-52], solid state reaction [53,54], flux growth [55-57], and chemical transportation [58]. The solid state reaction or the precipitation in aqueous solutions followed by calcination have been widely used to synthesize lanthanum phosphate samples for investigating their conduction properties. By these methods, it is relatively easy to obtain polycrystalline lanthanum phosphates. It is also possible to obtain Sr-doped samples by adding Sr-containing compounds such as $SrCO_3$ to starting materials. However, it is difficult to achieve desired grain sizes, especially larger size by these methods. In addition, high temperature heat treatments are inevitable which may lower the solubility of Sr.

On the other hand, large single crystals of rare earth phosphates have been obtained by precipitation in condensed phosphoric acid solutions, hydrothermal synthesis, flux growth, and chemical transportation. Among them, the precipitation in condensed phosphoric acid solutions can be performed with relatively simple apparatus and at lower temperatures. It has been extensively investigated for synthesizing single crystals of rare earth ultraphosphates (REP_5O_{14}) for the purpose of using them as laser materials [48,49,59-63]. The common procedure of this method can be stated as follows: A mixture of rare earth oxide and phosphoric acid is heated to several hundred degrees Celsius (*e.g.* 300 °C) to dissolve the oxide into phosphoric acid completely; Then the solution is heated up to higher temperatures (*e.g.* 500 °C) to precipitate REP_5O_{14}. With this method, single crystals of NdP_5O_{14} with size more than 3 cm were obtained [49]. Through related works, it was found that $LaPO_4$ and LaP_3O_9 precipitate at temperatures below ~300 °C [64-66]. According to Chudinova, however, it is difficult to obtain LaP_3O_9 because the temperature range of precipitation is only 50 °C [67]. Byrappa also stated that the process of formation of ortho- and polyphosphates

(*RE*PO_4 and *RE*P_3O_9) is very slow at temperatures lower than 260 °C and it is rather difficult to carry out the synthesis [68]. Nevertheless, there may be room for further improvement since the literature focusing on the precipitation behavior of $LaPO_4$ and LaP_3O_9 in condensed phosphoric acid solutions is still scarce.

1.4 Outline of This Work

In the above context, the synthesis conditions, thermodynamic properties and electrical conduction properties of lanthanum phosphates were studied throughout this work.

In Chapter 2, the precipitation conditions of $LaPO_4$, LaP_3O_9 and LaP_5O_{14} in phosphoric acid solutions were investigated in both ambient and humidified atmospheres. The morphology of precipitates was analyzed in relation to the precipitation condition.

In Chapter 3, the phase equilibria in the La_2O_3–P_2O_5 system were re-examined to resolve the differences in the reported phase diagrams.

In Chapter 4, thermodynamic measurements were carried out on LaP_3O_9 and LaP_5O_{14} by transpiration method. The thermal stabilities of LaP_3O_9 and LaP_5O_{14} were discussed using the obtained results.

In Chapter 5, synthesis of Sr-doped $LaPO_4$ and LaP_3O_9 was carried out in phosphoric acid solutions. The optimum conditions for obtaining highly Sr-doped $LaPO_4$ and LaP_3O_9 were revealed. It was confirmed that H_2O is certainly incorporated in the bulk by Sr doping.

In Chapter 6, direct synthesis of dense, polycrystalline Sr-doped $LaPO_4$ and LaP_3O_9 electrolytes was performed in phosphoric acid solutions. Single crystals of Sr-doped LaP_3O_9 were also synthesized. The electrical conduction properties of the precipitates were investigated by impedance spectroscopy.

In Chapter 7, a brief summary of this study is provided.

References

[1] T. Norby, Solid State Ionics 125 (1999) 1-11.

[2] D.J.L. Brett, A. Atkinson, N.P. Brandon, S.J. Skinner, Chem. Soc. Rev. 37 (2008) 1568-1578.

[3] O. Paschos, J. Kunze, U. Stimming, F. Maglia, J. Phys.: Condens. Matter 23 (2011) 234110.

[4] T. Norby, N. Christiansen, Solid State Ionics 77 (1995) 240-243.

[5] K. Amezawa, Y. Tomii, N. Yamamoto, Solid State Ionics 162-163 (2003) 175-180.

[6] N. Kitamura, K. Amezawa, Y. Tomii, T. Hanada, N. Yamamoto, T. Omata, S. Otsuka-Yao-Matsuo, J. Electrochem. Soc. 152 (2005) A658-A663.

[7] N. Kitamura, K. Amezawa, Y. Tomii, N. Yamamoto, Solid State Ionics 162-163 (2003) 161-165.

[8] N. Kitamura, K. Amezawa, Y. Tomii, N. Yamamoto, J. Jpn. Soc. Powder Powder Metall. 49 (2002) 856-860.

[9] K. Amezawa, Y. Tomii, N. Yamamoto, Solid State Ionics 175 (2004) 569-573.

[10] K. Amezawa, Y. Kitajima, Y. Tomii, N. Yamamoto, Electrochem. Solid-State Lett. 7 (2004) A511-A514.

[11] I. Hammas, K. Horchani-Naifer, M. Férid, J. Rare Earths 28 (2010) 321-328.

[12] A. Unemoto, K. Amezawa , T. Kawada, in: Abstracts of the 15th International Conference on Solid State Protonic Conductors, 2010, p. 69.

[13] K. Amezawa, Y. Tomii, N. Yamamoto, Solid State Ionics 176 (2005) 135-141.

[14] K. Amezawa, Y. Kitajima, Y. Tomii, N. Yamamoto, M. Widerøe, T. Norby, Solid State Ionics 176 (2005) 2867-2870.

[15] K. Amezawa, Y. Tomii, N. Yamamoto, Solid State Ionics 176 (2005) 143-148.

[16] K. Amezawa, Y. Uchimoto, Y. Tomii, Solid State Ionics 177 (2006) 2407-2411.

[17] S.R. Phadke, J.C. Nino, J. Am. Ceram. Soc. 94 (2011) 1817-1823.

[18] K. Amezawa, H. Maekawa, Y. Tomii, N. Yamamoto, Solid State Ionics 145 (2001) 233-240.

[19] J.M. Cole, M.R. Lees, J.A.K. Howard, R.J. Newport, G.A. Saunders, E. Schönherr, J. Solid State Chem. 150 (2000) 377-382.

[20] D.F. Mullica, W.O. Milligan, D.A. Grossie, G.W. Beall, L.A. Boatner, Inorg. Chim. Acta 95 (1984) 231-236.

[21] J. Matuszewski, J. Kropiwnicka, T. Znamierowska, J. Solid State Chem. 75 (1988) 285-290.

[22] S. Jørgensen, J.A. Horst, O. Dyrlie, Y. Larring, H. Ræder, T. Norby, Surf. Interface Anal. 34 (2002) 306-310.

[23] G. Harley, R. Yu, L.C. De Jonghe, Solid State Ionics 178 (2007) 769-773.

[24] R. Yu, L.C. De Jonghe, J. Phys. Chem. C 111 (2007) 11003-11007.

[25] K. Amezawa, T. Tomiga, N. Yamamoto, T. Hanada, Y. Tomii, J. Am. Ceram. Soc. 88 (2005) 3211-3214.

[26] F. Tyholdt, J.A. Horst, S. Jørgensen, T. Østvold, T. Norby, Surf. Interface Anal. 30 (2000) 95-97.

[27] S. Gallini, M. Hänsel, T. Norby, M.T. Colomer, J.R. Jurado, Solid State Ionics 162-163 (2003) 167-173.

[28] M.T. Schatzmann, M.L. Mecartney, P.E.D. Morgan, J. Mater. Chem. 19 (2009) 5720-5722.

[29] R.C. Ropp, J. Electrochem. Soc. 115 (1968) 841-845.

[30] T.C. Damen, H.P. Weber, B.C. Tofield, Appl. Phys. Lett. 23 (1973) 519-520.

[31] E.B. Stucchi, A.M. de Castro, M.A. Couto Dos Santos, P. Melnikov, J. Alloys Compd. 275-277 (1988) 86-88.

[32] S. Lu, J. Zhang, J. Lumin. 122-123 (2007) 500-502.

[33] K. Gunjigake, M. Hasegawa, H. Oizumi, Y. Ogata, United States Patent 4,033,790, July 5, 1977.

[34] G.R. Pickrell, J.E. Rapp, United States Patent 5,350,460, Sep. 27, 1994.

[35] M. Tao, H. Xiao, T. Sun, W. Guo, J. Chin. Ceram. Soc. 38 (2010) 1553-1557.

[36] P.E.D. Morgan, D.B. Marshall, Mater. Sci. Eng. A162 (1993) 15-25.

[37] S.V. Komarov, S.E. Romankov, S.H. Son, N. Hayashi, S.D. Kaloshkin, S. Ueno, E. Kasai, Surf. Coat. Technol. 202 (2008) 5180-5184.

[38] G.J. McCarthy, W.B. White, D.E. Pfoertsch, Mater. Res. Bull. 13 (1978) 1239-1245.

[39] A. Meldrum, L.A. Boatner, R.C. Ewing, Phys. Rev. B 56 (1997) 13805-13814.

[40] H.D. Park, E.R. Kreidler, J. Am. Ceram. Soc. 67 (1984) 23-26.

[41] J. Kropiwnicka, T. Znamierowska, Pol. J. Chem. 62 (1988) 587-594.

[42] W. Jungowska, T. Znamierowska, Mater. Chem. Phys. 48 (1997) 230-233.

[43] O.A. Serra, E. Giesbrecht, J. Inorg. Nucl. Chem. 30 (1968) 793-799.

[44] V.A. Ashuiko, I.A. Rat'kovskii, M.I. Kuz'menkov, N.M. Sergeeva, Izv. Vyssh. Uchebn. Zaved., Khim. Khim. Tekhnol. 18 (1975) 675.

[45] A.G. Buyers, E. Giesbrecht, L.F. Audrieth, J. Inorg. Nucl. Chem. 5 (1957) 133-140.

[46] I.V. Tananaev, V.P. Vasil'eva, Russ. J. Inorg. Chem. 8 (1963) 555-558.

[47] R. Kijkowska, J. Mater. Sci. 38 (2003) 229-233.

[48] H.G. Danielmeyer, J.P. Jeser, E. Schönherr, W. Stetter, J. Cryst. Growth 22 (1974) 298-302.

[49] R.D. Plättner, W.W. Krühler, W.K. Zwicker, T. Kovats, S.R. Chinn, J. Cryst. Growth 49 (1980) 274-290.

[50] M. Yoshimura, K. Fujii, S. Somiya, Mater. Res. Bull. 16 (1981) 327-333.

[51] K. Byrappa, M.K. Devaraju, J.R. Paramesh, B. Basavalingu, K. Soga, J. Mater. Sci. 43 (2008) 2229-2233.

[52] Y. Fujishiro, H. Ito, T. Sato, A. Okuwaki, J. Alloys Compd. 252 (1997) 103-109.

[53] N.N. Chudinova, L.P. Shklover, A.É. Balanevskaya, L.M. Shkol'nikova, A.E. Obodovskaya, G.M. Balagina, Inorg. Mater. 14 (1978) 569-574.

[54] E.G. Tselebrovskaya, B.F. Dzhurinskii, G.V. Lysanova, M.G. Komava, Russ. J. Inorg. Chem. 36 (1991) 1387-1389.

[55] H.Y.-P. Hong, Acta Cryst. B30 (1974) 469-474.

[56] R.S. Feigelson, J. Am. Ceram. Soc. 47 (1964) 257-258.

[57] H. Kasano, Y. Furuhata, J. Electrochem. Soc. 127 (1980) 2464-2468.

[58] H. Schäfer, V.P. Orlovskii, M. Wiemeyer, Z. Anorg. Allg. Chem. 390 (1972) 13-24.

[59] H.G. Danielmeyer, H.P. Weber, IEEE J. Quantum Electron. QE-8 (1972) 805-808.

[60] D.C. Miller, L.K. Shick, C.D. Brandle, J. Cryst. Growth 23 (1974) 313-317.

[61] M. Marais, N.D. Chinh, H. Savary, J.P. Budin, J. Cryst. Growth 35 (1976) 329-333.

[62] H. Kasano, Y. Furuhata, J. Electrochem. Soc. 126 (1979) 1567-1572.

[63] K. Watanabe, S. Tsunoda, J. Cryst. Growth 79 (1986) 953-962.

[64] N.N. Chudinova, L.P. Shklover, G.M. Balagina, Inorg. Mater. 11 (1975) 590-593.

[65] M. Tsuhako, S. Ikeuchi, T. Matsuo, I. Motooka, M. Kobayashi, Bull. Chem. Soc. Jpn. 52 (1979) 1034-1040.

[66] G.M. Balagina, N.N. Chudinova, E.V. Murashova, Russ. J. Inorg. Chem. 49 (2004) 614-616.

[67] N.N. Chudinova, Inorg. Mater. 15 (1979) 730-738.

[68] K. Byrappa, Prog. Cryst. Growth Charact. 13 (1986) 163-196.

Chapter 2
Synthesis of Lanthanum Phosphates in Phosphoric Acid Solutions

2.1 Introduction

As described in Chapter 1, a new synthesis method of $LaPO_4$ and LaP_3O_9 which facilitates the control of grain size is required. Also, the synthesis and densification of the compounds should be completely done at low temperatures to avoid lowering of Sr doping level and thermal decomposition. The most suited for this purpose might be the synthesis *via* precipitation in condensed phosphoric acid solutions. This method has been widely used for preparing single crystals of rare earth ultraphosphates, REP_5O_{14}, as laser materials. The common procedure of this method can be described as follows: A mixture of rare earth oxide and phosphoric acid is heated to several hundred degrees Celsius (*e.g.* 300 °C) to dissolve the oxide into phosphoric acid completely; Then the solution is heated up to higher temperatures (*e.g.* 500 °C) to precipitate REP_5O_{14}. Through related works, it was found that $LaPO_4$ and LaP_3O_9 precipitate at temperatures below ~300 °C [1-3]. According to Chudinova *et al.*, the temperature ranges of precipitation are below 160 °C for $LaPO_4$ and 180–240 °C for LaP_3O_9 [1]. They also reported that increase in gas humidity from 0.013 to 0.2 atm extends the temperature range of precipitation of LaP_3O_9 up to ~300 °C [3].

However, the literature focusing on the synthesis of $LaPO_4$ and LaP_3O_9 in condensed phosphoric acid solutions is still scarce. There has been no information on the morphologies of these precipitates. It is also of interest to know the crystallographic modification of the $LaPO_4$ precipitate. There are two polymorphs known for $LaPO_4$, namely, monazite and rhabdophane. The monazite-type

$LaPO_4$ has been investigated as a proton conductor [4]. It has been typically synthesized through high-temperature heat treatments, but the nanocrystals of monazite-type $LaPO_4$ have also been synthesized at low temperatures (such as 120 °C and 150 °C) by hydrothermal method [5,6]. Meanwhile, when synthesis was carried out in aqueous solutions at temperatures below 100 °C, the rhabdophane phase ($LaPO_4 \cdot xH_2O$) was obtained [7]. It was also reported that the rhabdophane phase was obtained by heating a mixture of La_2O_3 and H_3PO_4 (P/La = 1) at 150 °C [8].

In this chapter, the precipitation conditions of $LaPO_4$, LaP_3O_9 and LaP_5O_{14} were investigated under both ambient and humidified atmospheres. The crystal modification of the obtained $LaPO_4$ was identified by powder X-ray diffraction analysis. The morphologies of precipitates were also analyzed in relation to the precipitation condition.

2.2 Principles of the Synthesis Method

When phosphoric acid is heated, it gradually loses H_2O and condensation of phosphate anions takes place. The condensation can be expressed by the general formula:

$$n\ H_3PO_4\ (l) \rightarrow H(HPO_3)_nOH\ (l) + (n-1)\ H_2O\ (g). \quad (2.1)$$

The rate of H_2O loss increases with increasing temperature or decreasing the water vapor pressure. Therefore, when the water vapor pressure is constant as in ambient atmosphere, the rate of H_2O loss or the P_2O_5 concentration in the liquid phase is determined only by temperature. This interdependence between the P_2O_5 concentration and temperature is shown in the binary phase diagram of the H_2O–P_2O_5 system (Figure 2.1).

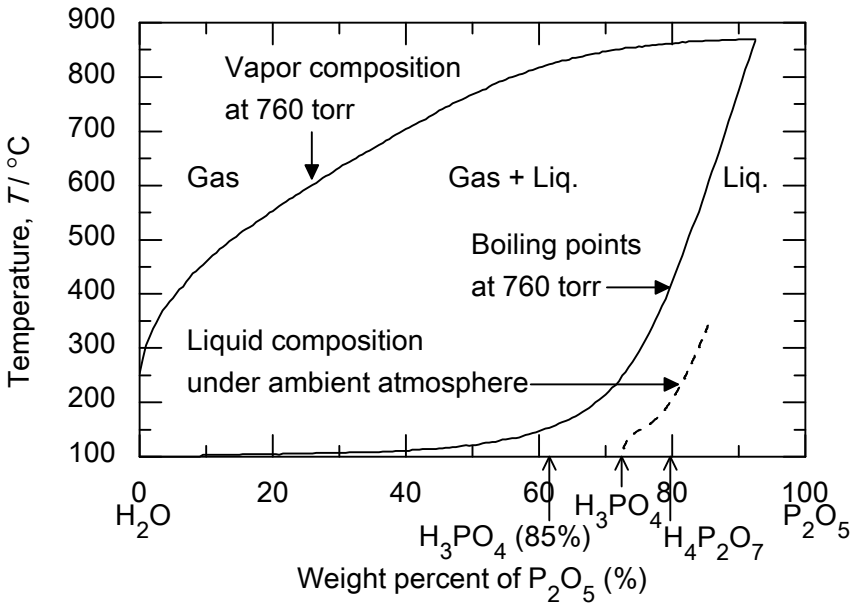

Figure 2.1 Phase diagram of the H_2O–P_2O_5 system adopted from Refs. [9,10].

Lanthanum phosphates can be precipitated in phosphoric acid containing lanthanum oxide. Chudinova *et al.* investigated the phase equilibria in the La_2O_3–P_2O_5–H_2O system, especially those between the phosphoric acid solution and lanthanum phosphates in ambient atmosphere [1]. Just like the H_2O–P_2O_5 system, the P_2O_5 concentration in the solution in an open system is determined only by temperature. Therefore, the P_2O_5 concentration cannot be varied arbitrary at any constant temperature. Chudinova *et al*. determined the solubility of La_2O_3 in such phosphoric acid solution at each temperature. They also determined the solid phase in equilibrium with the solution. The results were presented in a Gibbs triangle in a similar manner to a conventional isothermal section of a ternary phase diagram (Figure 2.2). This diagram is actually not an isothermal section but a diagram at a constant water vapor pressure.

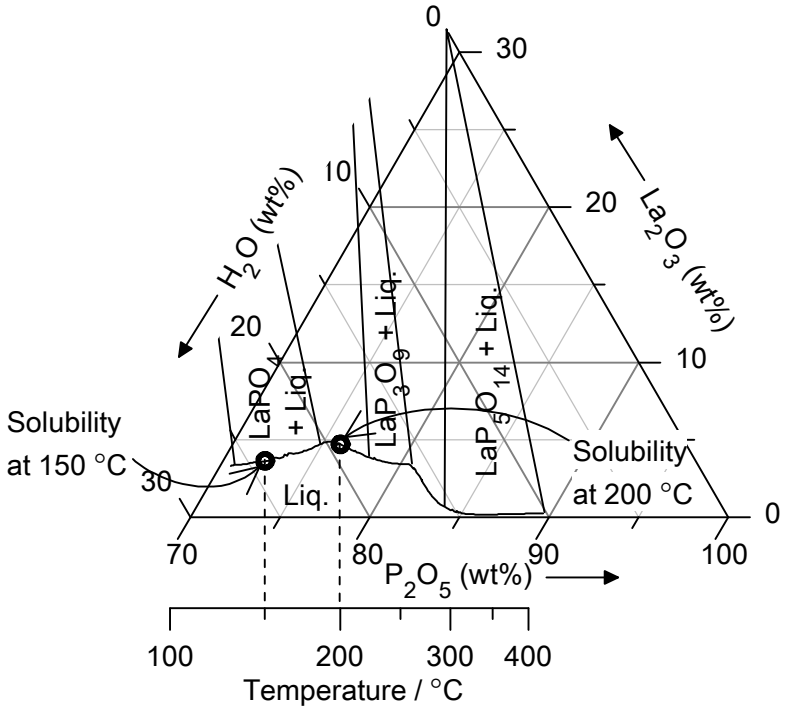

Figure 2.2 Phase diagram of the La_2O_3–P_2O_5–H_2O system at 100–500 °C by Chudinova *et al.* [1] The solubility of La_2O_3 in the liquid phase at each temperature can be obtained using the temperature axis below, as shown in the figure.

The relationship between conventional isothermal diagrams and the Chudinova's phase diagram (Figure 2.2) can be explained as follows. Figure 2.3 is a schematic illustration of the isothermal sections of the La_2O_3–P_2O_5–H_2O phase diagram at 150 °C and 200 °C. The broad curves in the figure represent the compositions of phosphoric acid solutions in equilibrium with water vapor in the ambient atmosphere. As the solubility of La_2O_3 in the phosphoric acid solution is on the order of only a few weight percent, the P_2O_5 concentration in the solution is assumed almost equal to that given for the H_2O–P_2O_5 binary system (dashed line in Figure 2.1). "Point A" in the figure represents the composition of such phosphoric acid solution in equilibrium with a solid phase (one of lanthanum phosphates). This point represents the solubility of La_2O_3 in the solution at the given temperature. The position of Point A changes with temperature and its trajectory can be expressed as a curve in the temperature–composition space (Figure 2.4). By projecting the curve on the Gibbs triangle, a

diagram is obtained which provides the solubility of La_2O_3 in the solution in a wide temperature range but at a constant water vapor pressure (Figure 2.2). This type of diagram is suitable for the crystal growth of rare earth phosphates in ambient atmosphere and has been reported for several systems [1,11,12]. It should be noted that the isothermal sections of the La_2O_3–P_2O_5–H_2O phase diagram presented in Figure 2.3 is drawn on the assumption that the phase equilibria between the liquid phase and solid phases do not change drastically with temperature. It has proved to be true for a similar system, Nd_2O_3–P_2O_5–H_2O system [12-14].

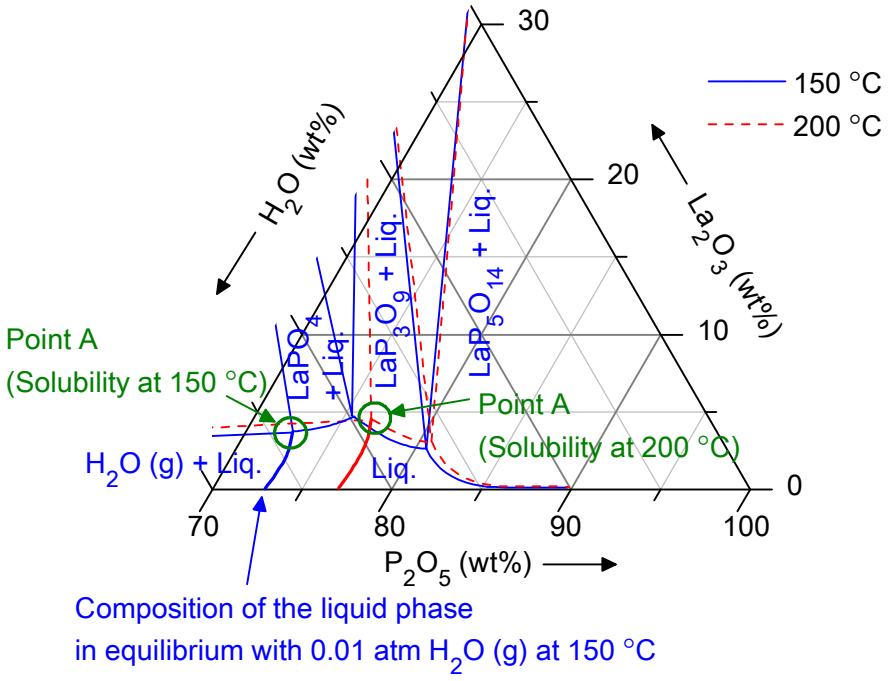

Figure 2.3 Schematic illustration of isothermal sections of the phase diagram of the La_2O_3–P_2O_5–H_2O system at 150 and 200 °C. Point A represents the three phases equilibrium between the solution, solid phase, and gas phase (p_{H2O} ~ 0.01 atm), or the solubility of La_2O_3 in the solution.

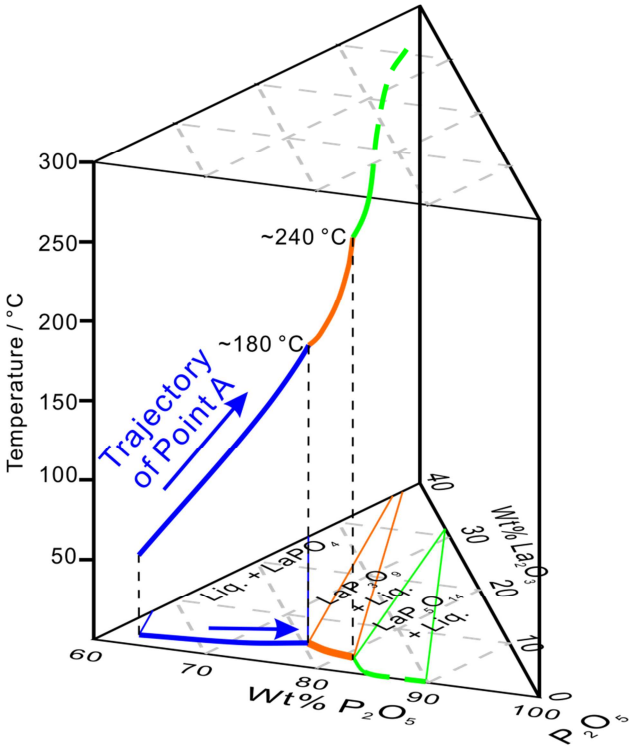

Figure 2.4 Trajectory of Point A in the temperature–composition space. The trajectory is also projected on the Gibbs triangle at the bottom.

Based on Figure 2.2, the solubility of La_2O_3 in the phosphoric acid solution is found to be highest at ~190 °C. At lower and higher temperatures, the solubility of La_2O_3 decreases and several lanthanum phosphates can be precipitated: $LaPO_4$ at lower temperatures, and LaP_3O_9 and LaP_5O_{14} at higher temperatures. Therefore, the dissolution temperature of La_2O_3 in phosphoric acid before the precipitation process was set at 190 °C in this work.

As mentioned at the beginning of this section, change in water vapor pressure also affects the composition of the phosphoric acid solution. As increasing water vapor pressure decreases the P_2O_5 concentration in the solution, it increases the temperature ranges of the precipitation of each phosphate from those in ambient atmosphere. This effect is so far confirmed by Balagina *et al*. for LaP_3O_9 [3]. According to Byrappa, the process of formation of ortho- and polyphosphates ($REPO_4$ and REP_3O_9) is very slow at temperatures lower than 260 °C and it is rather difficult to carry out the synthesis [15]. However, if sufficient humidification is applied, synthesis of these phosphates would be easier. In this work, the effect of humidification on the precipitation behaviors of lanthanum

phosphates was also investigated.

2.3 Experimental

2.3.1 Synthesis

$LaPO_4$, LaP_3O_9, and LaP_5O_{14} were synthesized by precipitation in homogeneous phosphoric acid solutions containing La_2O_3. La_2O_3 (99.99%, Nacalai Tesque) and H_3PO_4 (85%, Nacalai Tesque) were mixed at a P/La molar ratio of 15 in a perfluoroalkoxy (PFA) or glassy carbon (GC) crucible and held at 190 °C in a furnace for several days to obtain a transparent solution. Then temperature and water vapor pressure were changed and held for a predetermined period of time to precipitate the lanthanum phosphates. The temperature was set between 120 °C and 350 °C, and the water vapor pressure was set to approximately 0.01 atm (ambient atmosphere) or 1 atm (humidified atmosphere). Synthesis parameters are summarized in Table 2.1.

Table 2.1 Dissolution and precipitation conditions for the synthesis of $LaPO_4$, LaP_3O_9, and LaP_5O_{14}.

Abbr.	Dissolution		Precipitation		
	Temp. / °C	p_{H2O} / atm	Temp. / °C	p_{H2O} / atm	Time / h
A300	190	~0.01	300	~0.01	20
A230			230	~0.01	72
A140			140	~0.01	72
H350			350	~1	16
H250			250	~1	75
H140			140	~1	72

For humidification, the apparatus shown in Figure 2.5 was used. The whole apparatus was placed in a furnace kept at a constant temperature. A crucible was put on a stainless steel floor plate and covered with a stainless steel box with a capacity of 2.64 L. A 4-m-long spiral tube was attached to a side wall of the box. Liquid water was fed to the box through the spiral tube so that it evaporated before reaching the box. The liquid water feed rate was 0.1 mL/min, which was equivalent to 0.19 L-H_2O(g)/min at 140 °C and 0.28 L-H_2O(g)/min at 350 °C. The apparatus was not sealed tightly,

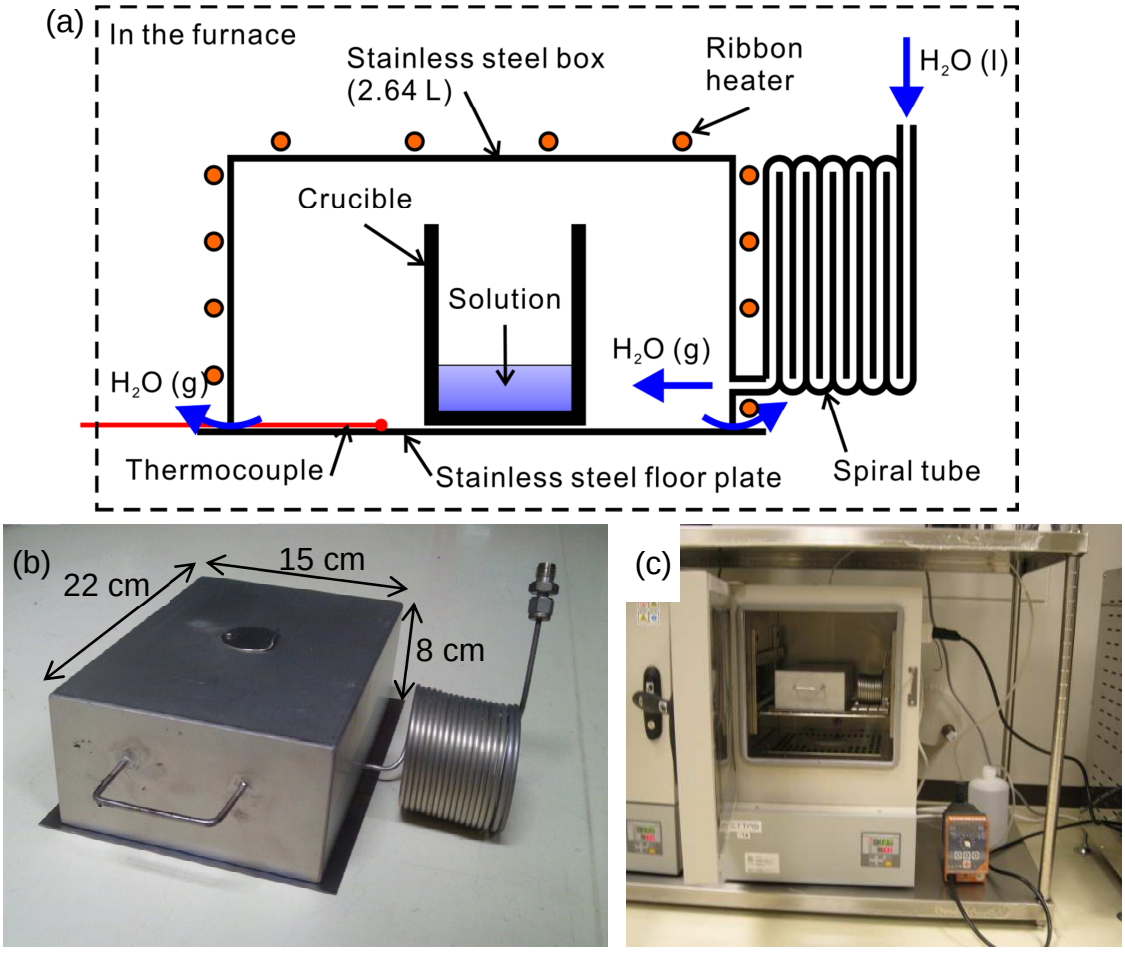

Figure 2.5 (a) Schematic illustration of the apparatus used for humidification during the precipitation of lanthanum phosphates. The thermocouple and ribbon heater were used only for H350 condition. (b) Photo of the stainless steel box and floor plate. (c) Photo of the stainless steel box and floor plate (without the ribbon heater) placed in the furnace and connected with a metering pump on the right.

so that the inner gas was able to flow out through the narrow gap between the box and the floor plate when the inner pressure exceeded 1 atm. Therefore, the water vapour pressure inside the box was expected to be 1 atm. For H350 condition, a ribbon heater wrapped around the stainless steel box was used for heating the solution up to 350 °C while the temperature in the furnace was kept at 270 °C. The temperature inside the stainless steel box was measured by a thermocouple attached to the upper surface of the floor plate.

After the predetermined precipitation period, the crucible was cooled down to room temperature. In general, there were precipitates on the bottom of the crucible and the transparent solution above them. The precipitates were washed well with hot water (~90 °C).

2.3.2 Characterization

Phase identification was carried out via X-ray powder diffraction (XRD) analysis on PANalytical X'Pert-Pro MPD using Cu Kα radiation at room temperature. The morphology of precipitates was investigated using KEYENCE VE-7800 scanning electron microscopy (SEM).

2.4 Results and Discussion

The precipitation temperatures of lanthanum phosphates were investigated under both atmospheric and humidified conditions with the synthesis parameters shown in Table 2.1. In all of the conditions (A300, A230, A140, H350, H250, and H140), colorless precipitates were obtained at the bottom of the crucibles. Figure 2.6 shows the X-ray diffraction patterns of the precipitates. Under the atmospheric conditions, LaP_5O_{14}, LaP_3O_9, and $LaPO_4$ were obtained at 300 °C (A300), 230 °C (A230), and 140 °C (A140), respectively. This is consistent with the results reported by Chudinova *et al*. [1] The obtained $LaPO_4$ had the monazite-type structure, which has been reported to exhibit proton conduction. Under the humidified conditions, LaP_3O_9 was obtained at 350 °C (H350) while monazite-type $LaPO_4$ was obtained at 250 °C and 140 °C. With these results, the precipitation region

of $LaPO_4$ was drawn on the temperature–p_{H2O} plane (Figure 2.7). As indicated in the figure, increasing water vapor pressure from 0.01 to 1 atm extends the precipitation regions of $LaPO_4$ and LaP_3O_9 toward higher temperatures by nearly 100 °C. At p_{H2O} = 1 atm, $LaPO_4$ can be obtained even at 250 °C, while LaP_3O_9 will be obtained at lower water vapor pressures such as 0.2 atm. Similarly, LaP_3O_9 can be obtained at 350 °C and p_{H2O} = 1 atm while LaP_5O_{14} will be obtained in lower humidification levels.

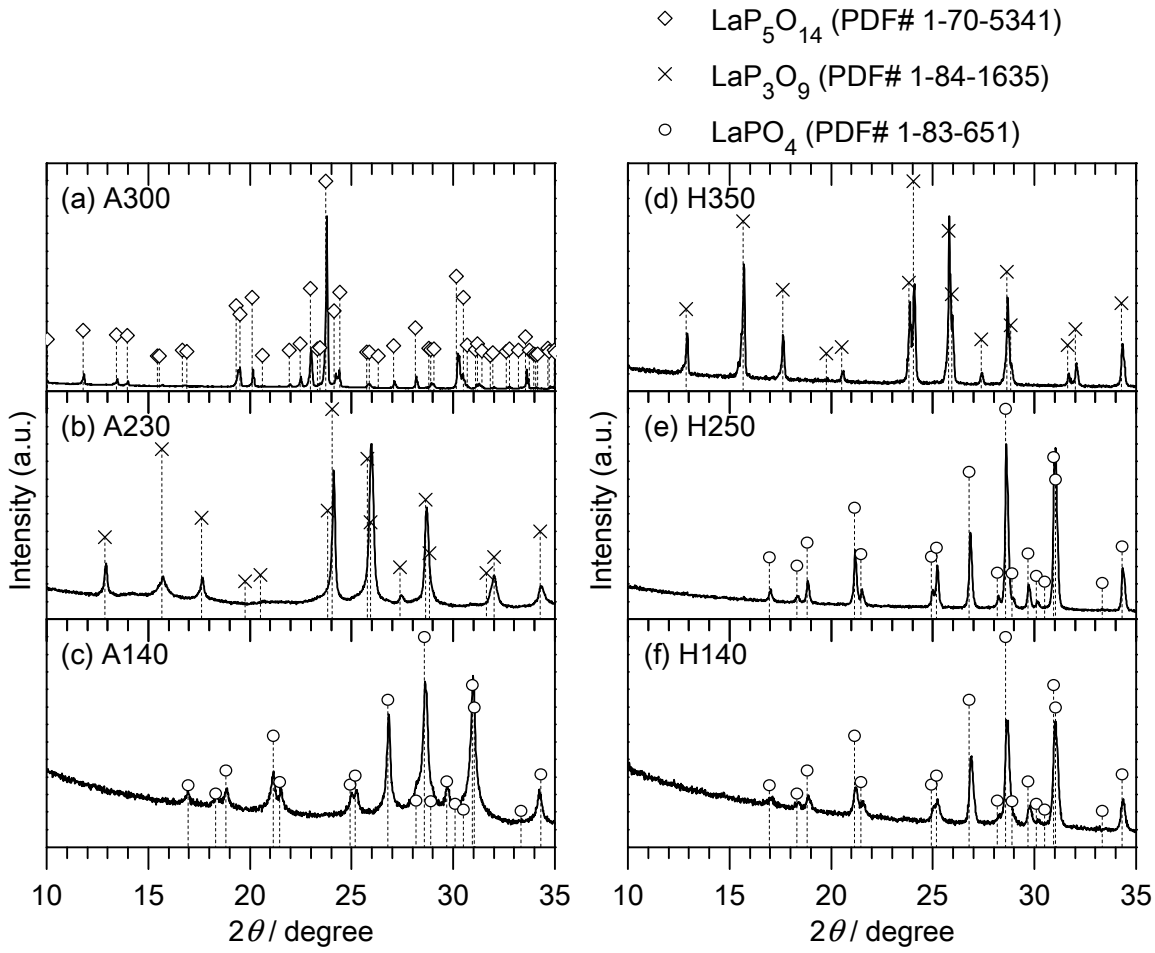

Figure 2.6 X-Ray powder diffraction patterns of lanthanum phosphate precipitates obtained under the conditions (a) A300, (b) A230, (c) A140, (d) H350, (e) H250, and (f) H140.

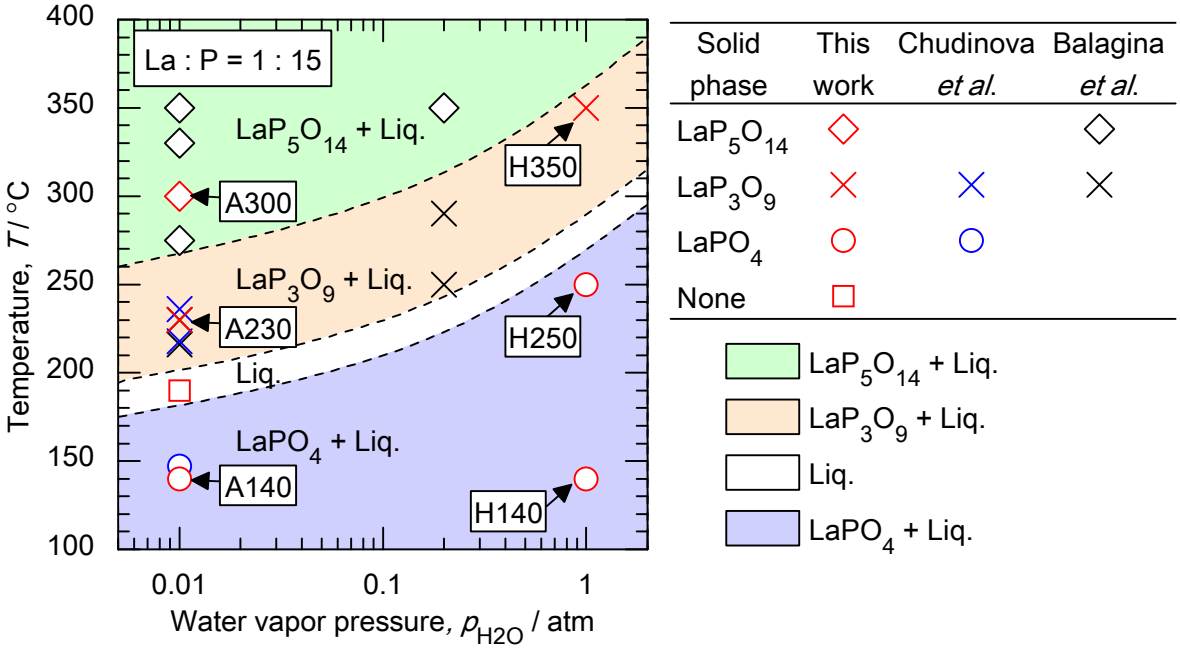

Figure 2.7 Phase stability diagram of the La_2O_3–P_2O_5–H_2O system with a constant La/P ratio (La : P = 1 : 15). In addition to the results obtained in this research, previous results reported by Chudinova *et al.* [1] and Balagina *et al.* [3] are also shown.

Figure 2.8 shows SEM images of $LaPO_4$ and LaP_3O_9 precipitates. Under the conditions A140 and H140, $LaPO_4$ precipitates were rice-shaped particles with a size range of 500 nm^{-1} μm. In contrast, under H250 condition, the $LaPO_4$ precipitates were aggregates of well-shaped crystals up to 200 μm. Thus, the precipitation temperature had a marked effect on the crystal growth of $LaPO_4$. As for LaP_3O_9, crystals of ~100 μm were obtained at 230 °C (A230) while those of ~300 μm were obtained at 350 °C (A350). Therefore, the crystal growth of LaP_3O_9 was also accelerated by increasing the precipitation temperature, though the effect was not as drastic as that on $LaPO_4$.

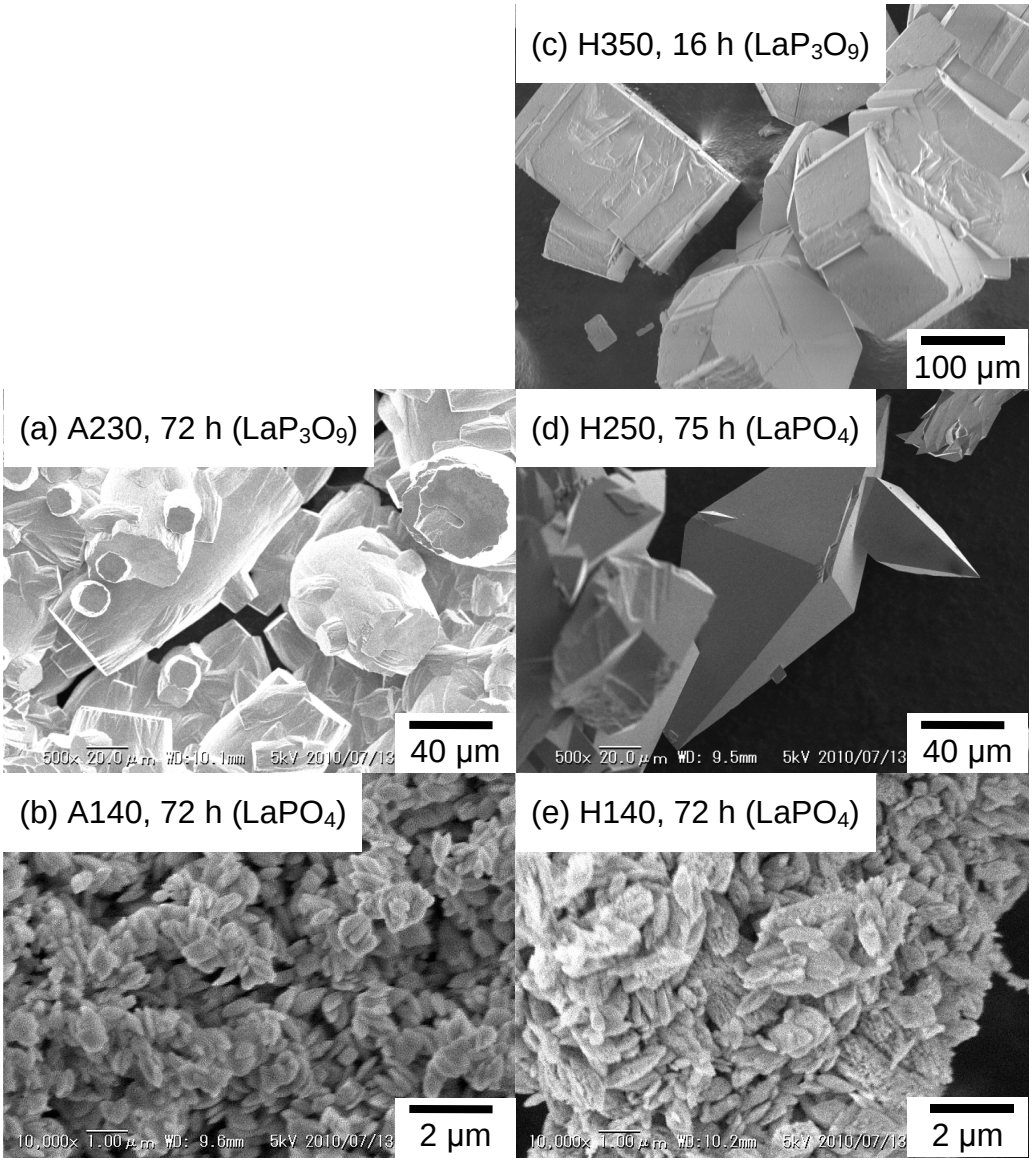

Figure 2.8 SEM images of $LaPO_4$ and LaP_3O_9 precipitates obtained under the conditions (a) A230, (b) A140, (c) H350, (d) H250, and (e) H140.

2.5 Conclusions

In this chapter, the precipitation conditions of $LaPO_4$, LaP_3O_9, and LaP_5O_{14} in condensed phosphoric acid solutions were established under both atmospheric and humidified conditions. The obtained $LaPO_4$ had the monazite-type structure, which has been reported to exhibit proton conduction. Increasing water vapor pressure from 0.01 atm to 1 atm extended the precipitation regions of $LaPO_4$ and LaP_3O_9 toward higher temperatures by nearly 100 °C. The crystal growth of

$LaPO_4$ was significantly accelerated under such conditions (e.g. T=250 °C and p_{H2O} = 1 atm). The crystal growth of LaP_3O_9 was also promoted moderately by the increase in precipitation temperature. These results will serve as fundamental information for further optimization of growth parameters (*e.g.* temperature profile, precipitation period, and initial composition) and hopefully the direct synthesis of dense lanthanum phosphate electrolytes in phosphoric acid solutions.

References

[1] N.N. Chudinova, L.P. Shklover, G.M. Balagina, Inorg. Mater. 11 (1975) 590-593.

[2] M. Tsuhako, S. Ikeuchi, T. Matsuo, I. Motooka, M. Kobayashi, Bull. Chem. Soc. Jpn. 52 (1979) 1034-1040.

[3] G.M. Balagina, N.N. Chudinova, E.V. Murashova, Russ. J. Inorg. Chem. 49 (2004) 614-616.

[4] S. Jørgensen, J.A. Horst, O. Dyrlie, Y. Larring, H. Ræder, T. Norby, Surf. Interface Anal. 34 (2002) 306-310.

[5] Y. Fujishiro, H. Ito, T. Sato, A. Okuwaki, J. Alloys Compd. 252 (1997) 103-109.

[6] K. Byrappa, M.K. Devaraju, J.R. Paramesh, B. Basavalingu, K. Soga, J. Mater. Sci. 43 (2008) 2229-2233.

[7] S. Lucas, E. Champion, E. Bregiroux, D. Bernache-Assollant, F. Audubert, J. Solid State Chem. 177 (2004) 1302-1311.

[8] H. Onoda, H. Nariai, A. Moriwaki, H. Maki, I. Motooka, J. Mater. Chem. 12 (2002) 1754-1760.

[9] E.H. Brown, C.D. Whitt, Ind. Eng. Chem. 44 (1952) 615-618.

[10] E. Thilo, R. Sauer, J. Prakt. Chem. 4 (1957) 324-348.

[11] N.N. Chudinova, Inorg. Mater. 15 (1979) 730-738.

[12] R.D. Plättner, W.W. Krühler, W.K. Zwicker, T. Kovats, S.R. Chinn, J. Cryst. Growth 49 (1980)

274-290.

[13] M. Yoshimura, K. Fujii, S. Somiya, Mater. Res. Bull. 16 (1981) 327-333.

[14] M. Yoshimura, K. Fujii, S. Somiya, J. Cryst. Growth 71 (1985) 333-339.

[15] K. Byrappa, Prog. Cryst. Growth Charact. 13 (1986) 163-196.

Chapter 3
Phase Equilibria in the La_2O_3–P_2O_5 System

3.1 Introduction

Various phosphates in the La_2O_3–P_2O_5 system have been studied not only as proton conductors, but also as laser and luminescent materials [1-4], phosphorus diffusion sources for semiconductors [5-7], debond materials in oxide composites [8], coating materials [9], and radioactive waste forms [10,11]. As written in Chapter 1, two phase diagrams have so far been presented for the La_2O_3–P_2O_5 system in the literature [12,13]. However, there are considerable differences in the compounds present and they may bring some confusion. For example, $La_7P_3O_{18}$, one of the proton conductors referred to in the previous chapter, is only present in the phase diagram by Park and Kreidler [12]. Harley *et al.* [14] adopted the La-rich part from Ref. [13] and P-rich part from Ref. [12] for some reason to show the La_2O_3–P_2O_5 phase diagram in their paper.

As shown in Table 3.1, the phase diagrams contain four intermediate compounds in common: La_3PO_7, $LaPO_4$, LaP_3O_9, and LaP_5O_{14}. In addition, Park and Kreidler [12] reported two compounds $La_7P_3O_{18}$ and $La_2P_4O_{13}$, and Kropiwnicka and Znamierowska [13] reported La_5PO_{10}. Therefore, further inspection should be necessary on the existence and stability of these three compounds. Here, a brief description is given on these compounds.

Table 3.1 Compounds in the La_2O_3–P_2O_5 phase diagrams in the literature. They are listed in increasing order of P_2O_5 content.

Compounds	Ref. [12]	Ref. [13]
La_5PO_{10}		X
La_3PO_7	X	X
$La_7P_3O_{18}$	X	
$LaPO_4$	X	X
$La_2P_4O_{13}$	X	
LaP_3O_9	X	X
LaP_5O_{14}	X	X

3.1.1 La_5PO_{10}

La_5PO_{10} has a composition between La_2O_3 and La_3PO_7. La_5PO_{10} was obtained by Kropiwnicka and Znamierowska [13,15] *via* solid state reaction between La_2O_3 and $NH_4H_2PO_4$ at temperatures above 540 °C. They determined its congruent melting temperature to be 1870 ± 10 °C. Meanwhile, Tselebrovskaya *et al*. [16] presented a phase diagram of the La_2O_3–$LaPO_4$–La_2GeO_5 system at 1300 °C, in which La_5PO_{10} was absent. El Ouenzerfi *et al*. [17] also observed that La_2O_3 and La_3PO_7 were in equilibrium at 1200–1400 °C, instead of forming La_5PO_{10}.

3.1.2 $La_7P_3O_{18}$

$La_7P_3O_{18}$ has a composition between La_3PO_7 and $LaPO_4$. $La_7P_3O_{18}$ has been synthesized by several researchers *via* solid state reactions and solidification of melts [12,18-22]. Serra *et al.* [20] observed an α-β phase transition at 1650 °C. According to Park and Kreidler [12], there is no evidence of a lower limit of stability. However, $La_7P_3O_{18}$ is obtainable only at temperatures above 1400 °C and it has not been synthesized at temperatures below 1200 °C [18,19,21,22]. The coexistence of La_3PO_7 and $LaPO_4$ at 1100–1200 °C was also observed by other authors [23,24]. Tselebrovskaya *et al.* attributed this to kinetic reasons [16,22].

3.1.3 $La_2P_4O_{13}$

$La_2P_4O_{13}$ has a composition between $LaPO_4$ and LaP_3O_9. Park and Kreidler obtained $La_2P_4O_{13}$ by crystallization from glass [12]. They found that it is stable at temperatures up to 755 °C. However, $La_2P_4O_{13}$ has not been obtained by other methods even at those temperatures [25-27]. The same phenomenon was found for the neodymium analogue, $Nd_2P_4O_{13}$, by Wong and Kreidler [27]: It was formed by crystallization of a glass, but not formed by direct solid-state reaction. They speculated that $Nd_2P_4O_{13}$ exists in a metastable state.

3.2 Experimental

3.2.1 Sample Preparation

La_2O_3 (Nacalai Tesque, mass fraction purity 0.9999) and H_3PO_4 (Nacalai Tesque, mass fraction purity 0.85) were used to prepare samples. La_2O_3 was heated overnight at 800 °C prior to use to remove absorbed H_2O and CO_2 [28]. $LaPO_4$ and LaP_3O_9 were synthesized by precipitation in phosphoric acid solutions, using the procedure given in Chapter 2. The $LaPO_4$ precipitates were dried at 800 °C for 100 h. For preparing samples with compositions between La_2O_3 and $LaPO_4$ (“L9P1”, “L8P2”, “L725P275”, “L7P3”, and “L6P4”), the La_2O_3 and $LaPO_4$ powders were mixed in the molar ratios listed in Table 3.2. The mixtures were then ballmilled for 70–100 h in isopropyl alcohol, dried, and pressed into pellets at ~150 MPa. The sample with a composition slightly poorer in P_2O_5 than LaP_3O_9, “L25P75−δ”, was prepared from LaP_3O_9. The LaP_3O_9 precipitate was ground and pressed into a pellet at ~400 MPa. The pellet was heated at 1050 °C for 3 h, to be partially decomposed according to the following reaction [12]:

$$LaP_3O_9\ (s) \rightarrow LaPO_4\ (s) + 1/2\ P_4O_{10}\ (g). \qquad (3.1)$$

Table 3.2 Compositions of samples.

Abbr.	Starting materials	Molar ratio		Remarks
		La :	P	
L9P1	La_2O_3 and $LaPO_4$	0.9	0.1	Between La_2O_3 and "La_5PO_{10}"
L8P2	La_2O_3 and $LaPO_4$	0.8	0.2	Between "La_5PO_{10}" and La_3PO_7
L725P275	La_2O_3 and $LaPO_4$	0.725	0.275	Between La_3PO_7 and "$La_7P_3O_{18}$"
L7P3	La_2O_3 and $LaPO_4$	0.7	0.3	Composition of "$La_7P_3O_{18}$"
L6P4	La_2O_3 and $LaPO_4$	0.6	0.4	Between "$La_7P_3O_{18}$" and $LaPO_4$
L25P75−δ	LaP_3O_9	0.25	0.75−δ	Slightly poorer in P_2O_5 than LaP_3O_9

3.2.2 Phase Equilibrium Experiments and Sample Characterization

Phase equilibrium experiments were carried by high-temperature heat treatments and subsequent phase identification. The sample pellets were placed in alumina crucibles, and heated at a predetermined temperature for typically 100 h in ambient atmosphere. Then the samples were cooled down in the furnace. The specific conditions for each heat treatment are provided in the following section. Phase identification was carried out via X-ray powder diffraction (XRD) analysis on PANalytical X'Pert-Pro MPD using Cu Kα radiation at room temperature. The microstructure of samples was analyzed using KEYENCE VE-7800 scanning electron microscopy (SEM).

3.3 Results and Discussion

3.3.1 La_2O_3–$LaPO_4$ Subsystem at 1000 and 1300 ℃

First, the phase relationships in the La_2O_3–$LaPO_4$ subsystem were investigated at 1000 °C and 1300 °C using samples L9P1, L8P2, L725P275, and L6P4. The samples were heated at each temperature for 100 h. Figure 3.1 and Figure 3.2 show the X-ray diffraction patterns of the samples after each heat treatment. The detected phases in each sample are summarized in Table 3.3. At both temperatures and in all of the samples, reactions between $LaPO_4$ and La_2O_3 occurred and intermediate phases were formed. The observed intermediate phases were La_3PO_7 at 1000 °C, and

La_3PO_7 and $La_7P_3O_{18}$ at 1300 °C. La_5PO_{10} was not detected at either temperature.

As for La_3PO_7, Park and Kreidler observed an α-β phase transition at 935 ± 5 °C [12]. They reported the X-ray diffraction patterns of both low-temperature α-phase and high-temperature β-phase. There have also been a few slightly different X-ray diffraction data reported for La_3PO_7 [20,29]. They are very similar, and it is rather difficult to distinguish them, but the present X-ray diffraction results are best fitted by the β-phase pattern given by Park and Kreidler.

Table 3.3 Phases present in samples L9P1, L8P2, L725P275, and L6P4 before and after heat treatments at 1000 °C or 1300 °C for 100h, as analyzed by powder X-ray diffraction.

Sample	Phases		
	Before heat treatments	After heat treatments	
		1000 °C, 100 h	1300 °C, 100 h
L9P1	La_2O_3, $LaPO_4$	(Not investigated)	La_2O_3[a], La_3PO_7
L8P2		La_2O_3[a], La_3PO_7	La_2O_3, La_3PO_7
L725P275		La_3PO_7, $LaPO_4$	La_3PO_7, **$La_7P_3O_{18}$**
L6P4		La_3PO_7, $LaPO_4$	**$La_7P_3O_{18}$**, $LaPO_4$

[a] Although $La(OH)_3$ was detected, it should have formed by hydration of La_2O_3 at room temperature after the heat treatments. Therefore, $La(OH)_3$ is expressed as "La_2O_3" in the table.

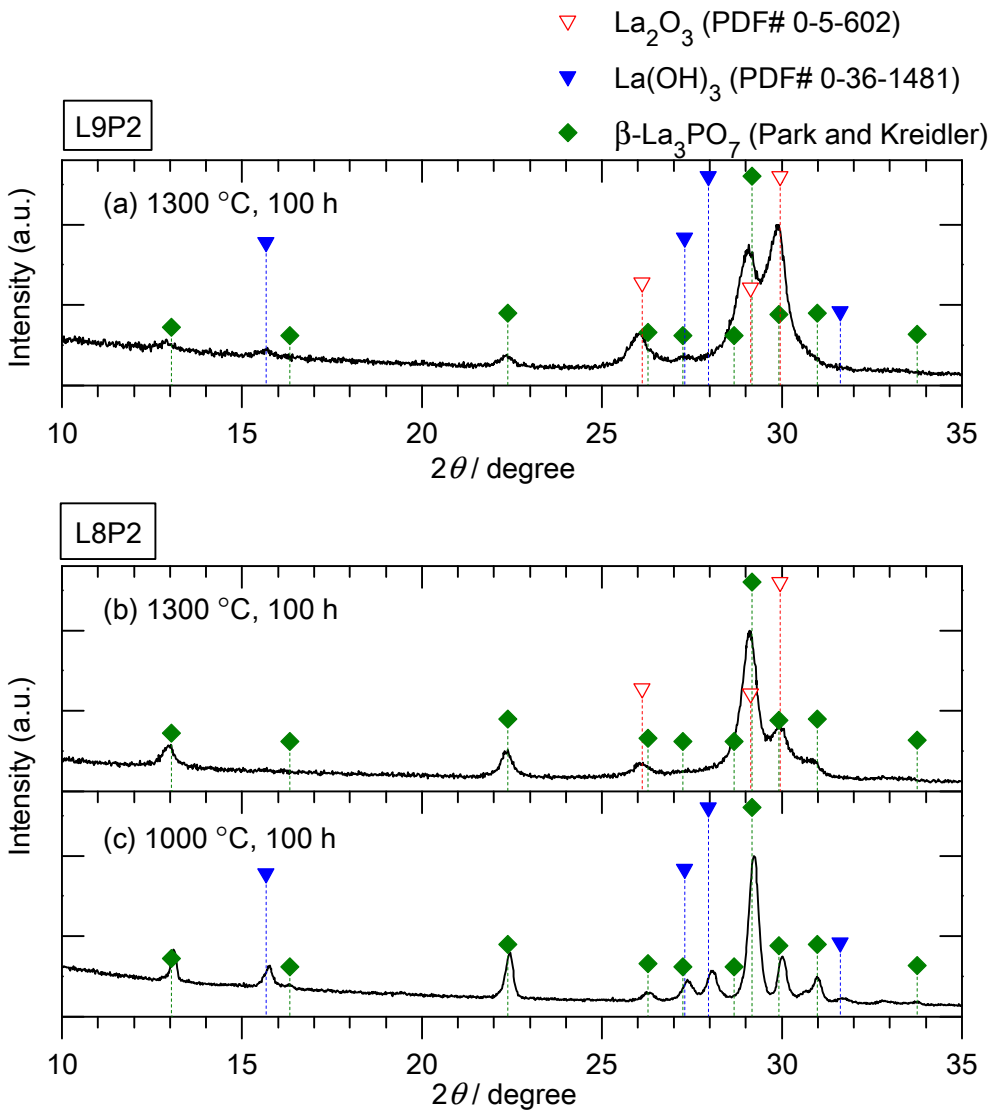

Figure 3.1 X-ray diffraction patterns of (a) L9P1 and (b)(c) L8P2 after heat treatments at (a)(b) 1300 °C or (c) 1000 °C for 100 h.

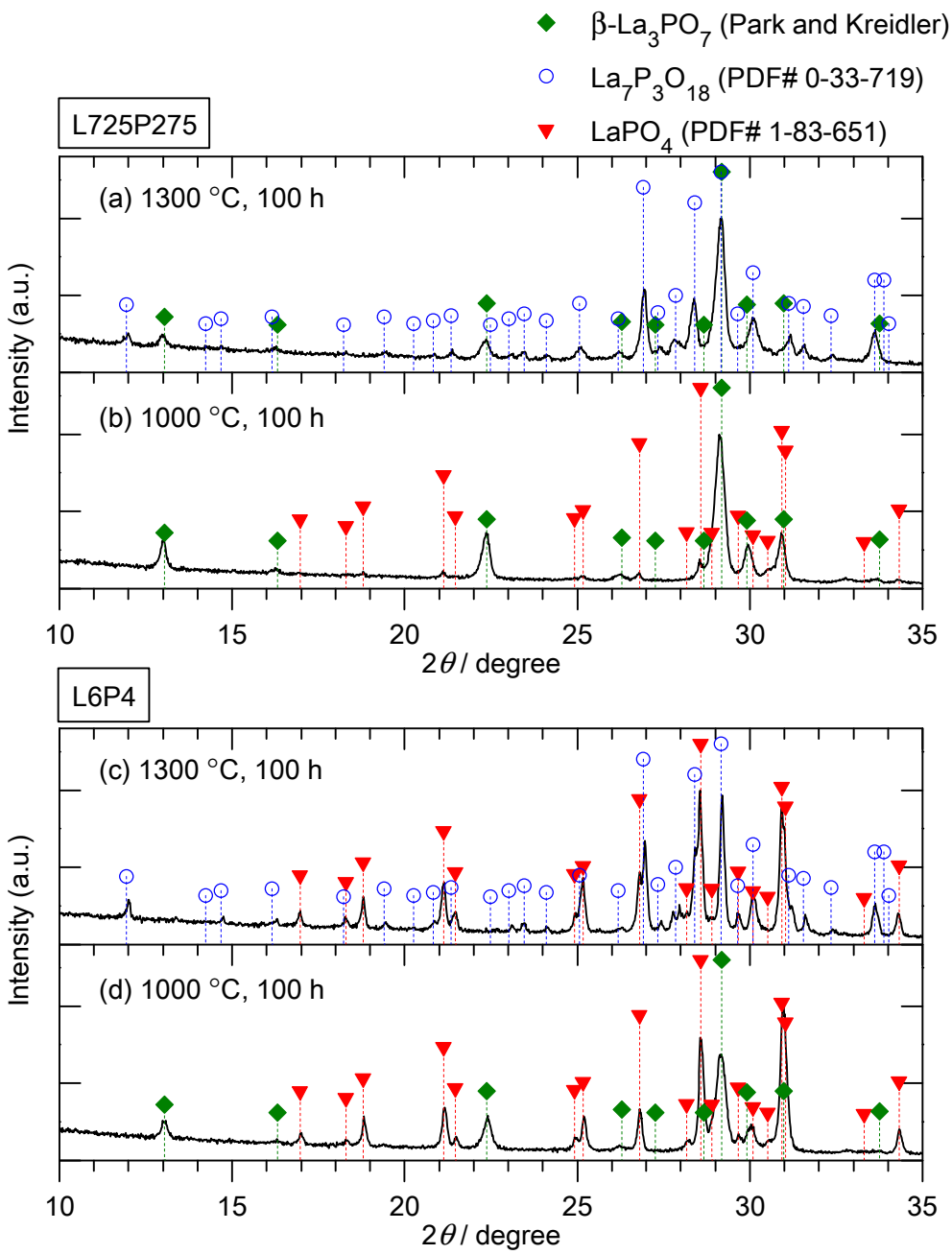

Figure 3.2 X-ray diffraction patterns of (a)(b) L725P275 and (c)(d) L6P4 after heat treatments at (a)(c) 1300 °C or (b)(d) 1000 °C for 100 h.

3.3.2 Phase Formation Process at the Composition La:P = 7:3

Since it was found in the previous subsection that $La_7P_3O_{18}$ was formed at 1300 °C while it was not formed at 1000 °C, further investigation was carried on the phase formation process at the composition La:P = 7:3. L7P3 samples (see Table 3.2) were heat treated in the temperature range

700–1300 °C with various stepwise temperature programs shown in Figure 3.3. Phase identification and SEM observation were performed after the heat treatments.

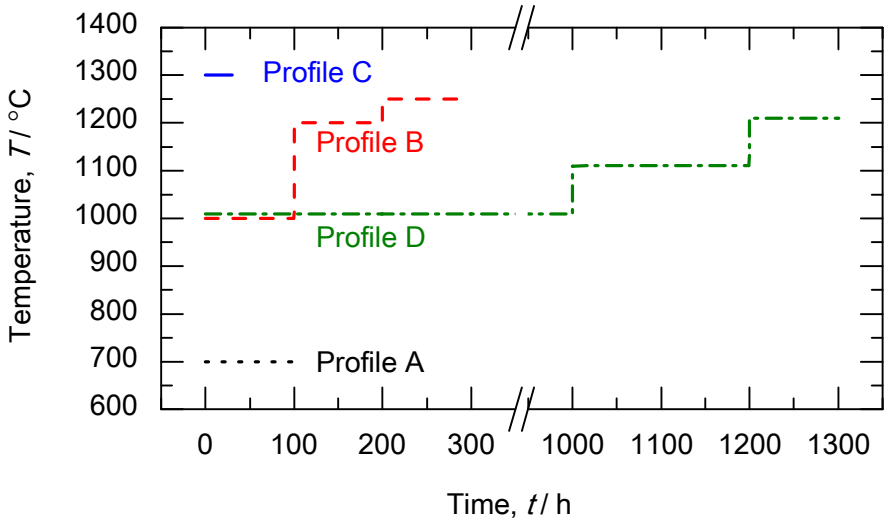

Figure 3.3 Temperature profiles for the heat treatments of L7P3. Occasional cooling to room temperature is not shown in the figure. Overlapping lines are slightly shifted for better visibility.

Figure 3.4 shows the X-ray diffraction patterns of L7P3 samples after various heat treatments (Temperature profile A–C in Figure 3.3). The sample held at 700 °C for 100 h (Temperature profile A) consisted of the same phases as the starting materials, La_2O_3 and $LaPO_4$, suggesting that almost no reaction occurred during the heat treatment. Weak peaks of $La_2O_2CO_3$ were also observed, but it could be because La_2O_3 reacted with CO_2 in the atmosphere during or after the heat treatment. On the other hand, in the sample held at 1000 °C for 100 h (Temperature profile B), La_3PO_7 and $LaPO_4$ were identified, but La_2O_3 was not observed. It indicates that the following reaction proceeded completely at 1000 °C:

$$La_2O_3 + LaPO_4 \rightarrow La_3PO_7 \text{ (700–1000 °C).} \quad (3.2)$$

An additional heat treatment of the sample at 1200 °C for 100 h did not have any effect on the phases present. With further heat treatment at 1250 °C for 100 h, essentially single phase $La_7P_3O_{18}$ was

formed by the following reaction:

$$La_3PO_7 + LaPO_4 \rightarrow La_7P_3O_{18} \text{ (~1250 °C).} \quad (3.3)$$

A small amount of $LaPO_4$ still remained in the sample, but it could be due to some compositional error in preparing the initial mixture. $La_7P_3O_{18}$ was also obtained by direct heating of another L7P3 sample to 1300 °C for 30 h (Temperature profile C).

To examine the kinetic effects on the formation process of $La_7P_3O_{18}$, long-term heat treatments of a L7P3 sample were performed at temperatures lower than 1250 °C with the temperature profile D (Figure 3.3). Figure 3.5 shows the X-ray diffraction patterns of the L7P3 sample during the heat treatments. Heating the sample at 1000 °C for 1000 h and at 1100 °C for 200 h did not result in the formation of $La_7P_3O_{18}$, consistent with previous results. However, after the subsequent heating at 1200 °C for 100 h, partial formation of $La_7P_3O_{18}$ from La_3PO_7 and $LaPO_4$ was observed. Comparing with the result obtained through the temperature profile B, it could be said that the long-term heat treatments at 1000–1100 °C slightly lowered the experimental formation temperature of $La_7P_3O_{18}$ to 1200 °C.

The kinetics of the formation process was also examined by SEM observation. Figure 3.6 shows typical SEM images of L7P3 samples before and after various heat treatments. The particle size of the as-ballmilled powder, shown in Figure 3.6 (a), was several hundred nm. It was not changed by the heat treatment at 700 °C, as shown in Figure 3.6 (b). It is consistent with the X-ray diffraction result which suggests no reaction occurred at 700 °C. On the other hand, larger and smoother grains were observed in the samples heated at 1000–1300 °C, at which La_3PO_7 and $La_7P_3O_{18}$ can be formed (Figure 3.6 (c) and (d)). It indicates that diffusion of atoms is possible at such temperatures. It should be noted that the grains in the sample heated at 1300 °C for only 30 h (single phase $La_7P_3O_{18}$) were even larger than those in the sample heated at 1000–1200 °C for a total of 1300 h ($La_7P_3O_{18}$ with residual La_3PO_7 and $LaPO_4$). Therefore, such temperature difference should have a significant effect on the rate of grain growth and diffusion of atoms. Considering the results of X-ray diffraction and

SEM observation together, there is a possibility that the formation process of $La_7P_3O_{18}$ is significantly governed by kinetics at temperatures below 1300 °C even if it is thermodynamically stable. The kinetic effects can further be characterized if smaller initial particles are used.

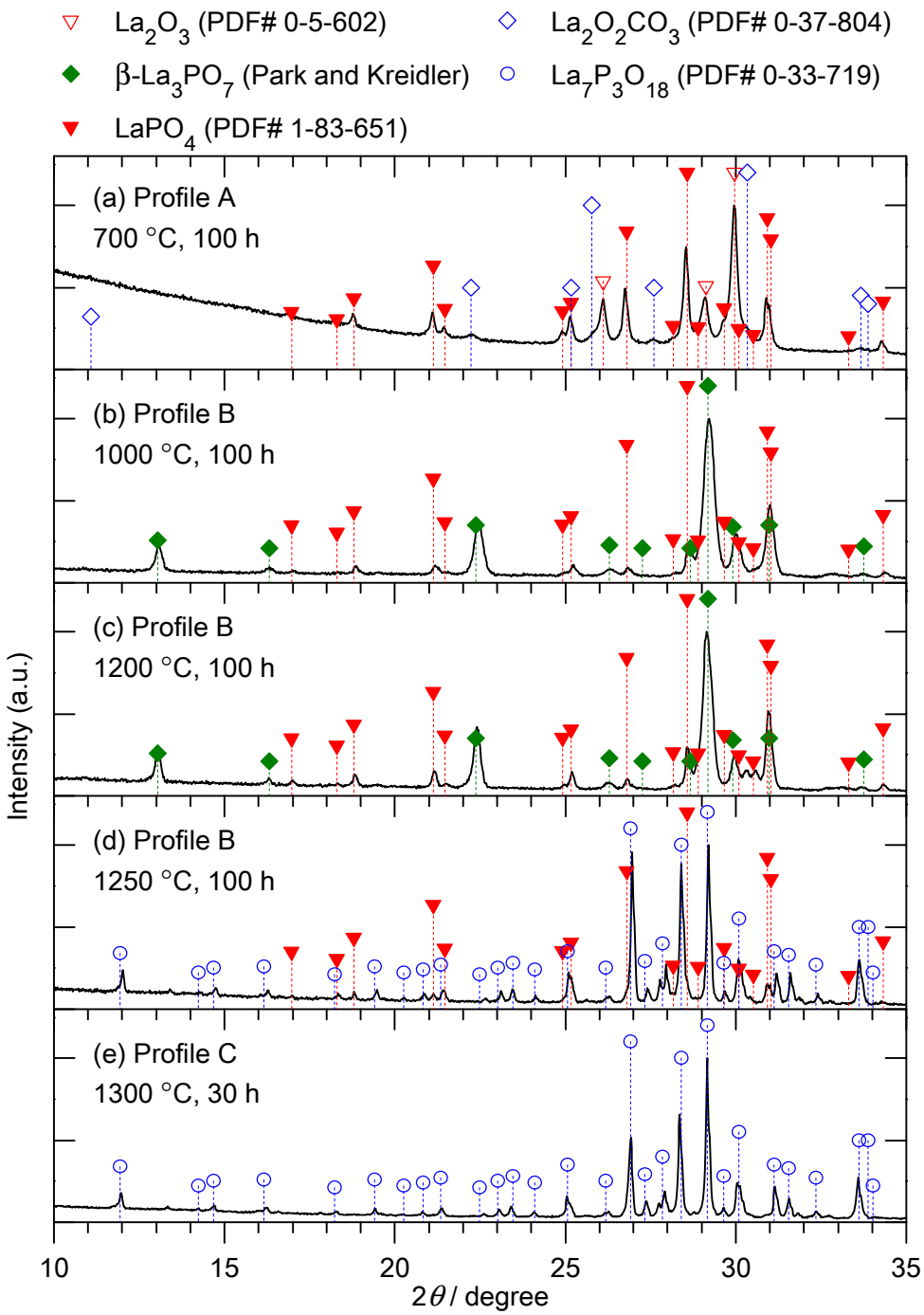

Figure 3.4 X-ray diffraction patterns of L7P3 after various heat treatments indicated as Profiles A-C in Figure 3.3. (a) After a heat treatment at 700 °C for 100 h (Profile A); (b) After the first heat treatment at 1000 °C for 100 h (Profile B); (c) After the second heat treatment at 1200 °C for 100 h (Profile B); (d) After the third heat treatment at 1250 °C for 100 h (Profile B); (e) After a heat treatment at 1300 °C for 30 h (Profile C).

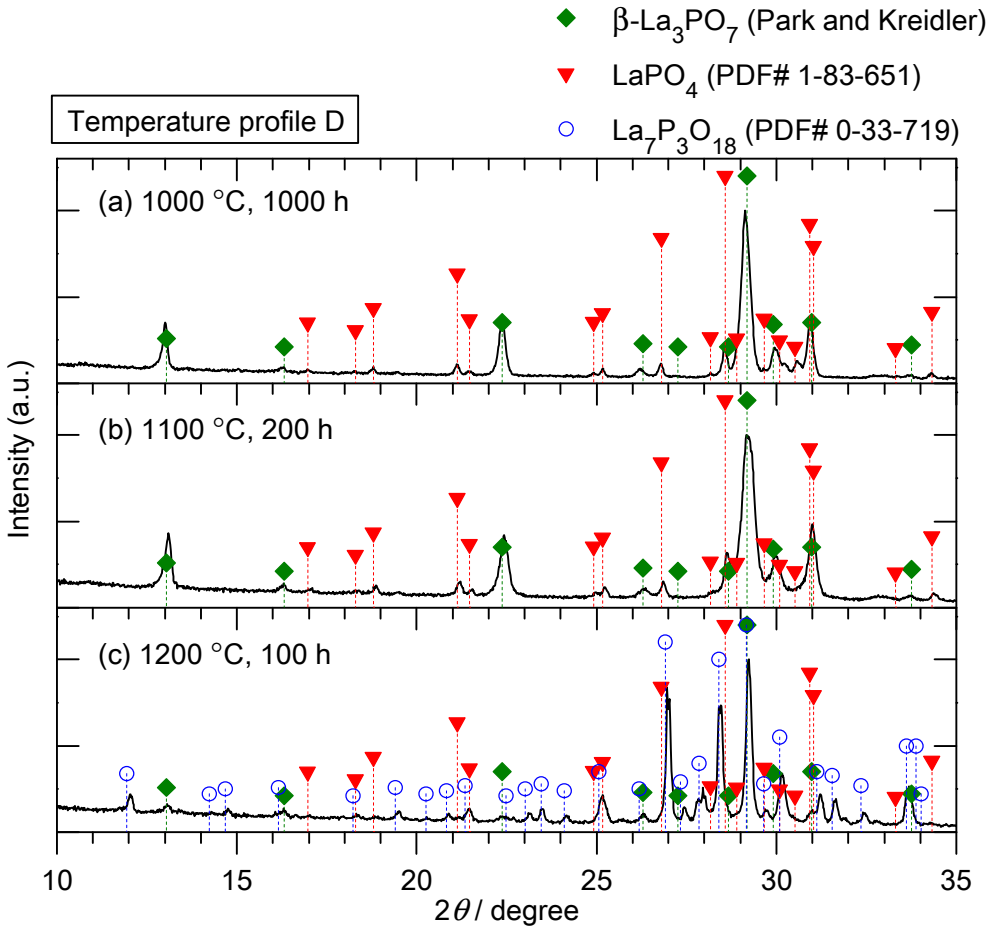

Figure 3.5 X-ray diffraction patterns of L7P3 after the heat treatments indicated as Profile D in Figure 3.3. (a) After heat treatments as 1000 °C for a total of 1000 h; (b) After additional heat treatments at 1100 °C for a total of 200h; (c) After an additional heat treatment at 1200 °C for 100 h.

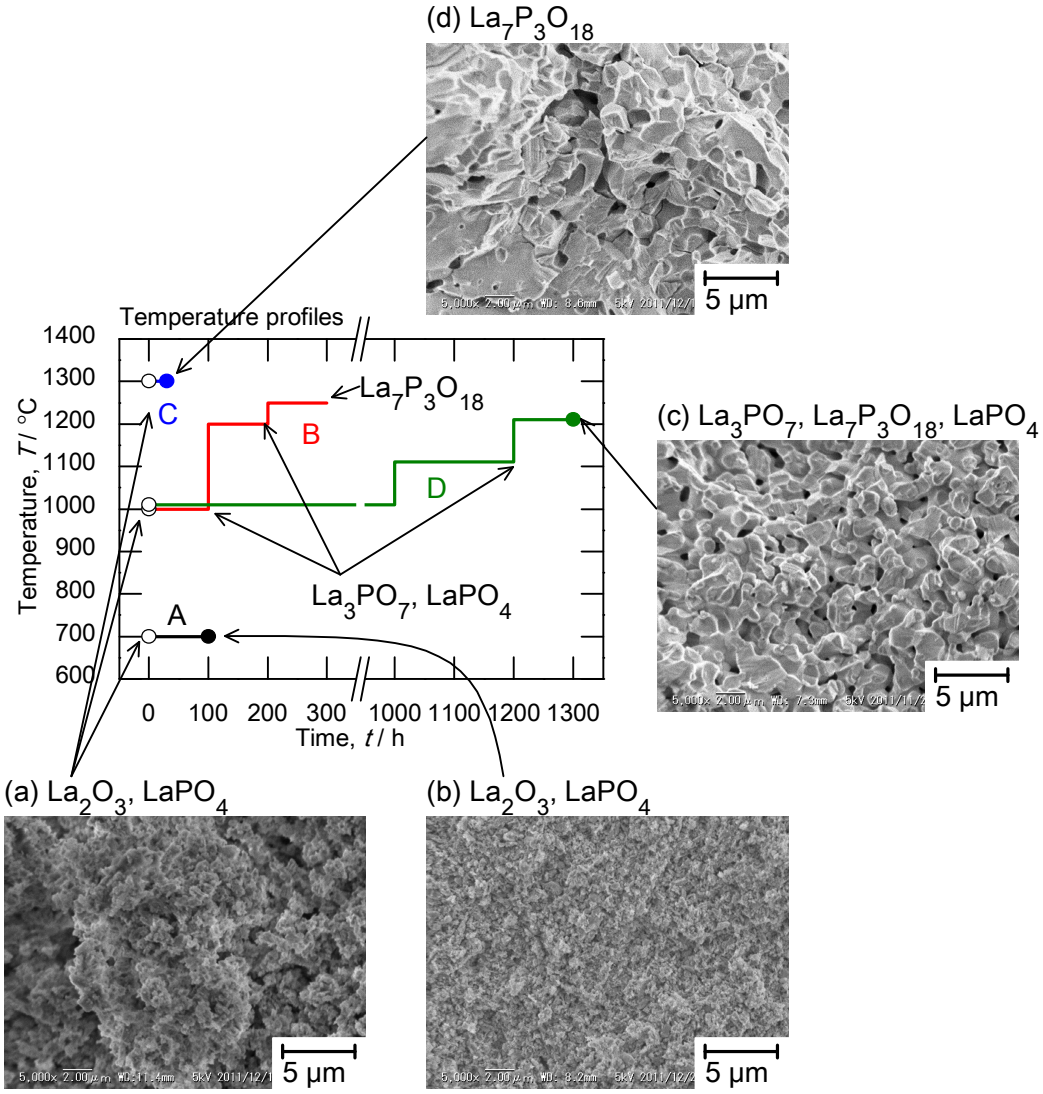

Figure 3.6 SEM images of L7P3. (a) As ballmilled powder; (b) After a heat treatment at 700 °C for 100 h (Temperature profile A in Figure 3.3); (c) After successive heat treatments at 1000 °C for 1000 h, at 1100 °C for 200 h, and at 1200 °C for 100 h (Temperature profile D in Figure 3.3); (d) After a heat treatment at 1300 °C for 30 h (Temperature profile C in Figure 3.3). The phases present in the samples are shown on each image.

3.3.3 Low Temperature Stability of $La_7P_3O_{18}$

Besides the kinetic reasons discussed above, another possible reason why $La_7P_3O_{18}$ forms only at 1200 °C or higher is that $La_7P_3O_{18}$ may be thermodynamically unstable at low temperatures. To

examine this possibility, $La_7P_3O_{18}$ synthesized at 1300 °C was subjected to long-term heat treatments at 1000, 1100, and 1200 °C with stepwise temperature profiles shown in Figure 3.7.

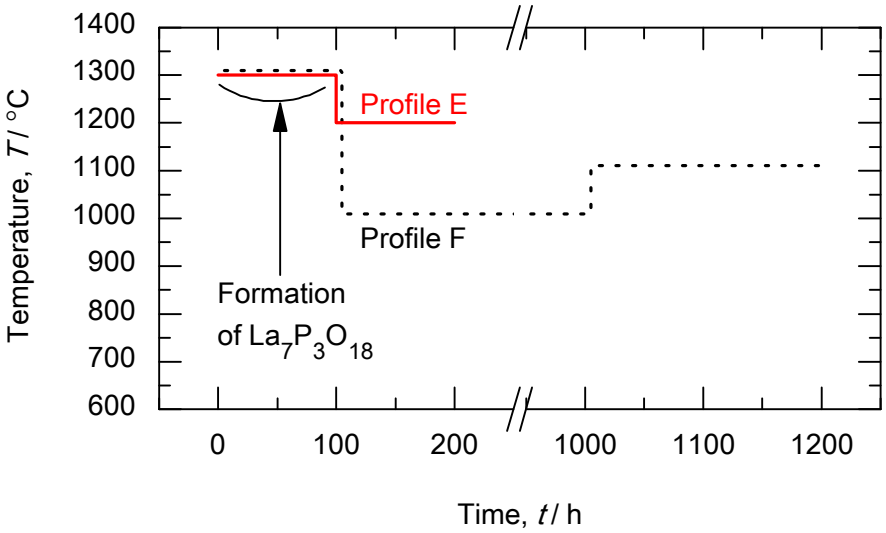

Figure 3.7 Temperature profiles for the heat treatments of $La_7P_3O_{18}$. Occasional cooling to room temperature is not shown in the figure. Overlapping lines are slightly shifted for better visibility.

Figure 3.8 shows the X-ray diffraction patterns of $La_7P_3O_{18}$ obtained after each heat treatment. As can be seen in the figure, all the patterns are essentially the same and representing that the samples consisted of $La_7P_3O_{18}$ in large part and a slight amount of La_3PO_7. No sign of the decomposition of $La_7P_3O_{18}$, the reverse reaction of Eq. (3.3), was detected. Therefore, it can be said that $La_7P_3O_{18}$, once formed at high temperatures, is practically stable at temperatures 1000–1200 °C. However, the thermodynamically stable phase(s) at these temperatures are still unknown and might be revealed by some thermodynamic measurements in the future. Figure 3.9 summarizes the results of the phase equilibrium experiments with L7P3 samples performed in the previous and this subsections.

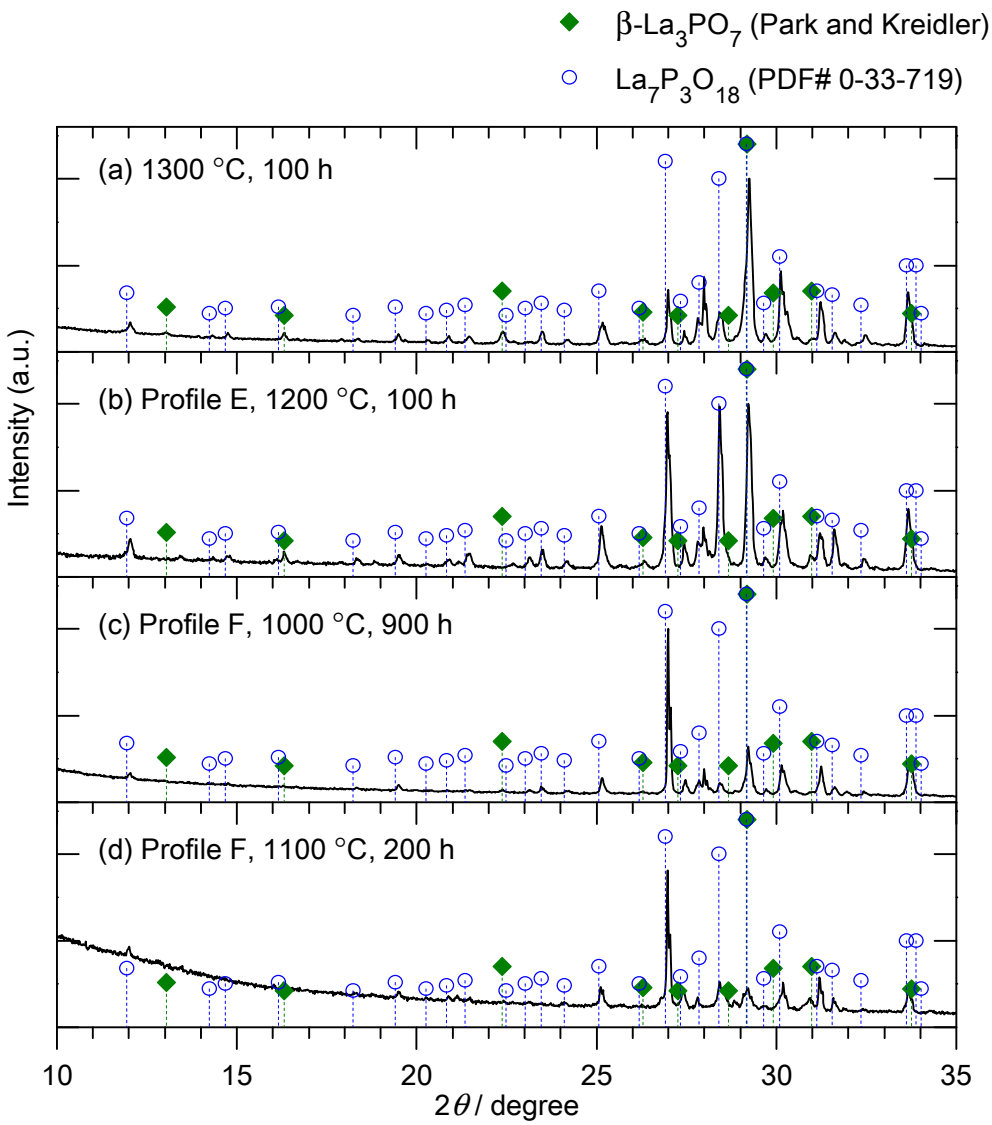

Figure 3.8 X-ray diffraction patterns of $La_7P_3O_{18}$ during heat treatments with temperature profiles indicated in Figure 3.7. (a) After the first heat treatment at 1300 °C for 100 h; (b) After the heat treatment at 1200 °C for 100 h (Profile E); (c) After the heat treatments at 1000 °C for a total of 900 h (Profile F). (d) After the heat treatments at 1100 °C for a total of 200 h (Profile F).

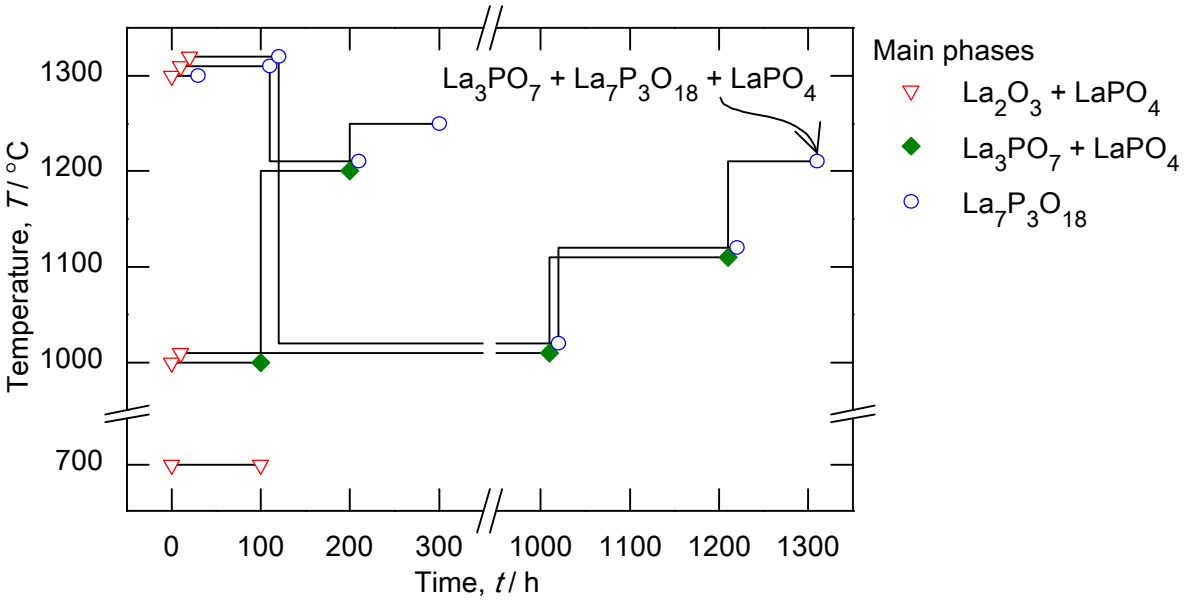

Figure 3.9 Summary of the phase equilibrium experiments with L7P3 samples. The lines represent the temperature profiles and the symbols indicate the phases present after various heat treatments. Overlapping symbols and lines are slightly shifted for better visibility.

3.3.4 $LaPO_4$–LaP_3O_9 Subsystem

The phase relationships between $LaPO_4$ and LaP_3O_9 were examined using the sample L25P75−δ. As described in 3.1.3, the existence of an intermediate compound, $La_2P_4O_{13}$, has been reported between $LaPO_4$ and LaP_3O_9, with the decomposition temperature of 755 °C. To verify whether it is formed or not, L25P75−δ was heat treated at 700 °C for 100 h.

Figure 3.10 shows the X-ray diffraction patterns of L25P75−δ before and after the heat treatment. As can be seen in the figure, both patterns are composed of the peaks of $LaPO_4$ and LaP_3O_9. No other phase such as $La_2P_4O_{13}$ was identified. So far $La_2P_4O_{13}$ has been obtained only by crystallization from glass and it was reported to decompose into $LaPO_4$ and LaP_3O_9 at 755 °C [12].Wong and Kreidler mentioned that $La_2P_4O_{13}$ and $Nd_2P_4O_{13}$ could not be formed by solid state reaction [27]. They speculated that $Nd_2P_4O_{13}$ exists in a metastable state. The present result implies that $La_2P_4O_{13}$ is also a metastable phase.

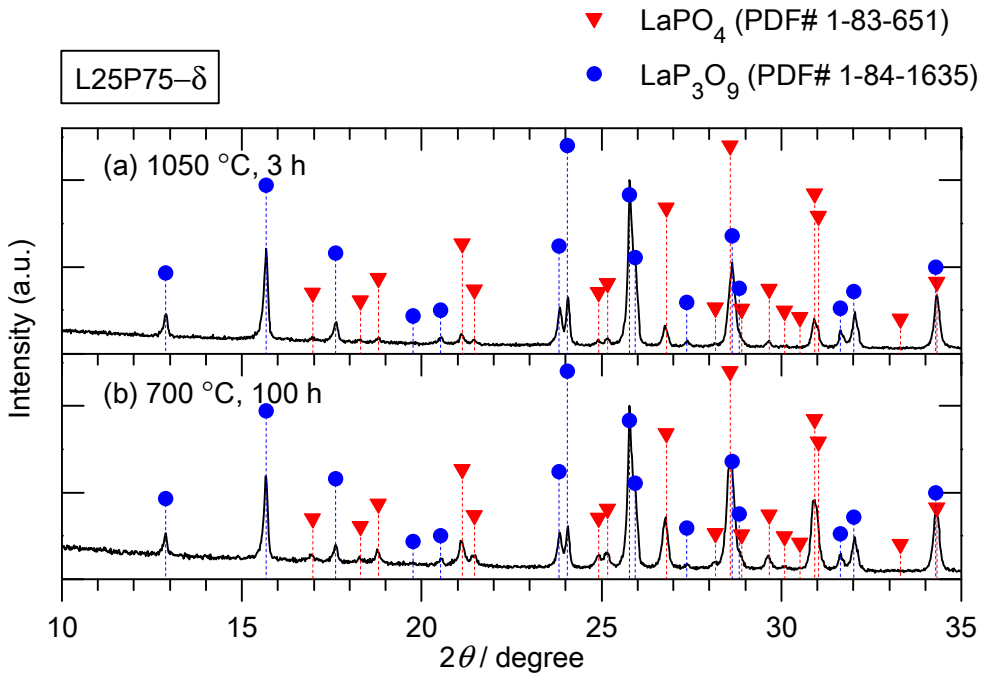

Figure 3.10 X-ray diffraction patterns of L25P75−δ (a) before and (b) after a heat treatment at 700 °C for 100 h.

3.4 Conclusions

In this chapter, the phase equilibria in the La_2O_3–P_2O_5 system were re-examined to verify the known phase diagrams. Two intermediate phases, La_3PO_7 and $La_7P_3O_{18}$, were identified in the La_2O_3–$LaPO_4$ subsystem. La_5PO_{10} was not observed. Therefore, the phase diagram reported by Park and Kreidler seems more likely to be accurate in that. La_3PO_7 was formed at 1000 °C, while $La_7P_3O_{18}$ was only formed at 1200 °C and higher. At 1000 °C, neither the formation nor decomposition of $La_7P_3O_{18}$ took place within 1000 h. This behavior might be due to kinetic reasons, but it was not verified. In the $LaPO_4$–LaP_3O_9 subsystem, no intermediate phase such as $La_2P_4O_{13}$ was detected. $La_2P_4O_{13}$ might be a metastable phase. Based on these results, the phase diagram reported by Park and Kreidler is slightly modified and presented in Figure 3.11. The diagram shows the phases obtainable by solid state reaction, and those possibly in metastable phases are not shown.

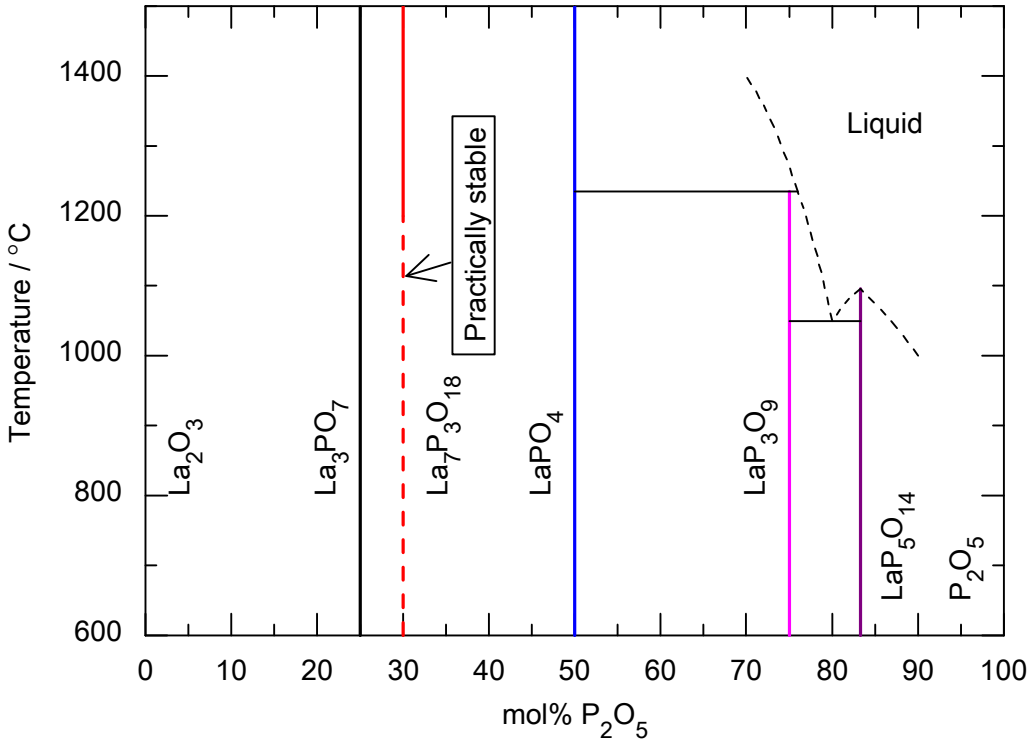

Figure 3.11 Proposed phase diagram of the La_2O_3–P_2O_5 system.

References

[1] R.C. Ropp, J. Electrochem. Soc. 115 (1968) 841-845.

[2] T.C. Damen, H.P. Weber, B.C. Tofield, Appl. Phys. Lett. 23 (1973) 519-520.

[3] E.B. Stucchi, A.M. de Castro, M.A. Couto Dos Santos, P. Melnikov, J. Alloys Compd. 275-277 (1988) 86-88.

[4] S. Lu, J. Zhang, J. Lumin. 122-123 (2007) 500-502.

[5] K. Gunjigake, M. Hasegawa, H. Oizumi, Y. Ogata, United States Patent 4,033,790, July 5, 1977.

[6] G.R. Pickrell, J.E. Rapp, United States Patent 5,350,460, Sep. 27, 1994.

[7] M. Tao, H. Xiao, T. Sun, W. Guo, J. Chin. Ceram. Soc. 38 (2010) 1553-1557.

[8] P.E.D. Morgan, D.B. Marshall, Mater. Sci. Eng. A162 (1993) 15-25.

[9] S.V. Komarov, S.E. Romankov, S.H. Son, N. Hayashi, S.D. Kaloshkin, S. Ueno, E. Kasai, Surf. Coat. Technol. 202 (2008) 5180-5184.

[10] G.J. McCarthy, W.B. White, D.E. Pfoertsch, Mater. Res. Bull. 13 (1978) 1239-1245.

[11] A. Meldrum, L.A. Boatner, R.C. Ewing, Phys. Rev. B 56 (1997) 13805-13814.

[12] H.D. Park, E.R. Kreidler, J. Am. Ceram. Soc. 67 (1984) 23-26.

[13] J. Kropiwnicka, T. Znamierowska, Pol. J. Chem. 62 (1988) 587-594.

[14] G. Harley, R. Yu, L.C. De Jonghe, Solid State Ionics 178 (2007) 769-773.

[15] J. Kropiwnicka, J. Thermal Anal. 36 (1990) 979-990.

[16] E.G. Tselebrovskaya, B.F. Dzhurinskii, A.V. Lavrov, A. Durif, Russ. J. Inorg. Chem. 39 (1994) 473-474.

[17] R. El Ouenzerfi, C. Goutaudier, G. Panczer, B. Moine, M.T. Cohen-Adad, M. Trabelsi-Ayedi, N. Kbir-Ariguib, Solid State Ionics 156 (2003) 209-222.

[18] K. Amezawa, Y. Tomii, N. Yamamoto, Solid State Ionics 175 (2004) 569-573.

[19] J.J. Serra, J. Coutures, A. Rouanet, High Temp. - High Pressures 8 (1976) 337-341.

[20] J.J. Serra, J. Coutures, A. Rouanet, H. Dexpert, G. Garon, Rev. Int. Hautes Temp. Refract. 15 (1978) 287-313.

[21] A. Rouanet, J.J. Serra, K. Allaf, V.P. Orlovskii, Inorg. Mater. 17 (1981) 76-81.

[22] E.G. Tselebrovskaya, B.F. Dzhurinskii, G.V. Lysanova, M.G. Komava, Russ. J. Inorg. Chem. 36 (1991) 1387-1389.

[23] E. Boakye, R.S. Hay, M.D. Petry, J. Am. Ceram. Soc. 82 (1999) 2321-2331.

[24] J.R. Mawdsley, J.W. Halloran, J. Eur. Ceram. Soc. 21 (2001) 751-757.

[25] N.N. Chudinova, L.P. Shklover, G.M. Balagina, Inorg. Mater. 11 (1975) 590-593.

[26] M. Tsuhako, S. Ikeuchi, T. Matsuo, I. Motooka, M. Kobayashi, Bull. Chem. Soc. Jpn. 52 (1979) 1034-1040.

[27] M.-S. Wong, E.R. Kreidler, J. Am. Ceram. Soc. 70 (1987) 396-399.

[28] S. Bernal, J.A. Díaz, R. García, J.M. Rodríguez-Izquierdo, J. Mater. Sci. 20 (1985) 537-541.

[29] E.G. Tselebrovskaya, B.F. Dzhurinskii, O.I. Lyamina, Inorg. Mater. 33 (1997) 52-59.

Chapter 4
Thermodynamic Properties of LaP_3O_9 and LaP_5O_{14}

4.1 Introduction

LaP_3O_9 and LaP_5O_{14} have been demonstrated to decompose gradually at high temperatures by the following reactions [1-5]:

$$LaP_3O_9\ (s) \rightarrow LaPO_4\ (s) + 1/2\ P_4O_{10}\ (g); \quad (4.1)$$

$$LaP_5O_{14}\ (s) \rightarrow LaP_3O_9\ (s) + 1/2\ P_4O_{10}\ (g). \quad (4.2)$$

The decomposition temperatures have been reported to be ~800 °C [1] and ~700 °C [3], respectively. The vapor produced by these reactions can be utilized for phosphorus doping of silicon wafers in the semiconductor industry [6-8]. Meanwhile, because of these decompositions, it is difficult to obtain dense LaP_3O_9 and LaP_5O_{14} electrolytes by conventional sintering method. In fact, dense LaP_3O_9 samples with relative density higher than 0.9 have only been obtained by spark plasma sintering [1]. Moreover, the instability of LaP_3O_9 and LaP_5O_{14} may limit the operating temperatures for the electrolytes, since the decomposition of the electrolytes during fuel cell operation may lead to the degradation of cell performance as well as corrosion of other components. However, very little quantitative information is available about the decomposition reactions. The only available experimental information, the vapor pressure of P_4O_{10} (p_{P4O10}) over LaP_3O_9, was given by Ashuiko *et al*. [5] as follows:

$$\log (p_{P4O10} / \text{mmHg}) = 8.5641 - 13613 \times (T / \text{K})^{-1}$$

$$(1219 \leq T / \text{K} \leq 1404). \quad (4.3)$$

For accurate assessment of the stabilities of LaP_3O_9 and LaP_5O_{14}, further examination and refinement

of their thermodynamic properties will be necessary. In this chapter, vapor pressure measurements on LaP_3O_9 and LaP_5O_{14} were carried out by the transpiration method [9].

4.2 Experimental

4.2.1 Sample Preparation and Phase Identification

LaP_3O_9 and LaP_5O_{14} were synthesized by precipitation in phosphoric acid solutions [10,11]. La_2O_3 (Nacalai Tesque, mass fraction purity 0.9999) and H_3PO_4 (Nacalai Tesque, mass fraction purity 0.85) were mixed at a P/La molar ratio of 15 and kept at 463 K in the air for several days to obtain a transparent solution. Then the solution was kept at 503 or 573 K to precipitate LaP_3O_9 and LaP_5O_{14}. The precipitates were separated from the solution, washed well with hot water and dried at ~90 °C. Then they were ground with a mortar and pestle, and pressed into pellets with weight of ~300 mg and relative density of 0.50–0.75. The LaP_3O_9 and LaP_5O_{14} pellets were heat-treated at 973 K (700 °C) and 873 K (600 °C), respectively, for 50 h in the air to eliminate residual water and phosphoric acid on the surface of samples before further experiments. Phase identification was carried out *via* X-ray powder diffraction (XRD) analysis on PANalytical X'Pert-Pro MPD using Cu Kα radiation.

4.2.2 Vapor Pressure Measurements

4.2.2.1 Apparatus and Procedure

The apparatus used for vapor pressure measurements is shown in Figure 4.1. The sample was placed in a platinum boat of length 110 mm and inserted into a quartz tube of diameter 25 mm. The sample was rapidly heated to the desired temperature (923–1323 K) at a rate of 5 K min^{-1} under a carrier gas flow. Oxygen (O_2) was selected as the carrier gas to ensure that the dominant vapor species is P_4O_{10}. The details are described in the following subsection. The temperature and the

carrier gas flow rate were kept constant for a specified period of time, and then the sample was cooled down at a rate of 5 K min^{-1}. The carrier gas flow rate was controlled by a variable area flow meter (KOFLOC, RK1250) at the gas inlet and checked by another flow meter (Agilent Technologies, ADM 1000) at the outlet. The precision of the flow rate was ±10%, and that of the sample temperature was ± 5 K.

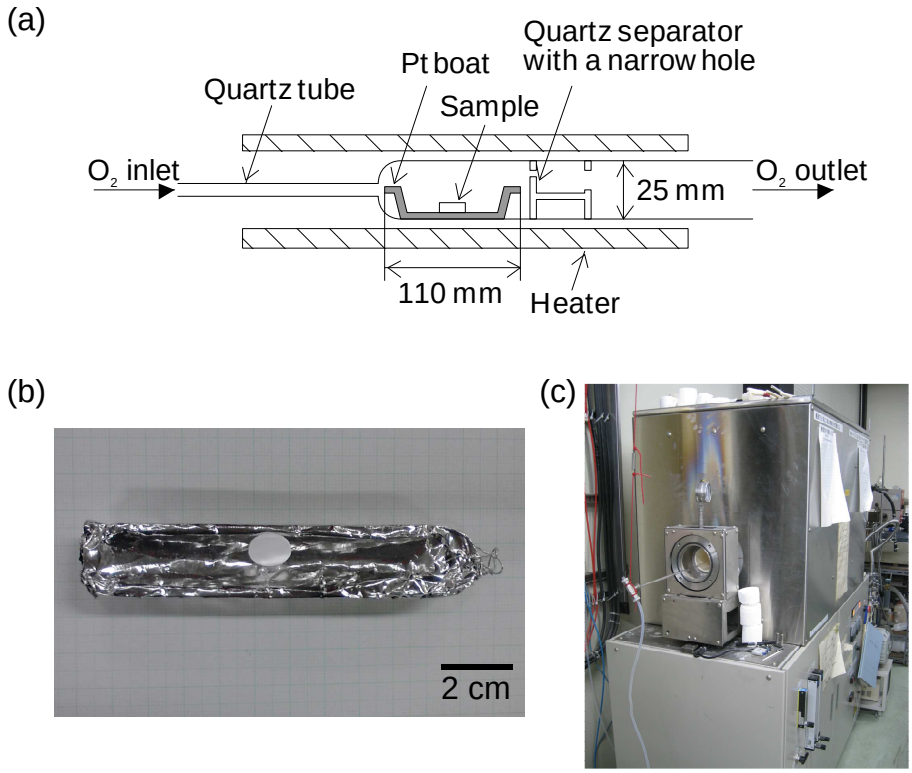

Figure 4.1 (a) Schematic illustration of the apparatus used for the transpiration method. (b) Photo of the platinum boat and a sample pellet. (c) Photo of the furnace and quartz tube inserted in it, taken from the inlet side.

The vapor pressure of P_4O_{10} over the sample, p_{P4O10}, was calculated using the following equation:

$$p_{P4O10} = \frac{n_{P4O10}}{n_{P4O10} + n_{O2}} P_{total}, \qquad (4.4)$$

where n_{P4O10} and n_{O2} are the numbers of moles of P_4O_{10} vapor and O_2 flowed, respectively, and P_{total}

is the total pressure in the quartz tube (1 atm). The value of n_{P4O10} was deduced by

$$n_{P4O10} = \frac{-\Delta w_{sample}}{M_{P4O10}}, \quad (4.5)$$

where Δw_{sample} is the weight change of the sample and M_{P4O10} is the molecular weight of P_4O_{10}. The value of n_{O2} was deduced by

$$n_{O2} = \frac{p_{O2}\, v_{O2}\, t}{R\, T_{room}}, \quad (4.6)$$

where p_{O2} and v_{O2} are the pressure (1 atm) and flow rate of O_2 at the inlet, respectively, t is the holding time, R is the gas constant and T_{room} is room temperature (298 K).

4.2.2.2 Vapor Species

To use the above equations, P_4O_{10} must be the dominant product of evaporation; otherwise, appropriate corrections should be made. Therefore, the partial pressures of known vapor species in the P–O system (P, PO, PO_2, P_2, P_2O_3, P_2O_4, P_2O_5, P_3, P_3O_6, P_4, P_4O_6, P_4O_7, P_4O_8, P_4O_9, and P_4O_{10}) were calculated under various conditions using thermodynamic functions given in the literature [12,13]. It should be noted that widely divergent values have been given for the standard enthalpy of formation ($\Delta_f H°$) of P_4O_6 (g). The NIST-JANAF Thermochemical Tables [12] gives a $\Delta_f H°$ (P_4O_{10}, g, 298.15K) value of −2214 kJ mol^{-1} while Ref. [13] gives a value of −1606 kJ mol^{-1}. As pointed out by several researchers [13-16], the former value is based on a value of $\Delta_f H°$ (P_4O_6, l, 298.15K) [17] which is not necessarily accurate. Therefore, we considered the latter value more reliable and used it for the following calculations.

Figure 4.2 (a) shows the variation of the calculated partial pressures of vapor species in the P–O system with O_2 partial pressure at 1000 K and a constant P_4O_{10} partial pressure of 10^{-6} atm. The P_4O_{10} partial pressure was fixed since it should be thermodynamically determined by $LaP_3O_9/LaPO_4$ or LaP_5O_{14}/LaP_3O_9 equilibria and independent of O_2 partial pressure. The value of 10^{-6} atm is in the

range of measured vapor pressures. From the figure, it is clear that P_4O_{10} is the dominant vapor species especially under high O_2 partial pressures. Then the temperature dependence of the partial pressures of vapor species was examined at an O_2 partial pressure of 1 atm (Figure 4.2 (b)). Although partial pressures of minor vapor species increase with temperature, the partial pressure of P_4O_{10} is still highest in the temperature range of 1000–1400 K. Therefore, O_2 was selected as the carrier gas to ensure that P_4O_{10} is the dominant vapor species in the present study.

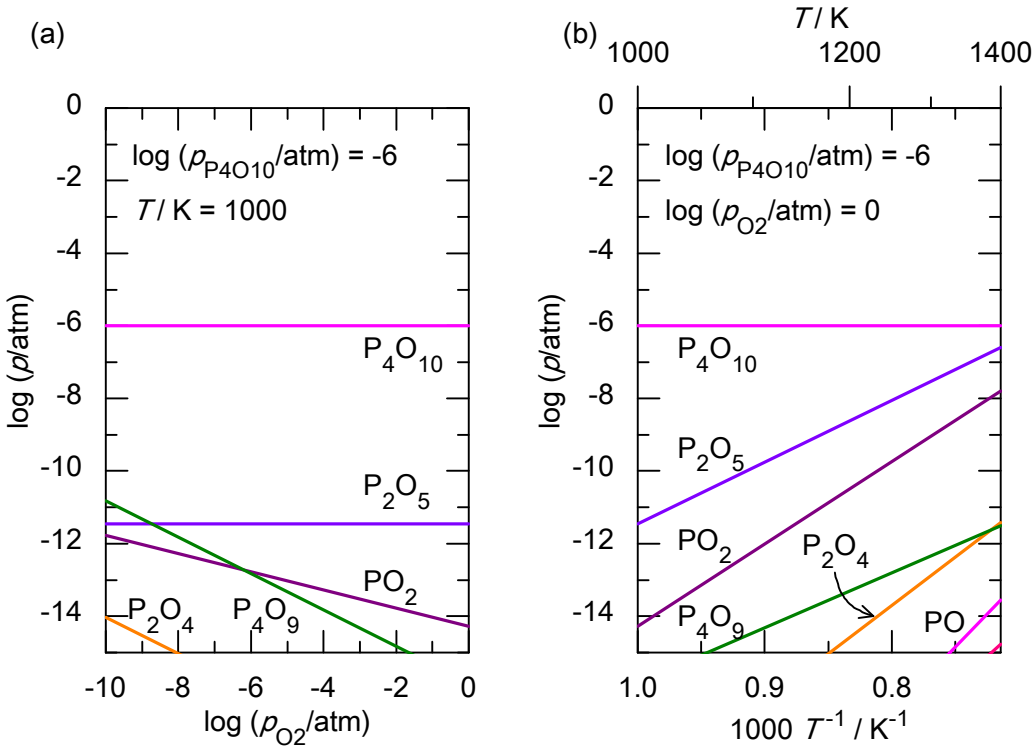

Figure 4.2 Variation of the partial pressures of vapor species in the P–O system. (a) log p_{O2} dependence at temperature T / K =1000 and log (p_{P4O10} / atm) = −6. (b) Temperature dependence at log (p_{P4O10} / atm) = −6 and log (p_{O2} / atm) = 0.

4.3 Results

4.3.1 Equilibrium Conditions

Phase identification of LaP_3O_9 and LaP_5O_{14} samples was carried out by X-ray diffraction

analysis before and after vapor pressure measurements. As shown in Figure 4.3, LaP_3O_9 became a mixture of LaP_3O_9 and $LaPO_4$ after vapor pressure measurements. Likewise, LaP_5O_{14} became a mixture of LaP_5O_{14} and LaP_3O_9. These results are consistent with the reported decomposition reactions (Eqs. (4.1) and (4.2)).

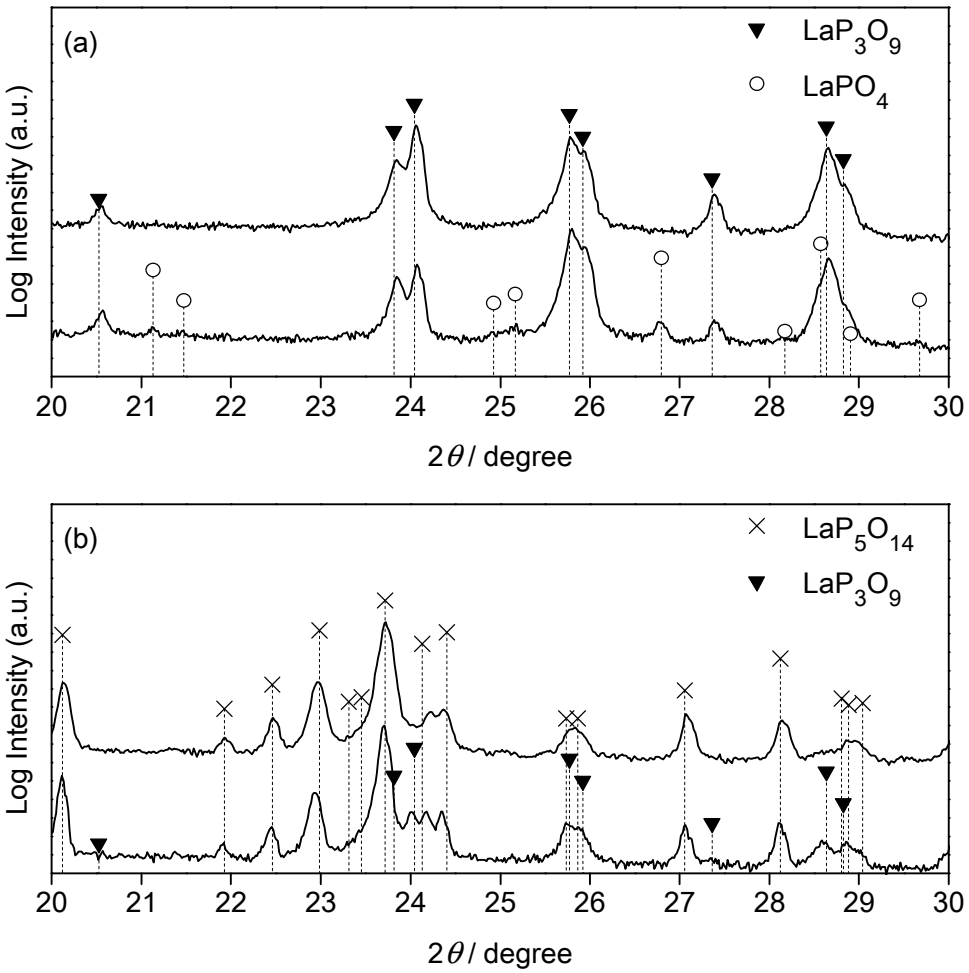

Figure 4.3 Typical X-ray diffraction patterns of (a) LaP_3O_9 and (b) LaP_5O_{14} pellets. The upper and lower patterns in each figure were obtained before and after vapor pressure measurements, respectively. During the vapor pressure measurements, the LaP_3O_9 pellet was held at 1273 K for 10 h and the LaP_5O_{14} pellet was held at 1073 K for 3 h. Peaks marked with ○, ▼ and × are attributed to $LaPO_4$ (PDF# 1-83-651), LaP_3O_9 (PDF# 1-84-1635) and LaP_5O_{14} (PDF# 1-70-5341), respectively.

To establish the conditions where the carrier gas (O_2) is saturated with P_4O_{10} vapor, variation of the apparent P_4O_{10} vapor pressure with O_2 flow rate was examined (Figure 4.4). The plateau region, where the vapor pressure is independent of the flow rate, was found to be in the flow rate range of 20–50 sccm. In the plateau region, equilibrium vapor pressures can be obtained without any correction for diffusional transport or kinetic effects [9]. In addition, the number of sample pellets inserted simultaneously in the apparatus did not have any marked effect on the above behavior. This indicates that enough evaporation rates were achieved with only one pellet. Therefore, all further vapor pressure measurements were carried out at an O_2 flow rate of 25 sccm with one sample pellet inserted in the apparatus.

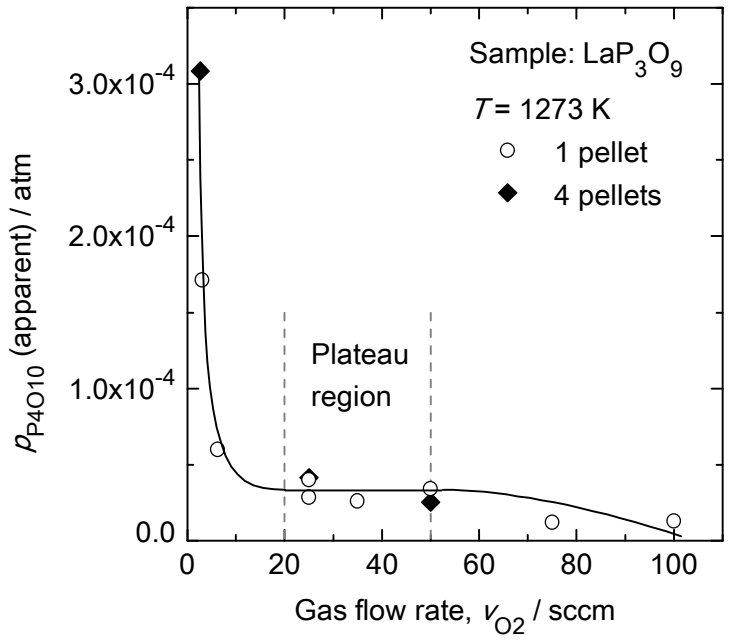

Figure 4.4 Apparent vapor pressures of P_4O_{10} over LaP_3O_9, p_{P4O10} (apparent), as a function of gas flow rate v_{O2} at 1273 K: ○, data obtained with a pellet; ♦, data obtained with four pellets.

4.3.2 Temperature Dependence of Vapor Pressures

The equilibrium vapor pressures of P_4O_{10} over LaP_3O_9 and LaP_5O_{14} were examined in the temperature range of 1123–1323K and 923–1173K, respectively. The vapor pressures obtained in each measurement are listed in Table 4.1. The logarithmic plot of the vapor pressures against

reciprocal temperature is shown in Figure 4.5. The least squares lines are given by

$$\log (p_{P4O10} / \text{atm}) = (5.12\pm1.00) - (1.22\pm0.12) \times 10^4 \times (T / \text{K})^{-1}$$

(over LaP_3O_9); (4.7)

$$\log (p_{P4O10} / \text{atm}) = (4.65\pm1.80) - (1.00\pm0.19) \times 10^4 \times (T / \text{K})^{-1}$$

(over LaP_5O_{14}), (4.8)

where each value is shown with two standard error range which provides 95% confidence. Our experimental data on LaP_3O_9 are in reasonable agreement with those reported by Ashuiko *et al*. [5]

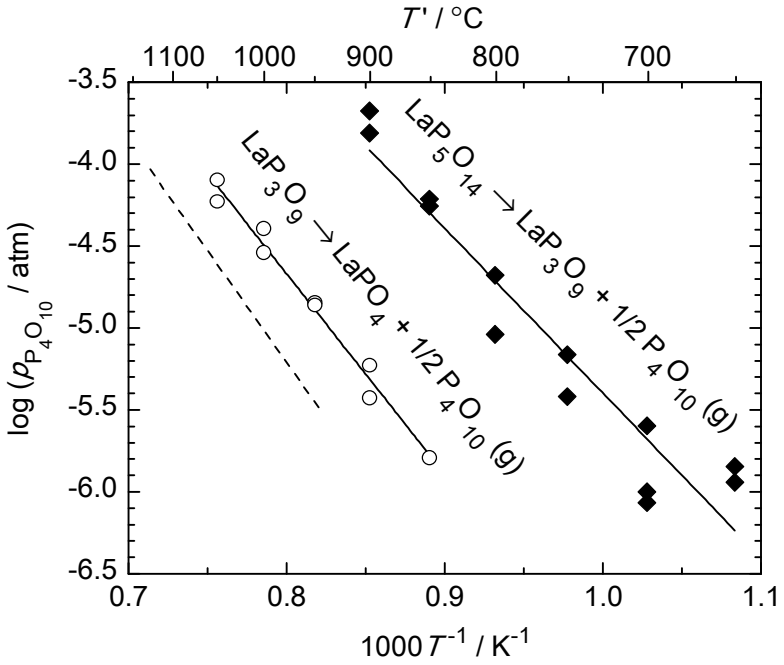

Figure 4.5 Temperature dependence of the vapor pressure of P_4O_{10}, p_{P4O10}: ○, p_{P4O10} over LaP_3O_9; ♦, p_{P4O10} over LaP_5O_{14}; ——, least-squares lines to the experimental data; - - - -, p_{P4O10} over LaP_3O_9 given by Ashuiko *et al*. [5].

Table 4.1 Weight losses of samples $-\Delta w_{sample}$ and the vapor pressures of P_4O_{10} p_{P4O10} at gas flow rate v_{O2} and temperature T with holding time t.

Sample	v_{O2} / sccm	T / K	t / h	$-\Delta w_{sample}$ / mg	p_{P4O10} [a] / atm
LaP_3O_9	25	1123	50	1.4	1.61×10^{-6}
LaP_3O_9	25	1173	35	3.6	5.90×10^{-6}
LaP_3O_9	25	1173	20	1.3	3.73×10^{-6}
LaP_3O_9	25	1223	10	2.4	1.38×10^{-5}
LaP_3O_9	25	1223	2	0.5	1.43×10^{-5}
LaP_3O_9	25	1273	5	2.5	2.87×10^{-5}
LaP_3O_9	25	1273	2	1.4	4.02×10^{-5}
LaP_3O_9	25	1323	3	3.1	5.93×10^{-5}
LaP_3O_9	25	1323	3	4.2	8.03×10^{-5}
LaP_5O_{14}	25	923	80	2.0	1.43×10^{-6}
LaP_5O_{14}	25	923	60	1.2	1.15×10^{-6}
LaP_5O_{14}	25	973	40	0.7	1.00×10^{-6}
LaP_5O_{14}	25	973	25	1.1	2.52×10^{-6}
LaP_5O_{14}	25	973	20	0.3	8.61×10^{-7}
LaP_5O_{14}	25	1023	15	1.0	3.83×10^{-6}
LaP_5O_{14}	25	1023	10	1.2	6.89×10^{-6}
LaP_5O_{14}	25	1073	10	1.6	9.18×10^{-6}
LaP_5O_{14}	25	1073	3	1.1	2.10×10^{-5}
LaP_5O_{14}	25	1123	3	2.9	5.55×10^{-5}
LaP_5O_{14}	25	1123	3	3.2	6.12×10^{-5}
LaP_5O_{14}	25	1173	3	8.1	1.54×10^{-4}
LaP_5O_{14}	25	1173	3	11.1	2.12×10^{-4}

[a] Derived from v_{O2}, t and $-\Delta w_{sample}$.

4.4 Discussion

4.4.1 Thermodynamic Properties of LaP_3O_9 and LaP_5O_{14}

The thermodynamic properties of the decomposition reactions (Eqs. (4.1) and (4.2)) were determined from the results of vapor pressure measurements. The slopes and intercepts of the least-squares lines in Figure 4.5 (Eqs. (4.4) and (4.5)) yield the second-law values of standard

enthalpies and entropies of the decomposition reactions, shown in Table 4.2. The corresponding values based on the literature [5,18] are also listed in the table. The standard enthalpy of decomposition of LaP_5O_{14} (Eq. (4.2)) was estimated from the specifications of a commercial phosphorus diffusion source made of LaP_5O_{14} (Techneglas, Inc., PhosPlus TP-250). In the brochure [18], the thicknesses of deposited glassy film using the diffusion source at various temperatures (1098–1223 K) are given. Assuming that the thickness is proportional to the vapor pressure of P_4O_{10}, one can obtain the standard enthalpy of decomposition by the second law treatment. Our present values and those from the literature are in reasonable agreement.

Table 4.2 Thermodynamic properties of the decomposition reactions of LaP_3O_9 and LaP_5O_{14}.

Reaction	Source	Method	$\Delta H°$ / kJ mol^{-1}	$\Delta S°$ / J mol^{-1} K^{-1}	T / K
(4.1)	This work	Second-law	117 ± 12	49 ± 10	1123–1323
	Ref. [5]	Second-law	130	54	1219–1404
(4.2)	This work	Second-law	96 ± 18	45 ± 17	923–1173
	Ref. [18]	Second-law	113 ± 18	Unavailable	1098–1223

4.4.2 Thermal and Chemical Stabilities of LaP_3O_9 and LaP_5O_{14}

As mentioned in the introduction, LaP_3O_9 and LaP_5O_{14} have been considered as candidates for solid proton-conducting electrolytes in fuel cells. In general, lifetimes greater than 40000 h are required for stationary fuel cell systems [19]. To meet the requirement, electrolytes in fuel cells should have sufficient thermal and chemical stability. As for LaP_3O_9 and LaP_5O_{14} electrolytes, their operation conditions should be limited to suppress the decomposition.

4.4.2.1 Operating Temperatures for the Electrolytes in Oxygen Atmosphere

The lifetime target of stationary fuel cells is the time until 10% power degradation [19]. Since the relationship between power degradation and the decomposition ratios of the electrolytes is unknown, a decomposition ratio of 0.01 (1%) was taken as the threshold in the following discussion

to obtain safer values. In the present study, a sign of decomposition (weight fraction loss of 5×10^{-3}; decomposition ratio of ~0.01) was detected in 50 h when the vapor pressure of P_4O_{10} was about 10^{-6} atm (for example, see the first row in Table 4.1). Although the dimensions of electrolytes and gas flow rates in actual fuel cell systems may be different from those in this study, the above observation could be basically applicable. Therefore, for long-term (> 40000 h) stability, the vapor pressure of P_4O_{10} should be lowered to ~10^{-9} atm. The second-law extrapolation of the vapor pressures of P_4O_{10} to 10^{-9} atm using Eqs. (4.4) and (4.5) gives the temperatures 864 K (591 °C) and 733 K (460 °C), respectively. Thus, the upper limits of the operating temperatures for LaP_3O_9 and LaP_5O_{14} electrolytes are estimated to be about 600 °C and 450 °C. At these temperatures, the proton conductivity of 5% Sr-doped LaP_3O_9 is ~2.5×10^{-4} S cm^{-1} [20] whereas that of 5% Sr-doped LaP_5O_{14} is ~1.3×10^{-5} S cm^{-1} [21]. Therefore, it can be said that LaP_3O_9 based electrolytes are more promising than LaP_5O_{14} based ones.

4.4.2.2 Stabilities in the Presence of Water and Hydrogen

Proton conducting electrolytes in practical fuel cells are used in the presence of water vapor and hydrogen. Therefore, the stabilities of the LaP_3O_9 and LaP_5O_{14} electrolytes in such conditions should also be assessed. Various vapor species can be formed by their reactions with water vapor and hydrogen:

$$y\mathrm{LaP_3O_9\,(s)} + (x+5y-2z)\mathrm{H_2\,(g)} + (-5y+2z)\mathrm{H_2O\,(g)} \rightarrow y\mathrm{LaPO_4\,(s)} + 2\mathrm{H}_x\mathrm{P}_y\mathrm{O}_z\,\mathrm{(g)}; \quad (4.9)$$

$$y\mathrm{LaP_5O_{14}\,(s)} + (x+5y-2z)\mathrm{H_2\,(g)} + (-5y+2z)\mathrm{H_2O\,(g)} \rightarrow y\mathrm{LaP_3O_9\,(s)} + 2\mathrm{H}_x\mathrm{P}_y\mathrm{O}_z\,\mathrm{(g)}. \quad (4.10)$$

$H_xP_yO_z$ (g) is a general expression for the vapor species. Here, PH, PH_2, PH_3, HPO, HPO_2, and HPO_3 were considered in addition to the P–O vapor species considered in 4.2.2.2. The equilibrium partial pressures of each vapor species were calculated by these equations using our present results and

thermodynamic data in the literature. The standard enthalpies of formation and Gibbs energy functions of PH, PH_2, and PH_3 were taken from Ref. [12]. Those of HPO were taken from Refs. [13,22]. For HPO_2 and HPO_3, the standard enthalpies of formation were taken from Ref. [22] and the Gibbs energy functions were calculated in the "rigid rotator-harmonic oscillator" approximation using the molecular constants given in Ref. [22]. The calculated values of the thermodynamic functions of HPO_2 and HPO_3 are tabulated in Table 4.3. Figure 4.6 shows the calculated partial pressures over LaP_3O_9 at 864 K both in oxygen and hydrogen atmospheres as a function of water vapor pressure, p_{H2O}. In oxygen atmosphere (Figure 4.6 (a)), the vapor pressure of HPO_3 increases with increasing p_{H2O} and exceeds the vapor pressure of P_4O_{10}. This indicates that decomposition of LaP_3O_9 will be accelerated in the presence of water vapor with evaporation of HPO_3. The effect of hydrogen is more drastic as can be seen in Figure 4.6 (b). In hydrogen atmosphere, the partial pressures of various vapor species in lower oxidation states such as HPO_2 and P_4 become several orders of magnitude greater than that of P_4O_{10}. Therefore, the stability of LaP_3O_9 in hydrogen atmosphere can be much poorer than that in oxygen atmosphere. As shown in Figure 4.7, the vapor pressures over LaP_5O_{14} were also found to have the similar dependencies on surrounding atmosphere. These results suggest that the operating atmospheres for the LaP_3O_9 and LaP_5O_{14} should be carefully chosen to prevent their decomposition. For example, in hydrogen atmospheres, decreasing p_{H2} and p_{H2O} simultaneously will lower the overall vapor pressure of phosphorus-containing vapor species as shown in Figure 4.8. Finally, as these effects were only derived from the thermodynamic calculations, future work will have to confirm these phenomena by experiment and examine kinetic aspects.

Table 4.3 Thermodynamic functions of HPO_2 and HPO_3 calculated using their molecular constants [22]. All values are in J mol^{-1} K^{-1} if not otherwise specified.

T / K	HPO_2			HPO_3		
	C_p	S	*gef*	C_p	S	*gef*
298.15	50.2	264.9	−264.9	62.7	277.8	−277.8
300	50.4	265.2	−264.9	62.9	278.2	−277.8
400	55.9	280.5	−266.9	71.4	297.5	−280.3
500	60.1	293.5	−271.0	77.7	314.1	−285.5
600	63.4	304.7	−275.7	82.5	328.7	−291.5
700	65.9	314.7	−280.6	86.1	341.7	−297.8
800	67.9	323.6	−285.4	89.0	353.4	−304.0
900	69.6	331.7	−290.1	91.3	364.1	−310.1
1000	71.0	339.1	−294.6	93.2	373.8	−316.0
1100	72.3	345.9	−299.0	94.9	382.7	−321.6
1200	73.3	352.3	−303.2	96.2	391.1	−327.1
1300	74.3	358.2	−307.2	97.4	398.8	−332.3
1400	75.1	363.7	−311.0	98.5	406.1	−337.3

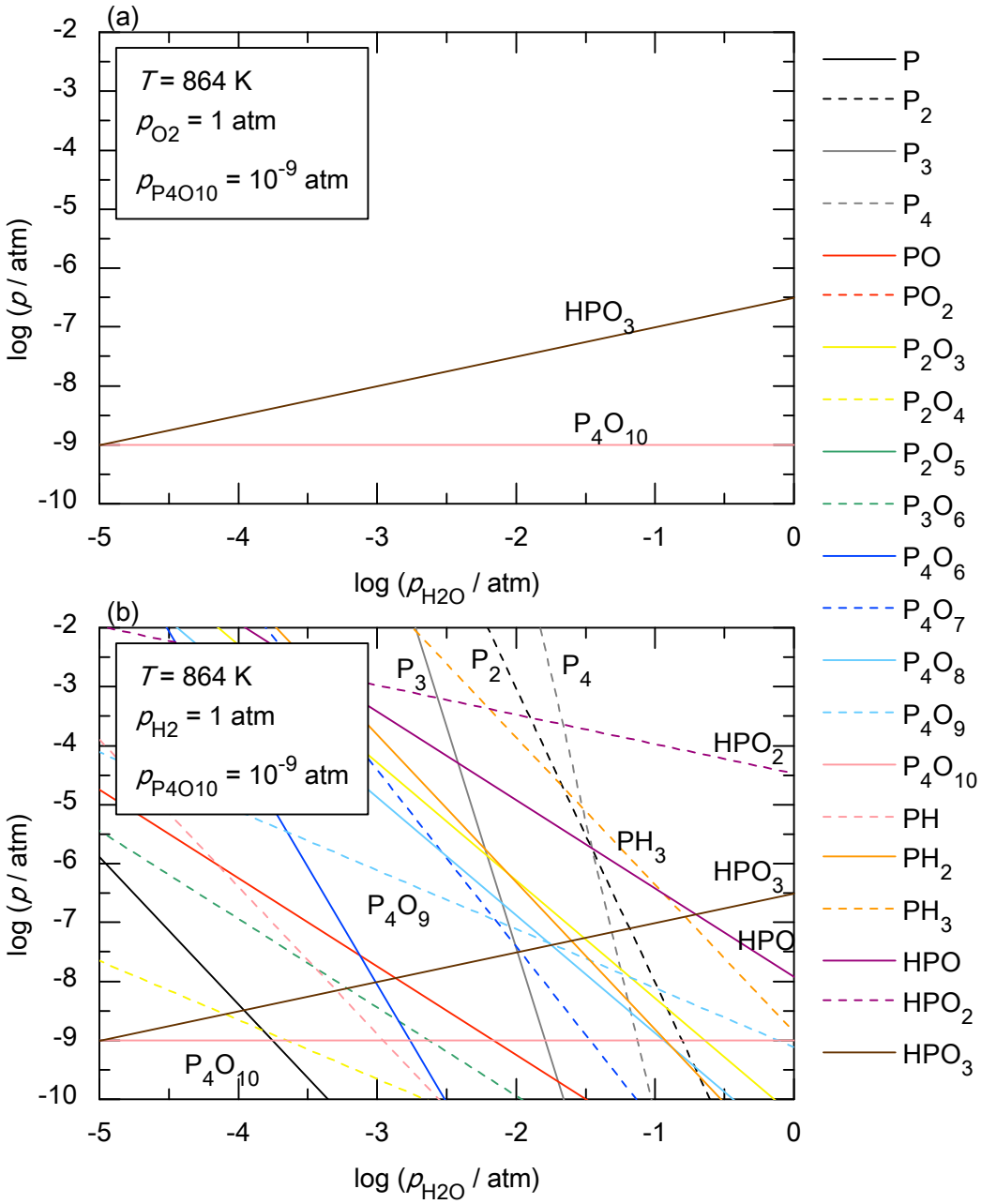

Figure 4.6 Partial pressures of vapor species over LaP_3O_9 at 864 K as a function of water vapor pressure, p_{H2O}. (a) Under 1 atm O_2; (b) under 1 atm H_2.

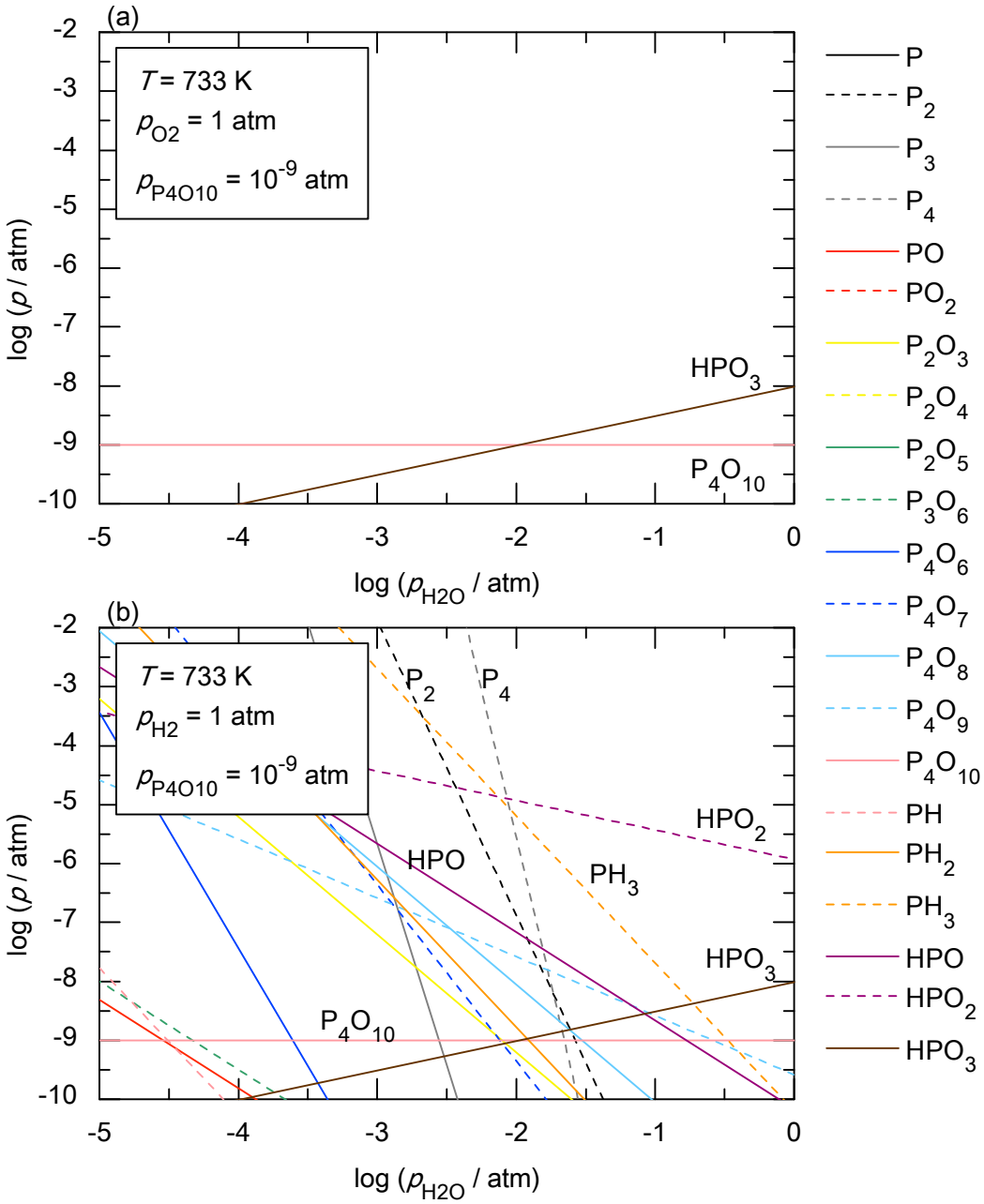

Figure 4.7 Partial pressures of vapor species over LaP_5O_{14} at 733 K as a function of water vapor pressure, p_{H2O}. (a) Under 1 atm O_2; (b) under 1 atm H_2.

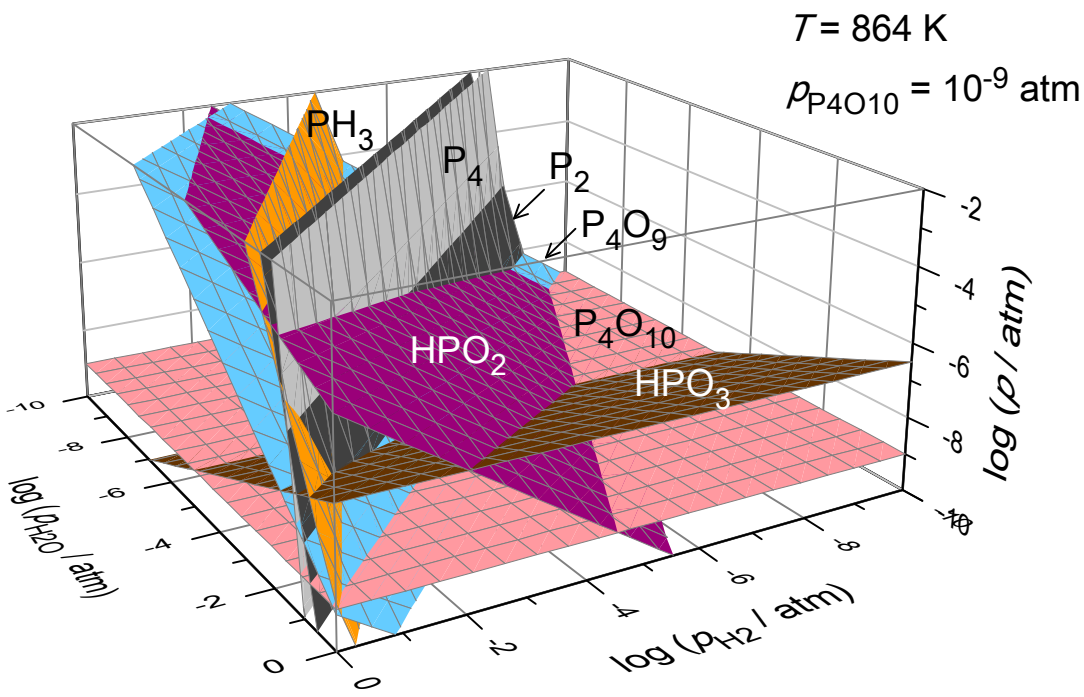

Figure 4.8 Partial pressures of selected vapor species over LaP_3O_9 at 864 K as a function of p_{H2O} and p_{H2}.

4.4.3 Re-examination of the Thermodynamic Data of P_4O_6

Finally, validity of the thermodynamic data of P_4O_6 in the literature was re-examined. In this study, a value of $\Delta_f H^\circ$ (P_4O_6, g, 298.15 K) = −1606 kJ mol^{-1} [13] was adopted while NIST-JANAF Thermochemical Tables [12] provide $\Delta_f H^\circ$ (P_4O_6, g, 298.15 K) = −2214 kJ mol^{-1}. If the value of −2214 kJ mol^{-1} was used instead, P_4O_6 partial pressure over LaP_3O_9 would be as high as 10^{16} atm at 864 K and p_{H2O}/p_{H2} = 1. However, such an extremely fast decomposition of LaP_3O_9 in hydrogen atmosphere has never been reported [20,23]. Therefore, the value in Ref. [13] seems more reliable, which is in agreement with several researchers [14-16]. In light of this conclusion, some work on the vapor phase equilibria in the P-O system [24] has to be reviewed again.

4.5 Conclusions

The vapor pressures of P_4O_{10} produced by decomposition of LaP_3O_9 and LaP_5O_{14} ($LaP_3O_9 \rightarrow LaPO_4 + 1/2\ P_4O_{10}$; $LaP_5O_{14} \rightarrow LaP_3O_9 + 1/2\ P_4O_{10}$) were measured by the transpiration method. The equilibrium vapor pressures of P_4O_{10} over LaP_3O_9 and LaP_5O_{14} can be expressed as

$$\log (p_{P4O10} / \text{atm}) = (5.12 \pm 1.00) - (1.22 \pm 0.12) \times 10^4 \times (T / \text{K})^{-1}$$

(over LaP_3O_9, $1123 \leq T / \text{K} \leq 1323$);

$$\log (p_{P4O10} / \text{atm}) = (4.65 \pm 1.80) - (1.00 \pm 0.19) \times 10^4 \times (T / \text{K})^{-1}$$

(over LaP_5O_{14}, $923 \leq T / \text{K} \leq 1173$).

The standard enthalpies of the evaporation reactions are given as 117±12 kJ mol^{-1} and 96±18 kJ mol^{-1} in the corresponding temperature ranges. The data were evaluated with respect to the proposed use of LaP_3O_9 and LaP_5O_{14} as solid electrolytes in fuel cells. The maximum operating temperatures for the LaP_3O_9 and LaP_5O_{14} electrolytes were suggested to be about 600 °C and 450 °C in oxygen atmosphere. Taking into account their proton conductivities at these temperatures, it can be said that LaP_3O_9 based electrolytes are more promising than LaP_5O_{14} based ones. In the presence of water vapor or hydrogen, however, decomposition of LaP_3O_9 and LaP_5O_{14} would be accelerated considerably.

References

[1] K. Amezawa, Y. Kitajima, Y. Tomii, N. Yamamoto, Electrochem. Solid-State Lett. 7 (2004) A511-A514.

[2] H.D. Park, E.R. Kreidler, J. Am. Ceram. Soc. 67 (1984) 23-26.

[3] W. Jungowska, T. Znamierowska, Mater. Chem. Phys. 48 (1997) 230-233.

[4] O.A. Serra, E. Giesbrecht, J. Inorg. Nucl. Chem. 30 (1968) 793-799.

[5] V.A. Ashuiko, I.A. Rat'kovskii, M.I. Kuz'menkov, N.M. Sergeeva, Izv. Vyssh. Uchebn. Zaved., Khim. Khim. Tekhnol. 18 (1975) 675.

[6] K. Gunjigake, M. Hasegawa, H. Oizumi, Y. Ogata, United States Patent 4,033,790, July 5, 1977.

[7] G.R. Pickrell, J.E. Rapp, United States Patent 5,350,460, Sep. 27, 1994.

[8] M. Tao, H. Xiao, T. Sun, W. Guo, J. Chin. Ceram. Soc. 38 (2010) 1553-1557.

[9] U. Merten, W.E. Bell, in: J.L. Margrave, (Ed.), The Characterization of High-Temperature Vapors, John Wiley & Sons, Inc., New York, 1967, pp. 91-114.

[10] N.N. Chudinova, L.P. Shklover, G.M. Balagina, Inorg. Mater. 11 (1975) 590-593.

[11] G.M. Balagina, N.N. Chudinova, E.V. Murashova, Russ. J. Inorg. Chem. 49 (2004) 614-616.

[12] M.W. Chase Jr., NIST-JANAF Thermochemical Tables, fourth ed., J. Phys. Chem. Ref. Data, Monograph No. 9, 1998.

[13] L.V. Gurvich, I.V. Veyts, and C.B. Alcock, (Eds.), Thermodynamic Properties of Individual Substances, 4th ed., Vol. 1, Hemisphere, New York, 1989.

[14] S.B. Hartley, J.C. McCoubrey, Nature 198 (1963) 476.

[15] D.W. Muenow, O.M. Uy, J.L. Margrave, J. Inorg. Nucl. Chem. 32 (1970) 3459-3467.

[16] S. Smoes, J. Drowart, Faraday Symp. Chem. Soc. 8 (1973) 139-148.

[17] W.E. Koerner, F. Daniels, J. Chem. Phys. 20 (1952) 113-115.

[18] Techneglas, Inc., PhosPlus (R) Brochure, http://www.techneglas.com/dopantpages/pdf/PhosPlusbro.pdf (accessed July 19, 2011).

[19] R. Borup et al., Chem. Rev. 107 (2007) 3904-3951.

[20] K. Amezawa, Y. Uchimoto, Y. Tomii, Solid State Ionics 177 (2006) 2407-2411.

[21] S.R. Phadke, J.C. Nino, J. Am. Ceram. Soc. 94 (2011) 1817-1823.

[22] D.L. Hildenbrand, K.H. Lau, J. Chem. Phys. 100 (1994) 8373-8376.

[23] V. Nalini, R. Haugsrud, T. Nolby, Solid State Ionics 181 (2010) 1264-1269.

[24] J.R. Flemish, R.E. Tressler, J. Electrochem. Soc. 138 (1991) 3743-3747.

Chapter 5
Synthesis of Highly Sr-doped $LaPO_4$ and LaP_3O_9

5.1 Introduction

As mentioned in Chapter 1, the low solubilities of Sr in $LaPO_4$ and LaP_3O_9 have been reported to be relatively low. According to Amezawa *et al*., the solubility of Sr, represented by the molar ratio Sr/(La+Sr), is ~2 mol% in $LaPO_4$ [1] and below 5 mol% in LaP_3O_9 [2]. This is considered as an obstacle to enhancing the conductivities of lanthanum phosphates. Nevertheless, previous studies suggest that the solubility of Sr would have dependence on temperature, and higher Sr doping levels would be expected at lower temperatures. Besides temperature, water vapor pressure may also affect the solubility of Sr. When Sr is doped into a lanthanum phosphate such as $LaPO_4$, a certain amount of water would also be introduced into $LaPO_4$ as represented by the following expression:

$$(1-x)\ LaPO_4 + (x/2)\ Sr_2P_2O_7 + (y/2)\ H_2O \rightarrow La_{1-x}Sr_xH_yPO_{4-(x/2)+(y/2)}. \quad (5.1)$$

Therefore, Sr-doped $LaPO_4$ ($La_{1-x}Sr_xH_yPO_{4-(x/2)+(y/2)}$) would be stabilized with higher water vapor pressure. However, the relationship between the solubility of Sr and these parameters has not been clarified yet.

In Chapter 2, the precipitation conditions for undoped $LaPO_4$ and LaP_3O_9 in homogeneous phosphoric acid solutions were established. In this chapter, further attempts were made to synthesize Sr-doped $LaPO_4$ and LaP_3O_9 in phosphoric acid solutions. The condition dependence of the Sr doping level was analyzed to reveal the optimum condition for obtaining highly Sr-doped phosphates. The incorporation of Sr and H_2O in the $LaPO_4$ lattice was verified by unit cell volume change and

evaporation of H_2O. The incorporation of Sr in the LaP_3O_9 lattice was verified similarly. Finally, the stability of Sr-doped $LaPO_4$ at high temperatures was investigated.

5.2 Experimental

5.2.1 Synthesis

Sr-doped $LaPO_4$ and LaP_3O_9 were synthesized by precipitation in homogeneous phosphoric acid solutions containing La_2O_3 and $SrCO_3$. La_2O_3 (99.99%, Nacalai Tesque), $SrCO_3$ (99.99%, Wako Pure Chemical Industries), and H_3PO_4 (85%, Nacalai Tesque) were mixed in a perfluoroalkoxy (PFA) beaker and held at 190 °C in a furnace for several days to obtain a transparent solution. Then temperature and water vapor pressure were changed and held for a predetermined period of time to precipitate lanthanum phosphates. The temperature was set between 120 °C and 250 °C, and the water vapor pressure was set to approximately 0.01 atm (atmospheric conditions) or 1 atm (humidified conditions). Synthesis parameters are summarized in Table 5.1 and Table 5.2. The precipitation conditions are also plotted on the phase stability diagram of the La_2O_3–P_2O_5–H_2O system constructed in Chapter 2, Figure 5.1.

Table 5.1 Initial compositions of solutions for the synthesis of $LaPO_4$ and LaP_3O_9

Abbr.	Starting materials	Initial composition	
		Molar ratio La : Sr : P	$\left(\frac{Sr}{La+Sr}\right)$ (mol%)
Sr4	La_2O_3, $SrCO_3$, H_3PO_4	0.96 : 0.04 : 15	4
Sr8		0.92 : 0.08 : 15	8
Sr12		0.88 : 0.12 : 15	12
Sr16		0.84 : 0.16 : 15	16
Sr20		0.80 : 0.20 : 15	20
Sr30		0.70 : 0.30 : 15	30
Sr40		0.60 : 0.40 : 15	40
Sr50		0.50 : 0.50 : 15	50
Sr60		0.40 : 0.60 : 15	60
Sr80		0.20 : 0.80 : 15	80

Table 5.2 Dissolution and precipitation conditions for the synthesis of $LaPO_4$ and LaP_3O_9.

Abbr.	Dissolution		Precipitation		Product
	Temp. / °C	p_{H2O} / atm	Temp. / °C	p_{H2O} / atm	
A230	190	~0.01	230	~0.01	LaP_3O_9
A120			120	~0.01	$LaPO_4$
H250			250	~1	$LaPO_4$
H120			120	~1	$LaPO_4$

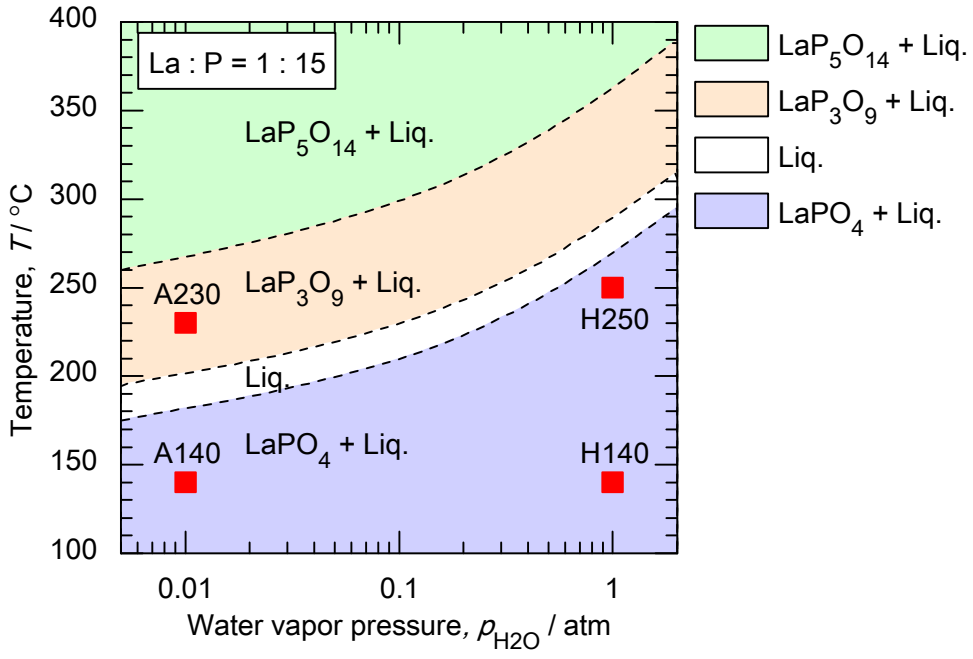

Figure 5.1 Phase stability diagram of the La_2O_3–P_2O_5–H_2O system with a constant La/P ratio (La : P = 1 : 15). The precipitation conditions listed in Table 5.2 are plotted in the figure.

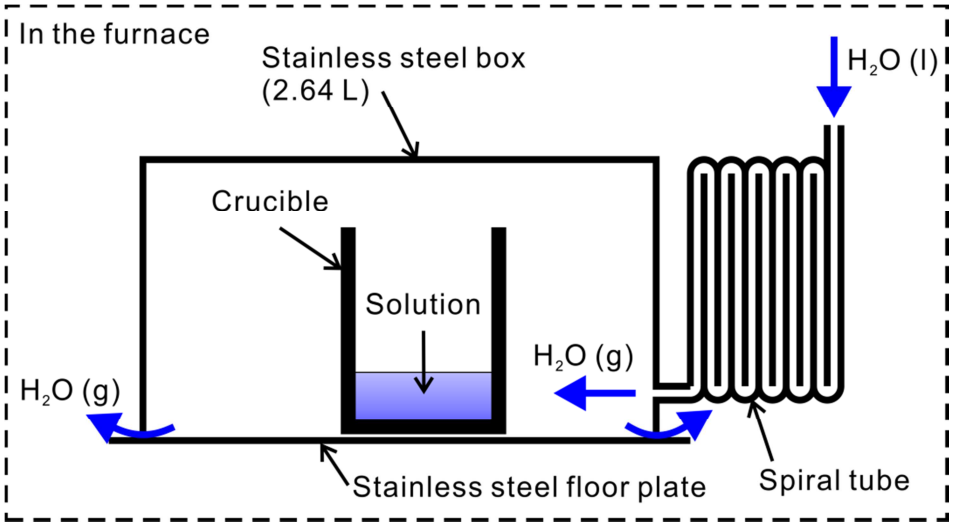

Figure 5.2 Schematic illustration of the apparatus used for humidification during the precipitation of $LaPO_4$.

For humidification, the apparatus shown in Figure 5.2 was used. The whole apparatus was placed in a furnace kept at a constant temperature. A beaker was put on a stainless steel floor plate and covered with a stainless steel box with a capacity of 2.64 L. A 4-m-long spiral tube was attached to a side wall of the box. Liquid water was fed to the box through the spiral tube so that it evaporated

before reaching the box. The liquid water feed rate was 0.1 mL/min, which was equivalent to 0.18 L-H_2O(g)/min at 120 °C and 0.24 L-H_2O(g)/min at 250 °C. The apparatus was not sealed tightly, so that the inner gas was able to flow out through the narrow gap between the box and the floor plate when the inner pressure exceeded 1 atm. Therefore, the water vapor pressure inside the box was expected to be 1 atm.

After the predetermined precipitation period, the beaker was cooled down to room temperature. In general, there were precipitates on the bottom of the beaker and the transparent solution above them. The residual solution was collected for the chemical analysis. The precipitates were washed well with hot water (~90 °C).

5.2.2 Characterization

Phase identification was carried out via X-ray powder diffraction (XRD) analysis on PANalytical X'Pert-Pro MPD using Cu-Kα radiation at room temperature. The unit cell volume of samples was evaluated by the Rietveld method using X'Pert HighScore Plus (Version 2.2c) software. The morphology of precipitates was investigated using KEYENCE VE-7800 scanning electron microscope (SEM). Chemical analysis of solutions and precipitates was performed by inductively coupled plasma atomic emission spectrometry (ICP-AES) on Seiko Instruments SPS4000.

The amount of H_2O evaporated from $LaPO_4$ was determined by the Karl Fischer titration method. The samples were dried in advance at 600 °C for 50 h in the air (p_{H2O} ~ 0.01 atm) to eliminate residual water and phosphoric acid on the surface of samples. The protons responsible for the proton conduction were still expected to remain in the samples, judging from the reported p_{H2O} dependence of the conductivity at 600 °C [3]. Then each sample was held at 800 °C under dry nitrogen flow (200 mL/min) to be dehydrated. The nitrogen which contains the released H_2O was transferred to the Karl Fischer moisture titrator to determine the amount of H_2O evaporated from the sample. For this, Kyoto Electronics Manufacturing MKC-510N (Karl-Fischer moisture titrator) and

ADP-512S (evaporator) were utilized.

5.2.3 Calculation of Precipitation Ratios

For better understanding of the precipitation behavior, the concentration values of La and Sr in the residual solutions were converted into “precipitation ratios”. Here, the precipitation ratio of element M, R_M, is defined by the following formula:

$$R_M \equiv \frac{n_{M,\,prec}}{n_{M,\,init}}, \tag{5.2}$$

where $n_{M,\,prec}$ and $n_{M,\,init}$ are the quantities of M in the precipitate and initial solution, respectively. For example, R_{La} will be 1 (=100 %) when all La in the initial solution precipitates as $LaPO_4$ or LaP_3O_9. For calculating R_{La} and R_{Sr} values, the following method was used. First, variables $C_{i,\,La}$, $C_{i,\,Sr}$, $C_{f,\,La}$, and $C_{f,\,Sr}$ are defined to represent the molar ratios of La, Sr, and P in the initial and residual solutions as shown in Eqs. (5.9) and (5.10):

$$La : Sr : P = C_{i,\,La} : C_{i,\,Sr} : 1 \text{ (In the initial solution)}, \tag{5.3}$$

$$La : Sr : P = C_{f,\,La} : C_{f,\,Sr} : 1 \text{ (In the residual solution after precipitation)}. \tag{5.4}$$

The values of $C_{i,\,La}$, and $C_{i,\,Sr}$ are readily obtained from the mixing ratio of the starting materials and those of $C_{f,\,La}$, and $C_{f,\,Sr}$ can be derived from the ICP analysis on the residual solution. Assuming that the molar ratio of P/(La+Sr) in the precipitates is k (k=1 for Sr-doped $LaPO_4$ and k=3 for Sr-doped LaP_3O_9), $C_{i,\,La}$, $C_{i,\,Sr}$, $C_{f,\,La}$, and $C_{f,\,Sr}$ can be correlated by Eq. (5.11) by considering the molar ratio in the residual solution:

$$C_{f,\,La} : C_{f,\,Sr} : 1 = C_{i,\,La}\,(1 - R_{La}) : C_{i,\,Sr}\,(1 - R_{Sr}) : 1 - k\,(C_{i,\,La}\,R_{La} + C_{i,\,Sr}\,R_{Sr}). \tag{5.5}$$

By solving this equation, the precipitation ratios (R_{La} and R_{Sr}) are given as follows:

$$R_{La} = -\frac{(C_{f,\,La}\,C_{i,\,Sr} - C_{f,\,Sr}\,C_{i,\,La})\;k + C_{i,\,La} - C_{f,\,La}}{(C_{f,\,Sr} + C_{f,\,La})\;C_{i,\,La}\,k - C_{i,\,La}}, \tag{5.6}$$

$$R_{Sr} = \frac{\left(C_{f,\,La}\,C_{i,\,Sr} - C_{f,\,Sr}\,C_{i,\,La}\right)\,k - \,C_{i,\,Sr} + C_{f,\,Sr}}{\left(C_{f,\,Sr} + C_{f,\,La}\right)\,C_{i,\,Sr}\,k - C_{i,\,Sr}}. \tag{5.7}$$

5.3 Results and Discussion

5.3.1 Sr-doped $LaPO_4$

5.3.1.1 Precipitation Behavior in Low Sr Concentration Solutions

First, attempts to synthesize Sr-doped $LaPO_4$ were carried out using solutions with the compositions Sr4 and Sr8. Experiments were performed in the precipitation region of $LaPO_4$ (see Figure 5.1) under both atmospheric (A120) and humidified (H250, H120) conditions. The precipitation period was varied to observe changes in the composition of precipitates and solutions with time. In each condition, single phase $LaPO_4$ was precipitated, as confirmed by X-ray diffraction.

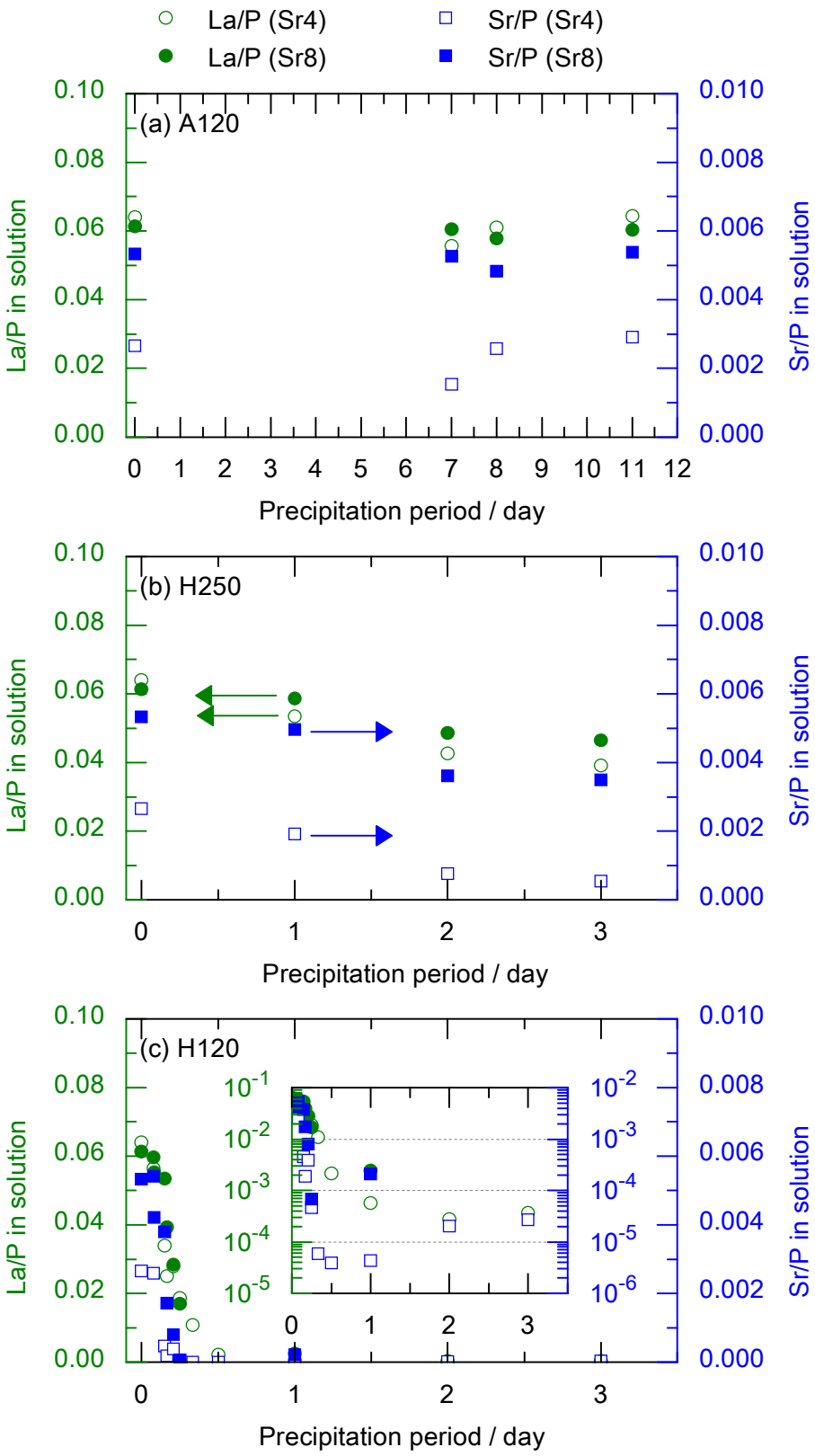

Figure 5.3 Change in composition of solutions with time under the conditions (a) A120, (b) H250, and (c) H120. Inset in (c) is a logarithmic plot.

Figure 5.3 shows the change in the composition of the solutions with time measured by ICP. The concentrations of La and Sr decreased with time. In particular, under H120 condition, the concentrations decreased rapidly by 2-3 orders. This indicates that the solubility of $LaPO_4$ in phosphoric acid solutions is especially low under H120 condition, or the driving force for the precipitation is strong under that condition. This result corresponds well to the fact that H120 condition is quite deep in the precipitation region of $LaPO_4$ in Figure 5.1. Under A120 condition, the changes in the concentrations of La and Sr fluctuated. This is likely due to the fluctuation of water vapor pressure in the atmosphere.

For better understanding of the precipitation behavior, these concentration values were converted into precipitation ratios defined by Eq. (5.8). Figure 5.4 shows the changes in R_{La} and R_{Sr}. R_{Sr} was greater than R_{La} in the early stages of the precipitation regardless of the initial composition of the solution. This suggests the formation of Sr-richer $LaPO_4$ than the initial solutions.

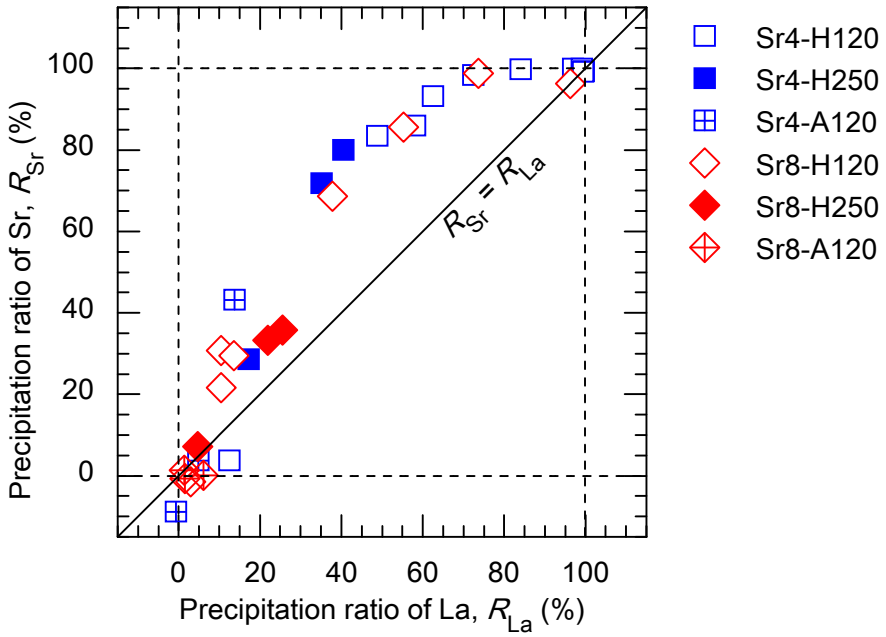

Figure 5.4 Change in the precipitation ratios of La and Sr observed along with the progression of the precipitation of $LaPO_4$.

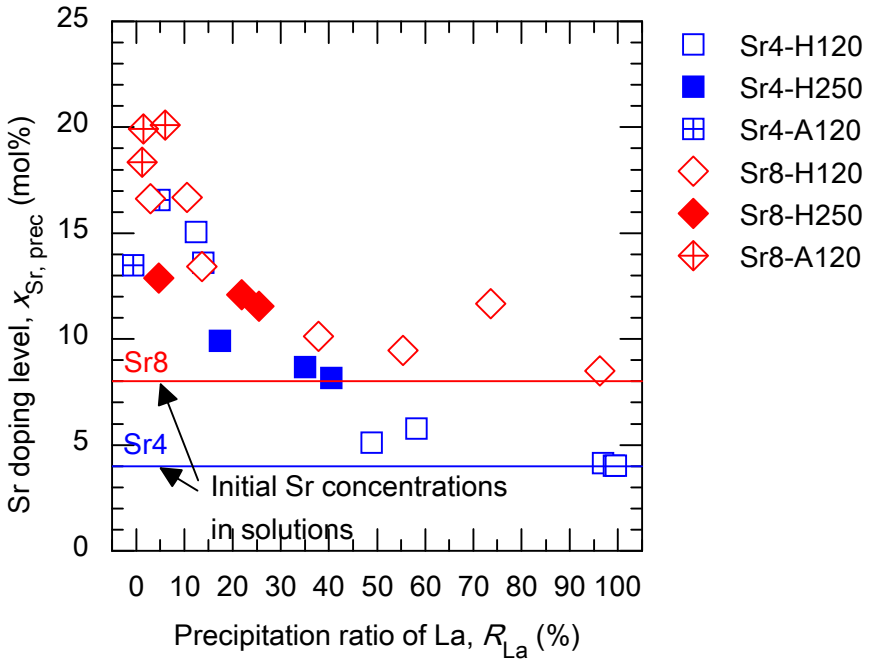

Figure 5.5 Dependence of the Sr doping level in $LaPO_4$ on the precipitation ratio of La.

Figure 5.5 shows the Sr doping levels in the $LaPO_4$ precipitates analyzed by ICP. Here, the Sr doping level, $x_{Sr,\ prec}$, represents the following molar fraction:

$$x_{Sr,\ prec} \equiv \frac{n_{Sr,\ prec}}{n_{La,\ prec} + n_{Sr,\ prec}} \times 100\ (\%). \qquad (5.8)$$

The Sr doping level showed a strong dependence on R_{La}. In good agreement with the precipitation ratio changes described above (Figure 5.4), the Sr doping levels in the precipitates were higher in the low R_{La} region, reaching 20 mol% at maximum. This value is one order of magnitude higher than the reported solubilities of Sr in $LaPO_4$ [1,4]. The precipitation temperature and p_{H2O} did not seem to have a significant effect on this trend, although they affect the attainable precipitation ratio limited by thermodynamics, and the Sr doping level accordingly.

5.3.1.2 Precipitation Behavior in High Sr Concentration Solutions

Because of the rapid decrease in the Sr doping level with progression of the precipitation, it would be difficult to obtain uniformly Sr-doped $LaPO_4$ in the above solutions. Since the Sr doping

levels shown in Figure 5.5 are average values, the actual Sr doping levels in the final precipitates (R_{La} = ~100%) are thought to be close to 0 %. The decrease in Sr doping level seems inevitable, as Sr in the solutions is nearly "exhausted" in early stages of the precipitation. A way to avoid the exhaustion of Sr in the solutions may be to increase the Sr concentration in the solutions. Therefore, the precipitation behavior of $LaPO_4$ in solutions Sr12, Sr16, Sr20, Sr40, Sr60, and Sr80 was investigated at H250 condition.

Single phase $LaPO_4$ was precipitated in all the solutions except Sr80, as confirmed by X-ray diffraction. In the Sr80 solution, $SrH_2P_2O_7$ precipitated instead of $LaPO_4$. Figure 5.6 represents the Sr doping levels in precipitates. As shown in Figure 5.6 (a), the Sr doping level in $LaPO_4$ increased with increasing the initial Sr concentration in the solutions. The dependence was not linear, however, and the increase in the doping level became moderate with higher initial Sr concentrations (Sr20, Sr40 and Sr60). The Sr doping level tended to decrease with increasing the precipitation ratio of La as observed previously. Nevertheless, the variation range relative to the doping level became smaller with higher initial Sr concentrations. As shown in Figure 5.6 (b), the Sr doping level relative to the initial Sr concentration in the solutions, ($x_{Sr,\ prec}$ / $x_{Sr,\ init}$), decreased with increasing the initial Sr concentration in the solutions. With Sr20, Sr40, and Sr60 compositions, ($x_{Sr,\ prec}$ / $x_{Sr,\ init}$) was not larger than 1. Thus, the exhaustion of Sr cannot happen with those compositions. These results indicate that uniformly and highly Sr-doped $LaPO_4$ with doping levels of ~20% can be obtained in the solutions with Sr concentrations higher than that of Sr20.

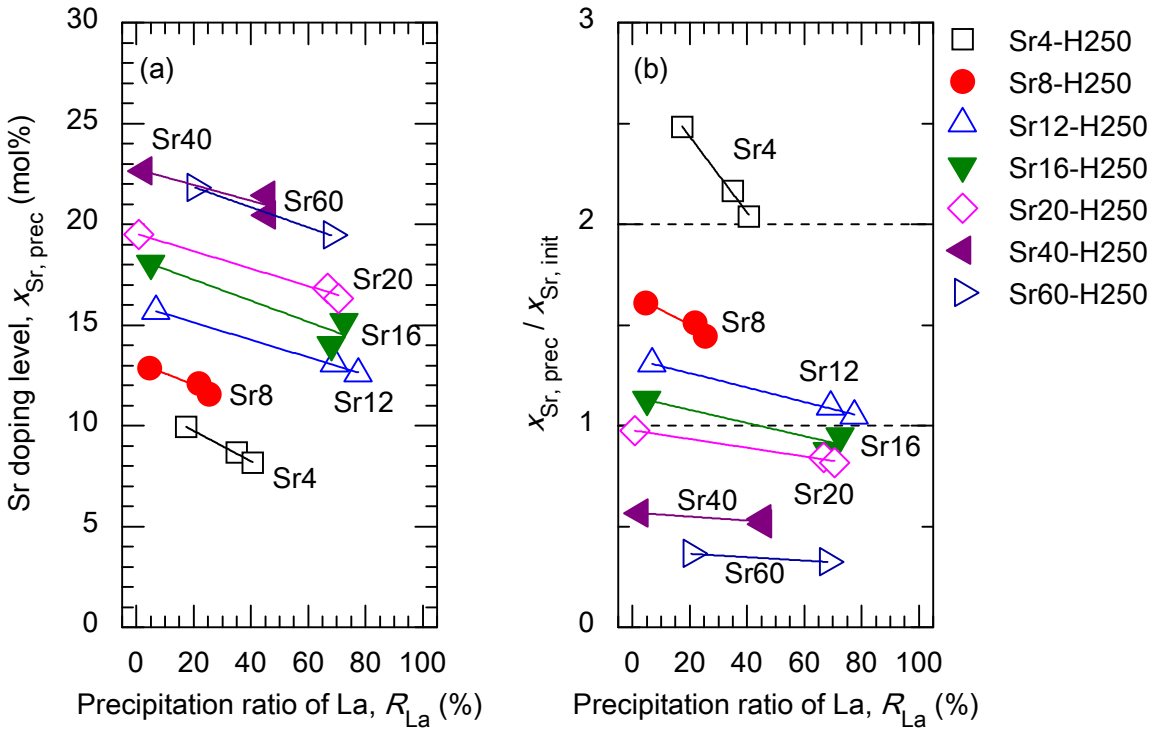

Figure 5.6 (a) Dependence of the Sr doping level in $LaPO_4$ on the precipitation ratio of La. (b) Sr doping level in $LaPO_4$ relative to the initial Sr concentration in the solutions.

5.3.1.3 Effectiveness of Sr Doping

To examine whether Sr was doped correctly and H_2O was incorporated in the bulk as desired, the following two methods were used: (1) The amount of H_2O evaporated from samples at 800 °C in dry N_2 was measured by the Karl Fischer titration method. (2) The unit cell volume of samples was evaluated before and after the H_2O evaporation measurement using powder X-ray diffraction patterns. Prior to these measurements, samples were dried at 600 °C in the air for 50 h.

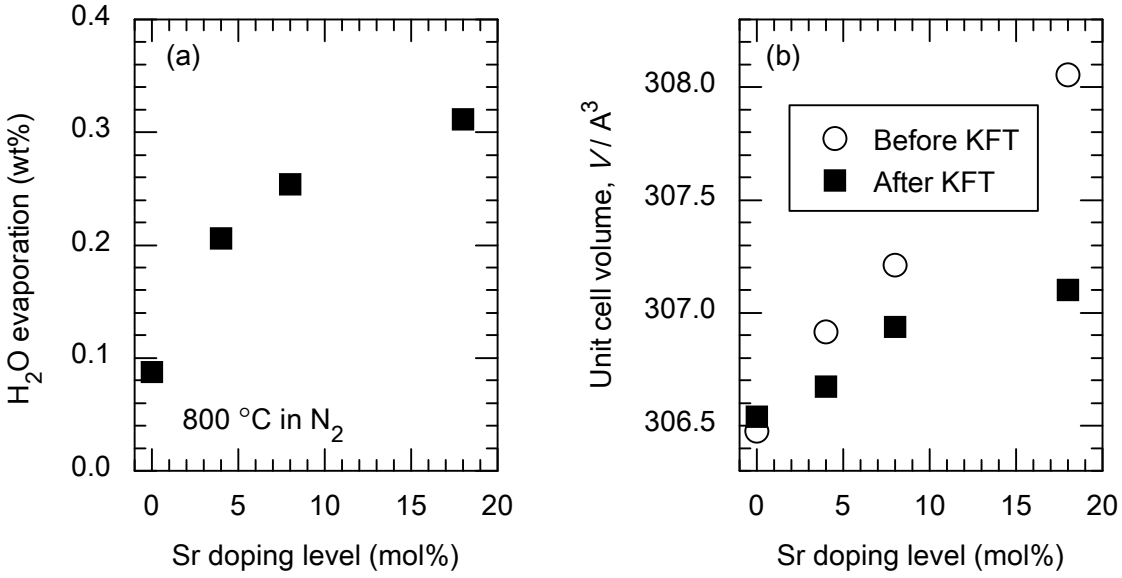

Figure 5.7 (a) H_2O evaporation from Sr-doped $LaPO_4$ under N_2 at 800 °C as measured by the Karl Fischer titration (KFT) method. The samples were held in the air at 600 °C for 50 h beforehand. (b) Unit cell volume of Sr-doped $LaPO_4$ as determined by Rietveld analysis using powder X-ray diffraction patterns. The open circles (○) represent the cell volume of samples before the titration (just after held in the air at 600 °C for 50 h). The filled squares (■) represent the cell volume of samples after the titration.

Figure 5.7 (a) represents the H_2O evaporation from $LaPO_4$ (expressed in percentage of the initial weight of each sample) with different Sr doping levels (0, 4, 8 and 18 mol%). Although the plots are not linear, H_2O evaporation monotonically increased with increasing the Sr doping level. This should indicate that H_2O was incorporated in $LaPO_4$ with Sr on the synthesis. Figure 5.7 (b) shows the unit cell volume of samples before and after the H_2O evaporation measurement. In both cases, $LaPO_4$ with higher Sr doping level had larger unit cell volume. This would indicate that Sr substituted for La in the monazite structure, since the ionic radius of Sr^{2+} in ninefold coordination (1.31 Å) is larger than that of La^{3+} (1.21 Å) [5]. After the H_2O evaporation measurement, the unit cell volume of Sr-doped $LaPO_4$ significantly decreased while that of undoped $LaPO_4$ remained unchanged. This would reflect the evaporation of H_2O from the bulk Sr-doped $LaPO_4$. In Figure 5.7 (a) the small H_2O evaporation was observed even from undoped $LaPO_4$, but it could be due to some residual water on

the surface or grain boundaries of the sample.

These results suggest that Sr successfully substituted for La and H_2O was certainly incorporated in the bulk as desired.

5.3.1.4 Thermal Stability of Highly Sr-doped $LaPO_4$

To evaluate the stability of highly Sr-doped $LaPO_4$, 13.4 % Sr-doped $LaPO_4$ and 20.1 % Sr-doped $LaPO_4$ synthesized in phosphoric acid solutions were heat treated at higher temperatures. The samples were first held at 600 °C for 80 h in the atmosphere, then the 13.4% doped sample was additionally held at 1200 °C for 5 h. Figure 5.8 shows the X-ray diffraction patterns obtained after each heat treatment. While no secondary phase was detected after the first heat treatment at 600 °C, the presence of secondary phases, $Sr_2P_2O_7$ and $Sr_3La(PO_4)_3$, was clearly detected after the second heat treatment at 1200 °C. Amezawa *et al*. reported $Sr_2P_2O_7$ as the secondary phase at 1200 °C and $Sr_3La(PO_4)_3$ at above 1350 °C [3]. Tyholdt *et al*. also reported both as the secondary phases at 1450 °C [4]. The fact that both $Sr_2P_2O_7$ and $Sr_3La(PO_4)_3$ were detected in the present study is somewhat incompatible with the previous study by Amezawa, but it could be due to some kinetic reason. The present results indicate that the solubility of Sr in $LaPO_4$ would be sufficiently high (at least 20.1 %) at 600 °C, which is in the operating temperature range for the electrolyte. However, the solubility of Sr is considerably lower than 13.4 % at 1200 °C, which is a typical sintering temperature for this material. Therefore, a new synthesis process of $LaPO_4$ electrolytes based on precipitation in homogeneous phosphoric acid solutions, which enables synthesizing dense $LaPO_4$ electrolytes without sintering, should have a considerable advantage. The reason why the solubility of Sr is higher at lower temperatures has not been clarified, but it is possible to speculate that Sr in the $LaPO_4$ lattice is destabilized with evaporation of water at high temperatures. In other words, the reverse reaction of Eq. (5.1) can proceed at higher temperatures.

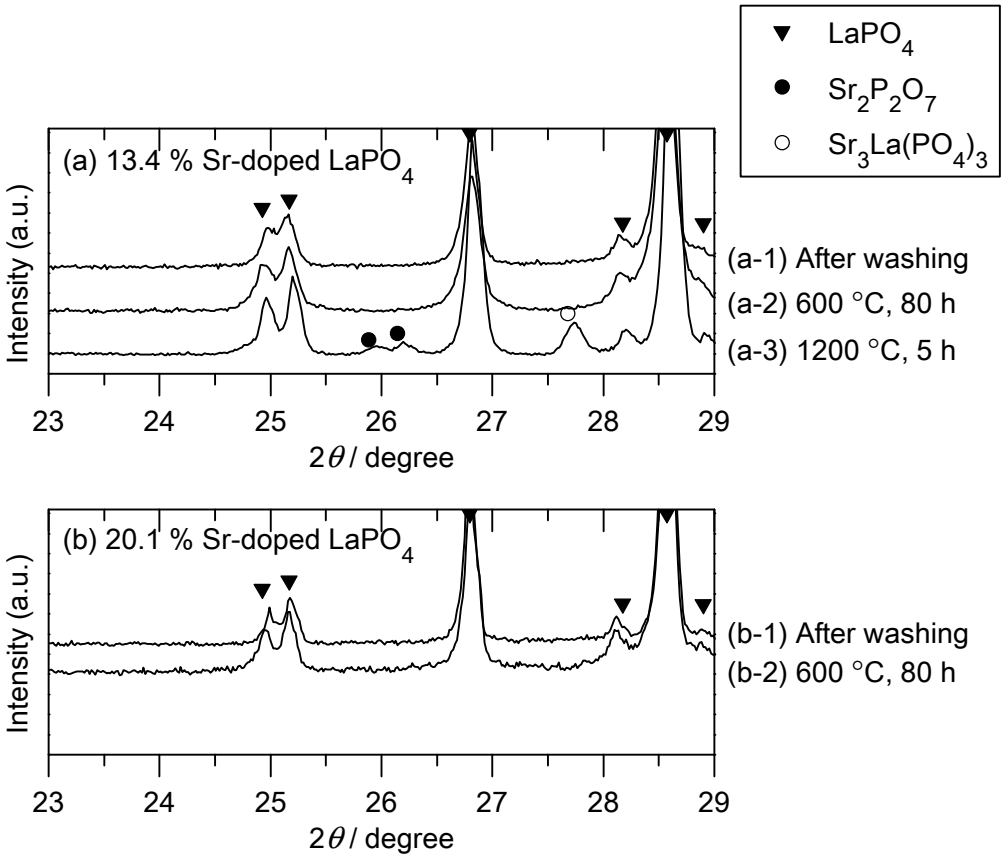

Figure 5.8 X-ray diffraction patterns of (a) 13.4% Sr-doped $LaPO_4$ and (b) 20.1% Sr-doped $LaPO_4$. They were collected (a-1)(b-1) just after washing, (a-2)(b-2) after the first heat treatment at 600 °C for 80 h and (a-3) after the second heat treatment at 1200 °C for 5 h. Peaks marked with ▼, ●, and ○ are attributed to $LaPO_4$ (PDF# 1-83-651), $Sr_2P_2O_7$ (PDF#0-24-1011), and $Sr_3La(PO_4)_3$ (PDF# 0-29-1306), respectively.

5.3.2 Sr-doped LaP_3O_9

The precipitation behavior of LaP_3O_9 in phosphoric acid solutions was also investigated at A230 condition. Single phase LaP_3O_9 was obtained in the solutions Sr4, Sr8, Sr12, Sr16, Sr20, Sr30, Sr40, and Sr50 whereas $Sr(PO_3)_2$ formed in the solutions Sr60 and Sr80. Figure 5.9 represents the Sr doping levels in precipitates. As shown in Figure 5.9 (a), the Sr doping level in LaP_3O_9 increased with increasing the initial Sr concentration in the solutions, reaching 14 mol% at maximum. This value is approximately three times higher than the previously attained value [2]. Similar to the case

of $LaPO_4$, the Sr doping level tended to decrease with increasing the precipitation ratio of La. However, as shown in Figure 5.6 (b), the Sr doping level relative to the initial Sr concentration in the solutions, ($x_{Sr,\ prec}$ / $x_{Sr,\ init}$), was always less than 1. Thus, in contrast to the case of $LaPO_4$, the exhaustion of Sr is not thought to happen. The reason for the decrease in the Sr doping level is currently unknown, but the problem might be less serious than that with $LaPO_4$. In the same time, as is the case for $LaPO_4$, uniformly and highly Sr-doped LaP_3O_9 can be easily obtained in the solutions with higher Sr concentrations.

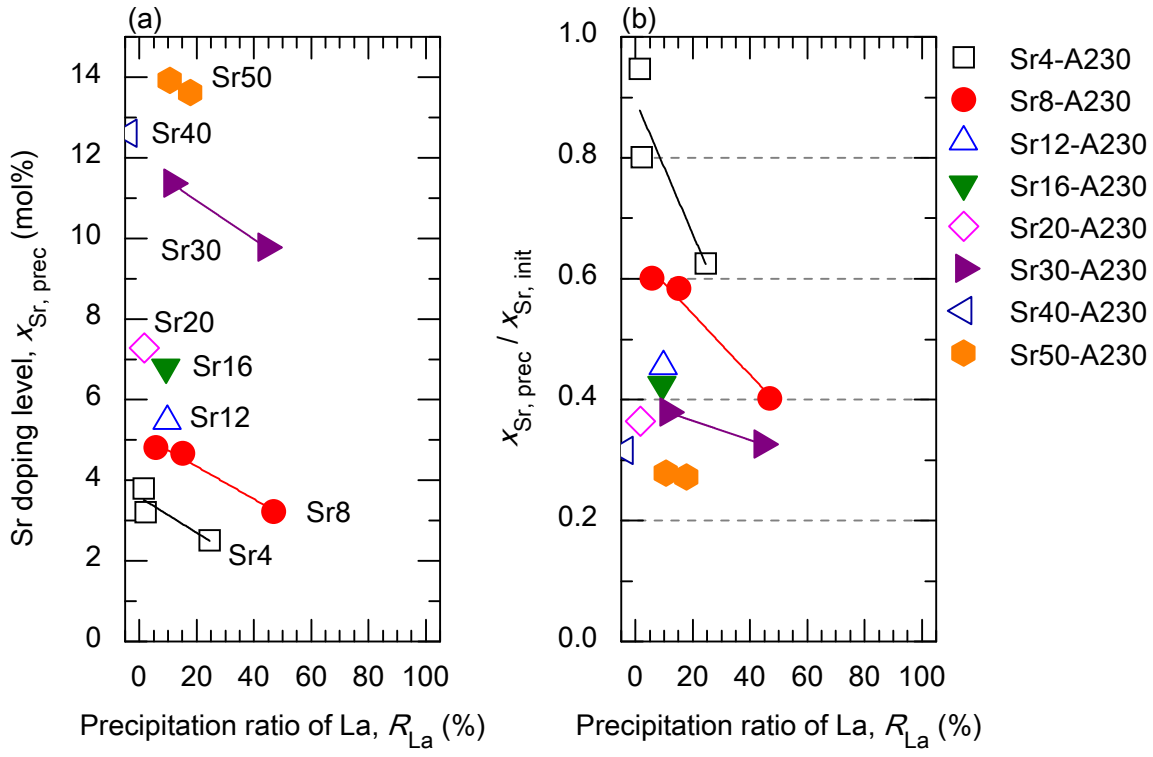

Figure 5.9 (a) Dependence of the Sr doping level in LaP_3O_9 on the precipitation ratio of La. (b) Sr doping level in LaP_3O_9 relative to the initial Sr concentration in the solutions.

In order to see whether Sr was successfully incorporated in the LaP_3O_9 lattice, unit cell volume changes were determined by Rietveld analysis using powder X-ray diffraction data. As shown in Figure 5.10, LaP_3O_9 with higher Sr doping level had larger unit cell volume. This would indicate that Sr substituted for La in the LaP_3O_9 lattice, since the ionic radius of Sr^{2+} in eightfold coordination

(1.26 Å) is larger than that of La^{3+} (1.16 Å) [5].

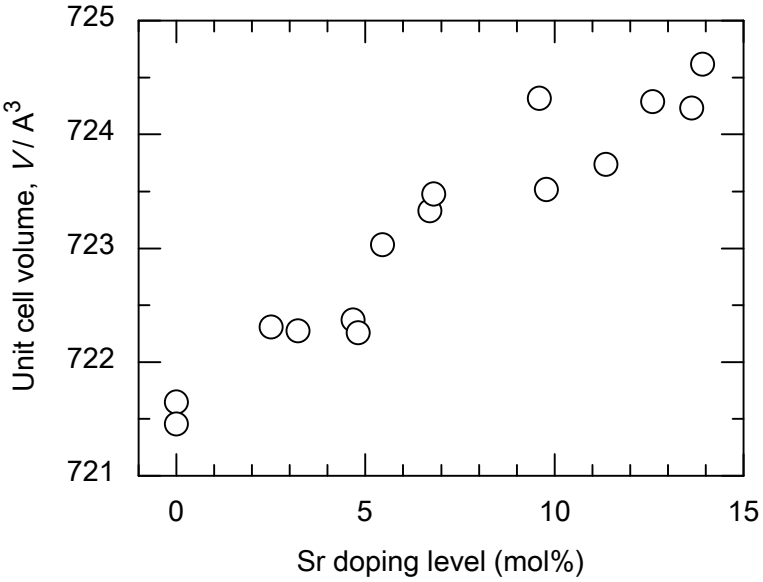

Figure 5.10 Unit cell volume of Sr-doped LaP_3O_9 as determined by Rietveld analysis using powder X-ray diffraction patterns.

5.4 Conclusions

In this chapter, attempts were made to synthesize Sr-doped $LaPO_4$ and LaP_3O_9 in phosphoric acid solutions. The condition dependence of the Sr doping level was analyzed to reveal the optimum condition for obtaining highly Sr-doped phosphates.

The Sr doping level in $LaPO_4$ and LaP_3O_9 depended on the precipitation ratio of La, R_{La}. The Sr doping level gradually decreased with the progression of the precipitation, which was especially noticeable for low Sr concentration solutions. In the case of $LaPO_4$, Sr in the solutions was thought to be exhausted in early stages of the precipitation. However, with high Sr concentrations in the solutions, such as $\left(\frac{Sr}{La+Sr}\right) \geq 20$ mol%, the change in the Sr doping level was relatively small. In such solutions, almost uniformly Sr doped samples are expected to be obtained. The maximum Sr doping levels attained for $LaPO_4$ and LaP_3O_9 were ~23 % and ~14 %, respectively. These values are

several times higher than previously reported solubilities of Sr in $LaPO_4$ and LaP_3O_9.

The incorporation of Sr and H_2O in the $LaPO_4$ lattice was verified by unit cell volume change and evaporation of H_2O. Sr partially substituted for La in monazite-type $LaPO_4$ when synthesized in phosphoric acid solutions, as well as by solid state reaction as reported in the literature. On synthesis, H_2O was certainly incorporated in the bulk by Sr doping. The incorporation of Sr in the LaP_3O_9 lattice was also verified by unit cell volume change.

The stability of Sr-doped $LaPO_4$ at high temperatures was also investigated. The solubility of Sr in $LaPO_4$ was found to be sufficiently high (at least 20.1 %) even at 600 °C, which is in the operating temperature range for the electrolyte. However, it becomes considerably lower than 13.4 % at 1200 °C. The reason why the solubility of Sr is higher at lower temperatures has not been clarified, but it is possible to speculate that Sr in the $LaPO_4$ lattice is destabilized with evaporation of water at high temperatures.

References

[1] K. Amezawa, Y. Tomii, N. Yamamoto, Solid State Ionics 176 (2005) 143-148.

[2] K. Amezawa, Y. Uchimoto, Y. Tomii, Solid State Ionics 177 (2006) 2407-2411.

[3] K. Amezawa, H. Maekawa, Y. Tomii, N. Yamamoto, Solid State Ionics 145 (2001) 233-240.

[4] F. Tyholdt, J.A. Horst, S. Jørgensen, T. Østvold, T. Norby, Surf. Interface Anal. 30 (2000) 95-97.

[5] R.D. Shannon, Acta Cryst. A32 (1976) 751-767.

Chapter 6
Electrical Conduction Properties of Sr-doped $LaPO_4$ and LaP_3O_9

6.1 Introduction

As mentioned in Chapter 1, the proton conductivity enhancement in lanthanum phosphates is desirable, while the proton conduction mechanisms are still unclear. In previous chapters, the precipitation conditions have been established for synthesizing highly Sr-doped $LaPO_4$ and LaP_3O_9 with various grain sizes. These techniques should broaden the way to investigate the proton conduction mechanisms, as well as to improve the electrolyte performances. Nevertheless, if they are heat treated at typical sintering temperatures to obtain dense electrolytes, they will decompose or Sr doping level will decrease (see previous chapters). Therefore, the direct synthesis of dense electrolytes at low temperatures is necessary for investigating their electrical conduction properties.

In this chapter, attempts were made to obtain dense, polycrystalline plates of Sr-doped $LaPO_4$ and LaP_3O_9 in phosphoric acid solutions by gradually providing the driving force for the precipitation. The synthesis of large single crystals of Sr-doped LaP_3O_9 was also tried with a similar strategy. Then the electrical conduction properties of the precipitates were investigated by impedance spectroscopy.

6.2 Experimental

6.2.1 Synthesis

Sr-doped $LaPO_4$ and LaP_3O_9 were synthesized in phosphoric acid solutions based on the method

given in the previous chapter. La_2O_3 (99.99%, Nacalai Tesque), $SrCO_3$ (99.99%, Wako Pure Chemical Industries), and H_3PO_4 (85%, Nacalai Tesque) were mixed in glassy carbon crucibles and heated at 190 °C for several days to dissolve all solid compounds in phosphoric acid. Then the solutions were gradually cooled or heated in ambient (p_{H2O} = ~0.01 atm) or humidified (p_{H2O} = ~1 atm) atmospheres to precipitate lanthanum phosphates. The synthesis parameters are given in Table 6.1. These parameters were chosen based on the solubility of lanthanum oxide in phosphoric acid solutions at each temperature. The following requirements were considered: (1) No precipitate should be formed at the initial temperature in the precipitation stage; (2) The desired precipitate should be formed at the final temperature. As a result, a moderate driving force for the precipitation should begin to be provided at a certain point during the cooling or heating process. After the temperature had reached the final temperature, the solutions were held isothermally for several days. For humidification, the apparatus used in Chapter 2 was used.

Table 6.1 Synthesis parameters for Sr-doped $LaPO_4$ and LaP_3O_9 electrolytes. p_{H2O} is water vapor pressure, $T_{initial}$ and T_{final} denote temperatures at which slow cooling/heating started and ended, respectively, β is the heating rate, and $t_{isothermal}$ is the duration of the isothermal heating.

	Product	Initial composition	Precipitation parameters				
		La : Sr : P	p_{H2O} / atm	$T_{initial}$ / °C	T_{final} / °C	β / °C h^{-1}	$t_{isothermal}$ / day
(a)	Sr-doped $LaPO_4$ polycrystalline plates	0.48 : 0.12 : 15	~1	250	200	−1	1
(b)	Sr-doped LaP_3O_9 polycrystalline plates	0.80 : 0.20 : 15	~0.01	190	250	1	8
(c)	Sr-doped LaP_3O_9 single crystals	0.40 : 0.10 : 15	~1	300	360	0.5	4

6.2.2 Characterization

Phase identification was carried out *via* X-ray diffraction (XRD) analysis on PANalytical X'Pert-Pro MPD using Cu-Kα radiation at room temperature. The morphology and composition of

precipitates were investigated using KEYENCE VE-7800 scanning electron microscope (SEM) equipped with energy dispersive X-ray spectrometer (EDS, EDAX Genesis-XM2). Chemical analysis was also performed by inductively coupled plasma atomic emission spectrometry (ICP-AES) on Seiko Instruments SPS4000. It has been found that, in general, the difference between the values for the Sr doping level of the same sample derived from EDS and ICP analyses are within 3%.

6.2.3 AC Impedance Spectroscopy

For measuring the electrical conductivity of the polycrystalline plates, silver paste (Fujikura Kasei, D-550) was painted on each surface of the precipitates. A silver wire and a silver mesh were attached to each surface using the silver paste. Then the sample was fixed to the sample holder shown in Figure 6.1 (a). For measuring the electrical conductivity of the single crystals, platinum wires were attached to parallel surfaces using the silver paste. Then the sample was fixed to the sample holder shown in Figure 6.1 (b).

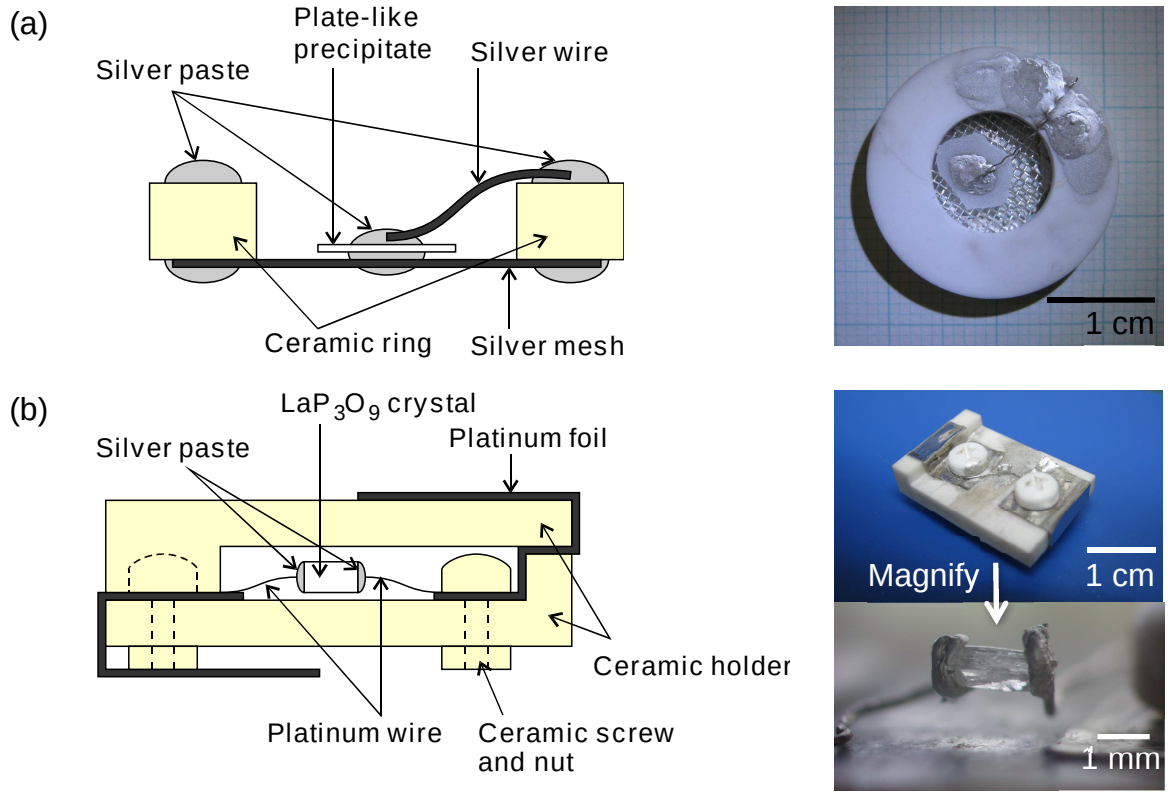

Figure 6.1 Schematic illustrations and typical photographs of the sample holders for conductivity measurements. (a) For polycrystalline plates; (b) For single crystals.

The conductivity of the samples was measured by impedance spectroscopy. A.C. impedance data were collected over the frequency range of 10 Hz–10 MHz using a frequency response analyzer (Solartron SI 1260) at an applied voltage of typically 100 mV. Humidified hydrogen, argon or their mixture was flowed over the samples at typically 20 sccm. The fitting of the impedance data was performed using the commercial software package, ZView Version 2.9c (Scribner Associates).

6.3 Results and Discussion

6.3.1 Direct Synthesis of Electrolytes in Phosphoric Acid Solutions

6.3.1.1 Sr-doped $LaPO_4$ Polycrystalline Plates

Figure 6.2 shows a typical photograph and SEM image of Sr-doped $LaPO_4$ precipitated on the bottom surface of the crucible with the synthesis parameters given in Table 6.1 (a). The precipitate

formed a plate which can be handled with tweezers or by hand. The thickness of the plate was about 150 μm. As can be seen in the cross-sectional image of the plate (Figure 6.2 (b)), the plate mainly consisted of densely packed, elongated grains of ~100 μm arranged in the direction perpendicular to the surfaces. In addition, a closer look at the lower part of the plate, which was in contact with the crucible, reveals the existence of a thin layer consisted of relatively small grains. The overall geometry of the cross-section resembles the general microstructure of ingots, with the lower part and upper part of the plate corresponding to the chill zone and columnar zone in an ingot, respectively. This suggests that heterogeneous nucleation took place on the bottom surface of the crucible and then large columnar grains were formed upward as a result of competitive growth.

Figure 6.3 shows the X-ray diffraction patterns obtained from each surface of the Sr-doped $LaPO_4$ plate. The relative intensities of the peaks were significantly different from those expected from randomly oriented powders, indicating the existence of preferred orientations of the grains. While the $(\bar{1}\,11)$ planes were oriented parallel to the surfaces in the lower part, the (100) planes were oriented parallel to the surfaces in the upper part. Therefore, the perpendicular direction to the (100) planes is considered to be the preferred growth direction for $LaPO_4$ crystals.

By EDS analysis, the Sr doping level was found to be 13% at the lower surface and 18% at the upper surface. These results show that, dense, highly-oriented and coarse-grained polycrystalline plates of highly Sr-doped $LaPO_4$ can be directly synthesized in phosphoric acid solutions, which cannot be obtained by conventional solid state reaction.

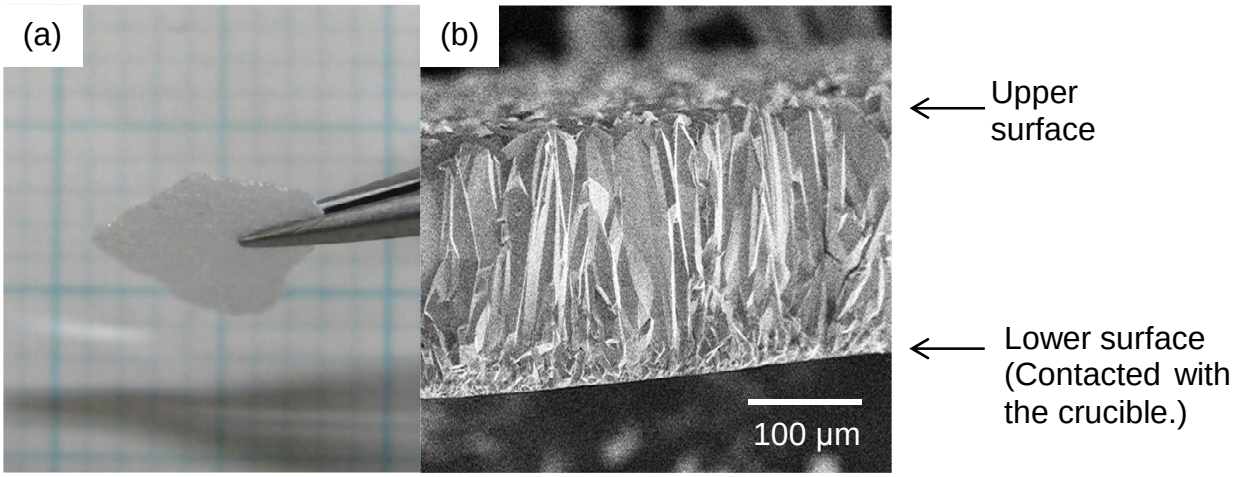

Figure 6.2 Typical (a) photograph and (b) SEM image of the polycrystalline plate of Sr-doped $LaPO_4$.

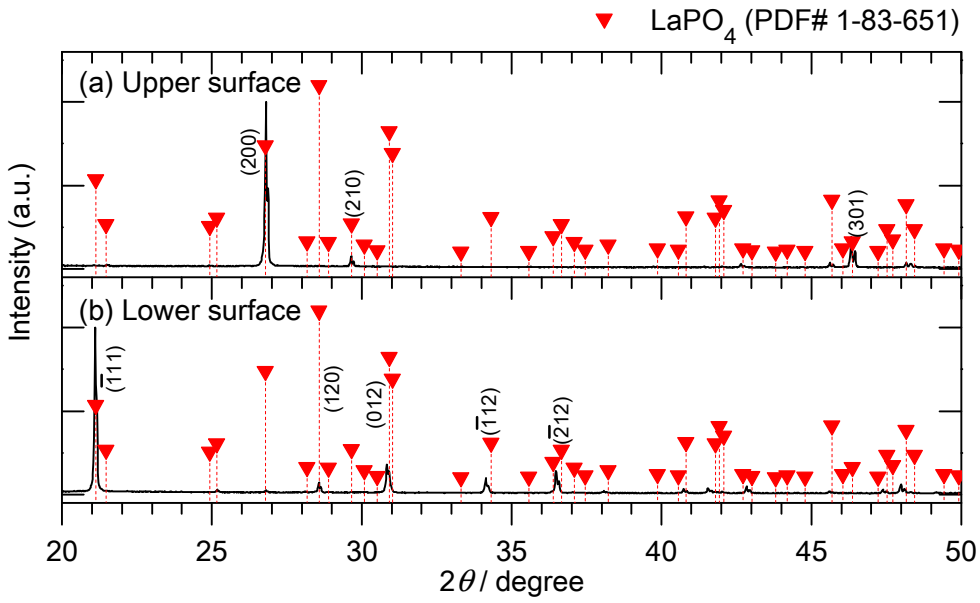

Figure 6.3 X-ray diffraction patterns of a polycrystalline plate of Sr-doped $LaPO_4$: (a) upper surface of the plate; (b) lower surface of the plate. The numbers in parentheses represent the Miller indices of peaks.

6.3.1.2 Sr-doped LaP_3O_9 Polycrystalline Plates

Figure 6.4 shows a typical photograph and SEM image of Sr-doped LaP_3O_9 precipitated on the bottom surface of the crucible with the synthesis parameters given in Table 6.1 (b). Similarly to the

case of Sr-doped $LaPO_4$, the Sr-doped LaP_3O_9 precipitate formed a plate with thickness of about 250 μm and it had the chill zone and columnar zone. (As the plate was precipitated by heating, "chill zone" might not be appropriate.) Figure 6.5 shows the X-ray diffraction patterns obtained from each surface of the Sr-doped LaP_3O_9 plate. While the (110) planes tended to be oriented parallel to the surfaces in the lower part, the (001) planes were strongly oriented parallel to the surfaces in the upper part. Therefore, the perpendicular direction to the (001) planes is considered to be the preferred growth direction for LaP_3O_9 crystals. As LaP_3O_9 has an orthorhombic crystal structure, the preferred growth direction is identical to the c-axis. By EDS analysis, the Sr doping level was found to be 11% at the lower surface and 5% at the upper surface. In summary, as is the case for Sr-doped $LaPO_4$, dense, highly-oriented and coarse-grained polycrystalline plates of highly Sr-doped LaP_3O_9 can also be directly synthesized in phosphoric acid solutions.

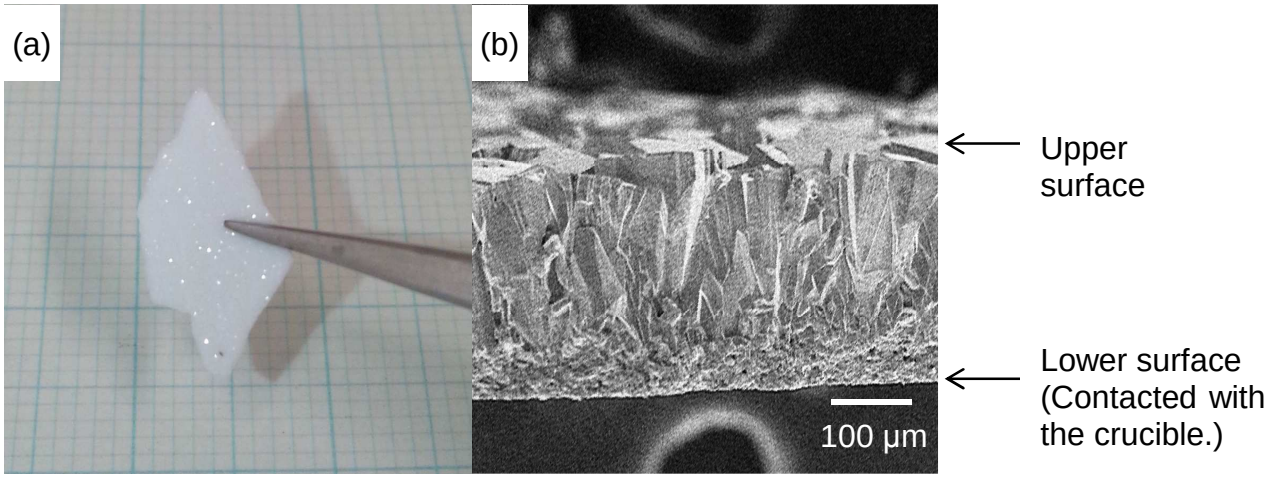

Figure 6.4 Typical (a) photograph and (b) SEM image of the polycrystalline plate of Sr-doped LaP_3O_9.

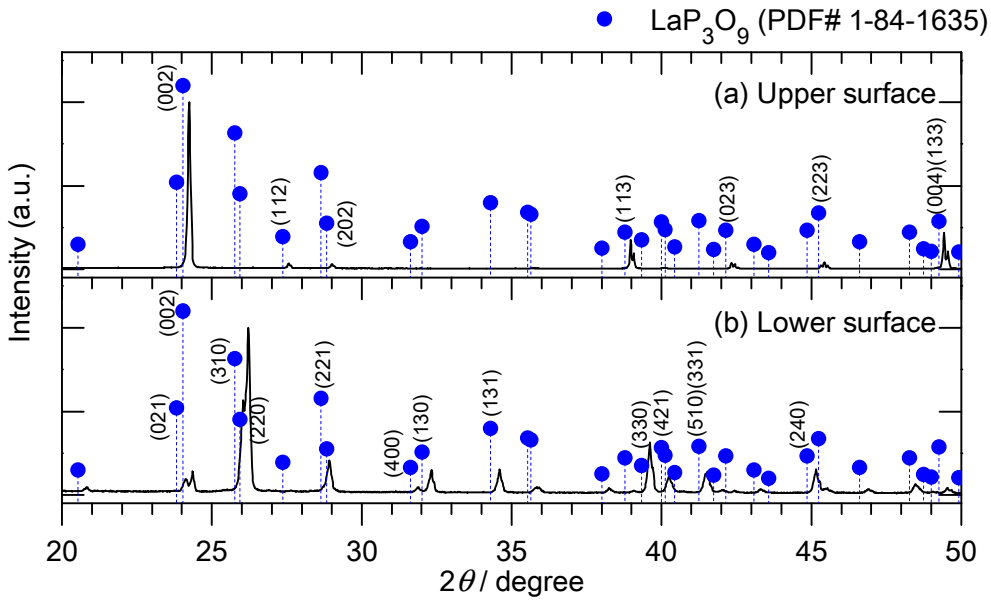

Figure 6.5 X-ray diffraction patterns of a polycrystalline plate of Sr-doped LaP_3O_9: (a) upper surface of the plate; (b) lower surface of the plate. The numbers in parentheses represent the Miller indices of peaks.

6.3.1.3 Sr-doped LaP_3O_9 Single Crystals

Figure 6.6 shows a typical photograph and SEM image of Sr-doped LaP_3O_9 precipitated at the bottom of the crucible with the synthesis parameters given in Table 6.1 (c). Transparent, column crystals with well-developed morphology were obtained. The crystals were nearly 2 mm in length, sufficiently large for conductivity measurements. This result confirms that the "high-humidity and high-temperature" condition established in Chapter 2 facilitates the growth of LaP_3O_9 crystals. By X-ray diffraction, it was found that the c-axis of the LaP_3O_9 lattice was always directed parallel to the longer direction of the crystals (Figure 6.7). This is consistent with the preferred growth direction of LaP_3O_9 suggested in the previous subsection (c-axis). As LaP_3O_9 has an orthorhombic crystal structure, the ab plane is perpendicular to the c-axis, but it was difficult to distinguish crystallographic directions in the ab plane by crystal morphology. By ICP analysis, the Sr doping level was found to be 5.1%, sufficient for generating protonic charge carriers.

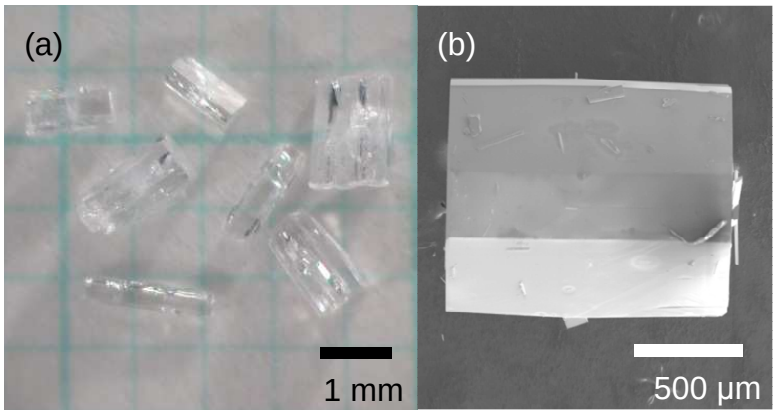

Figure 6.6 (a) Photograph and (b) SEM image of Sr-doped LaP_3O_9 single crystals.

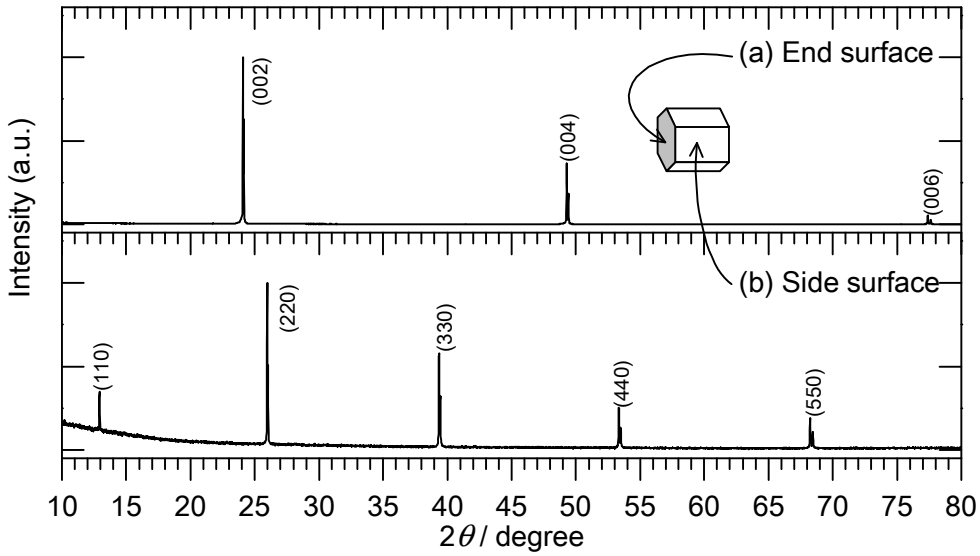

Figure 6.7 X-ray diffraction patterns of a column crystal of Sr-doped LaP_3O_9: (a) obtained from the end surface of the column crystal; (b) obtained from the side surface of the column crystal. The numbers in parentheses represent the Miller indices of peaks.

6.3.2 Electrical Conduction Properties

6.3.2.1 Sr-doped $LaPO_4$ Polycrystalline Plates

Figure 6.8 shows the impedance data of a Sr-doped $LaPO_4$ plate collected at 500 °C under various atmospheres with different hydrogen partial pressures p_{H2} and water vapor pressures p_{H2O}. Two impedance arcs were observed in the impedance spectra shown in Figure 6.8 (a). The

impedance spectra were analyzed using an equivalent circuit model $(R_1Q_1)(R_2Q_2)$ where R is a resistor and Q is a constant phase element. The resistances corresponding to high- and low-frequency arcs, R_1 and R_2, showed different dependences on hydrogen and water partial pressures. Figure 6.8 (b) shows the deviation in R_1 and R_2 on changing the atmosphere. While R_1 was independent of hydrogen partial pressure, R_2 increased with decreasing hydrogen partial pressure (atmospheres (1)–(3) in the figure).

In the present atmospheres, the forward and reverse reactions of the following equation are mainly expected to take place at both electrodes:

$$2H^+ + 2e = H_2\ (g) \tag{6.1}$$

where H^+ represents a proton in the electrolyte. Generally, at low overpotentials, the charge transfer resistance R_{ct} is inversely proportional to the exchange current density i_0 as follows:

$$R_{ct} = \frac{RT}{nFi_0} \tag{6.2}$$

where R, T, n, and F are the gas constant, absolute temperature, number of electrons in the reaction, and Faraday's constant, respectively. The exchange current density depends on the concentrations of reactants. For the reaction of Eq. (6.1), the dependence is given as

$$i_0 \propto c_{H+}^{1-\alpha} \cdot p_{H2}^{\alpha}\ (0 < \alpha < 1) \tag{6.3}$$

where c_{H+}, p_{H2}, and α are the concentration of protons in the electrolyte, hydrogen partial pressure, and charge transfer coefficient, respectively. Combining Eqs. (6.2) and (6.3) yields

$$R_{ct} \propto \frac{1}{c_{H+}^{1-\alpha} \cdot p_{H2}^{\alpha}}. \tag{6.4}$$

Therefore, if c_{H+} is constant, changing hydrogen partial pressure from $p_{H2,i}$ to $p_{H2,f}$ should result in the charge transfer resistance change from $R_{ct,i}$ to $R_{ct,f}$ according to the following relationship:

$$\frac{R_{ct,f}}{R_{ct,i}} = \left(\frac{p_{H2,i}}{p_{H2,f}}\right)^{\alpha}. \tag{6.5}$$

In the present measurements, the value of R_2 increased from 21.7 kΩ to 30.1 kΩ with decreasing hydrogen partial pressure from 0.9 atm to 0.45 atm. This behavior fits well to Eq. (6.5) with an α value of ~0.47. Therefore, R_2 would surely correspond to the charge transfer resistance R_{ct}. Accordingly, R_1 would be attributed to the electrolyte. As mentioned above, R_1 did not depend on hydrogen partial pressure. Kitamura *et al*. reported that the conductivity of Sr-doped $LaPO_4$ was almost independent of hydrogen partial pressure [1]. Hence it is reasonable to assume R_1 as the resistance of the Sr-doped $LaPO_4$ plate. For further analysis, the conductivity of the Sr-doped $LaPO_4$ plate, σ, was calculated from R_1.

When p_{H2} and p_{H2O} were varied simultaneously, from atmosphere (3) to (4) in Figure 6.8, both R_1 and R_2 changed. As it was found that R_1 did not depend on p_{H2}, the decrease in R_1 can be attributed to the increase in p_{H2O}. It suggests that the charge carrier concentration in the electrolyte increased with increasing p_{H2O}, and it is consistent with the idea that the protons are introduced into Sr-doped $LaPO_4$ through the equilibrium with water vapor [2] (See Chapter 1). As shown in Figure 6.9, the conductivity of the Sr-doped $LaPO_4$ plate exhibited a similar dependence on water vapor pressure to those reported for 2% or 3% Sr-doped $LaPO_4$ [3]. The slope of the $\log \sigma - \log p_{H2O}$ plot was 0.09, much smaller than 1/2. As discussed by Amezawa *et al*. [3], it implies that the sample was mostly hydrated in the present atmospheres.

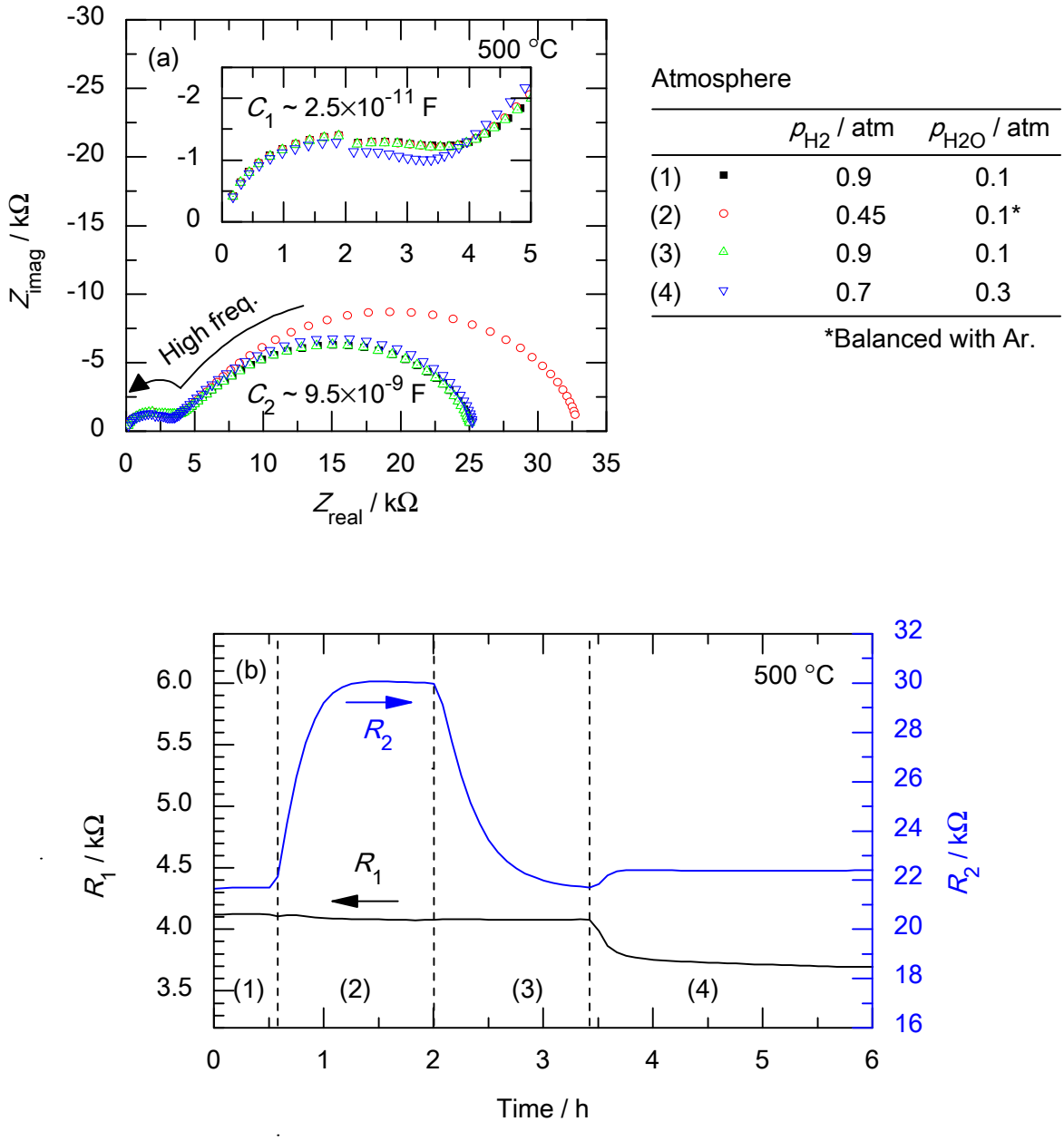

Figure 6.8 (a) Impedance spectra of a polycrystalline plate of Sr-doped $LaPO_4$ at 500 °C under various atmospheres ((1)-(4)). Inset is an enlarged view of the high-frequency arc. (b) Time dependence of the resistance of Sr-doped $LaPO_4$ at 500 °C under various atmospheres. R_1 and R_2 represent the resistances corresponding to the high- and low-frequency arcs in the impedance spectra, respectively.

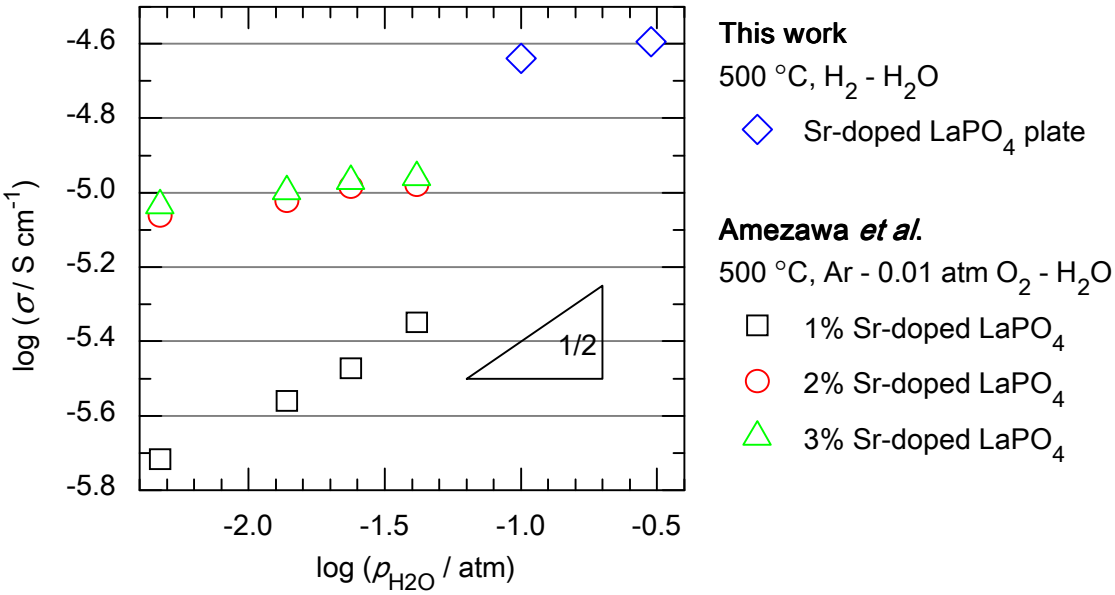

Figure 6.9 Water vapor pressure dependence of the conductivity of the polycrystalline plate of Sr-doped $LaPO_4$. Data given by Amezawa *et al.* are also shown for comparison [3].

Assuming a linear relationship between the conductivity derived from R_1 and the proton concentration in the electrolyte, a proton concentration increase of 1.11 times is expected with increasing p_{H2O} from 0.1 atm to 0.3 atm (Figure 6.8 and Figure 6.9). It is also possible to estimate the proton concentration change by the charge transfer resistance. From Eq. (6.4), the following relationship is derived for the variation in charge transfer resistance caused by the concentration changes:

$$\frac{R_{ct,f}}{R_{ct,i}} = \left(\frac{c_{H+,i}}{c_{H+,f}}\right)^{1-\alpha} \left(\frac{p_{H2,i}}{p_{H2,f}}\right)^{\alpha} \tag{6.6}$$

where the suffixes “i” and “f” represent “before” and “after” the concentration changes. Using $R_{ct,f} / R_{ct,i}$ = 22.4/21.7, $p_{H2,i} / p_{H2,f}$ = 0.9/0.7, and the α value of 0.47 derived above, the proton concentration change is given as

$$\frac{c_{H+,f}}{c_{H+,i}} = 1.18. \tag{6.7}$$

This is in a fair agreement with the value of 1.11 derived from the conductivity of the electrolyte,

indicating the current interpretation is valid. Thus, the proton conduction was confirmed in the Sr-doped $LaPO_4$ plate which was directly synthesized in a phosphoric acid solution.

Figure 6.10 shows the temperature dependence of the conductivities of Sr-doped $LaPO_4$ plates. Besides the above used plate ("Plate A"), two additional plates ("Plate B" and "Plate C") were used for the conductivity measurements. All the plates were obtained in the same solution. The conductivities of the three samples were of the same order of magnitude as those reported in the literature [3], and showed similar temperature dependences. The activation energies for charge transport, derived from the slopes of the plots, were 0.80 ± 0.05 eV at 400–500 °C while Amezawa *et al.* reported a value of 0.86 eV for 2% Sr-doped $LaPO_4$ at 500–600 °C [3].

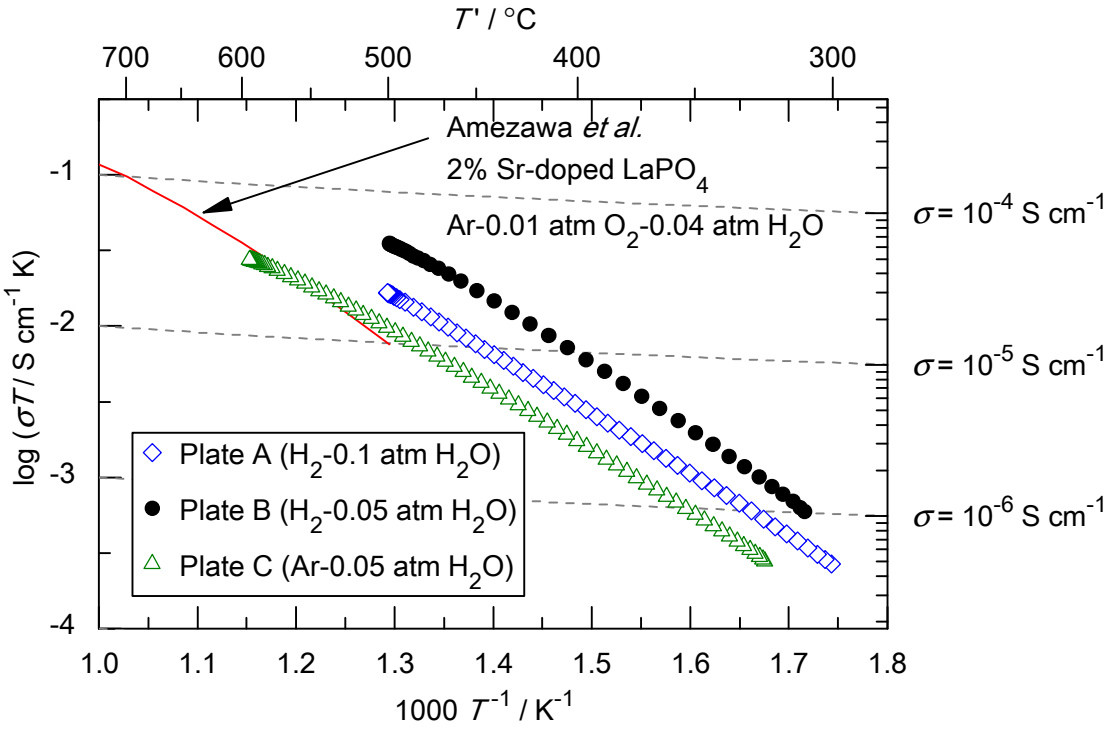

Figure 6.10 Temperature dependence of the conductivity of Sr-doped $LaPO_4$ plates. "Plate A", "Plate B", and "Plate C" are different samples obtained from the same crucible.

However, as obvious from the figure, the three samples exhibited different absolute values for the conductivity although they should be equal. The conductivities of each sample shown in Figure

6.10 were essentially reproducible through repeated heating/cooling cycles, but there was even a case where the conductivity changed through heating/cooling cycles (Not shown on the figure). The reason for the conductivity differences might be, for example, inadequate contact between the electrolyte and electrodes, or breakage of the electrolyte due to its insufficient mechanical strength, but the exact reason is not clear at present. Although the atmospheres were slightly different in which each measurement was done, it would not result in the severalfold differences of the conductivities. For further studies of the effect of Sr doping level, grain size, and crystallographic orientation on the conduction properties, it is required to establish the experimental conditions where reproducible results can be obtained.

6.3.2.2 Sr-doped LaP_3O_9 Polycrystalline Plates

Figure 6.11 shows the impedance data of a Sr-doped LaP_3O_9 plate collected at 500 °C with different hydrogen partial pressures. Two partly overlapping arcs were identified in the impedance spectra shown in Figure 6.11 (a). Fitting to the impedance spectra was carried out using an equivalent circuit model $(R_1)(R_2Q_2)$ at low frequencies (100–1000 Hz) where the low frequency arc was dominant. The high frequency intercept of the fit arc with the real axis, R_1, was regarded as the resistance corresponding to the high frequency arc. The resistances corresponding to the high- and low-frequency arcs, R_1 and R_2, showed analogous dependences on hydrogen partial pressure to those observed for Sr-doped $LaPO_4$ plates: While R_1 remained constant, R_2 increased with decreasing hydrogen partial pressure. The variation in R_2 fits well to Eq. (6.5) with an α value of ~0.39. For these reasons, R_1 and R_2 can be assigned to the electrolyte resistance and charge transfer resistance, respectively. However, because of the overlap of two impedance arcs, it was difficult to obtain accurate R_1 values at lower temperatures and hence the temperature dependence of the conductivity was not analyzed. The conductivity of the plate at 500 °C calculated from R_1 was ~1.4×10^{-5} S cm^{-1}, while Amezawa *et al*. reported a value of 8.2×10^{-5} S cm^{-1} for "5% Sr-doped LaP_3O_9" [4]. For

clarifying the reason for this difference as well as the effects of Sr doping level, grain size, and crystallographic orientation on the conduction properties, further experiments with sufficient reproducibility need to be carried out in future work.

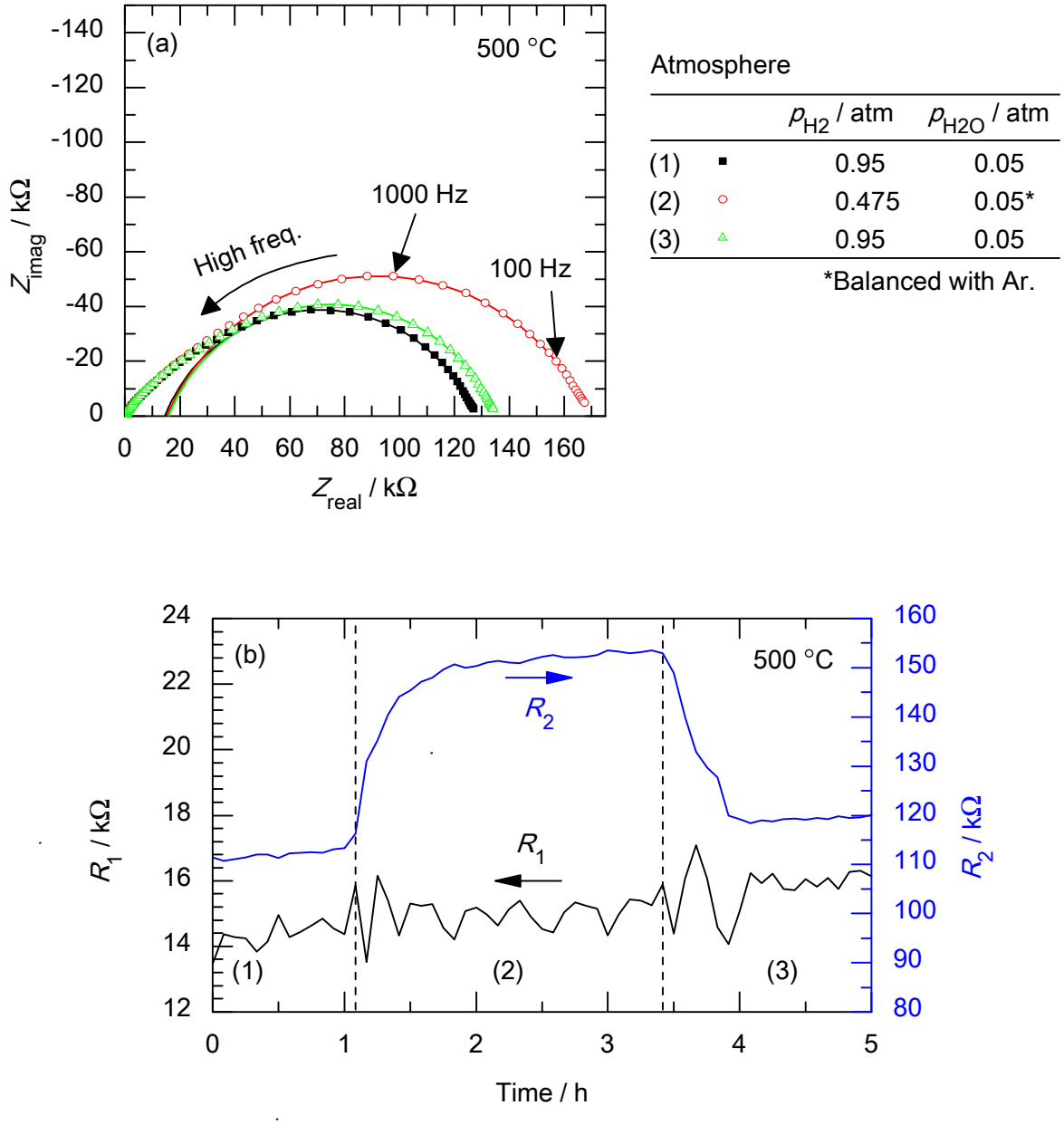

Figure 6.11 (a) Impedance spectra of a polycrystalline plate of Sr-doped LaP_3O_9 at 500 °C under various atmospheres ((1)-(3)). Solid lines are the fitted curves to the low-frequency arc using an equivalent circuit model (R_1)(R_2Q_2) where *R* is a resistor and *Q* is a constant phase element. R_1 and R_2 represent the resistances corresponding to the high- and low-frequency arcs. (b) Time dependence of the resistance of Sr-doped LaP_3O_9 at 500 °C under various atmospheres.

6.3.2.3 Sr-doped LaP_3O_9 Single Crystals

Figure 6.12 shows the impedance spectra of a Sr-doped LaP_3O_9 single crystal measured along the c-axis at 500 °C with different hydrogen partial pressures. Two impedance arcs were identified as was the case for Sr-doped $LaPO_4$ and LaP_3O_9 plates. The resistances corresponding to the high- and low-frequency arcs, R_1 and R_2, showed analogous dependences on hydrogen partial pressure to those observed for Sr-doped $LaPO_4$ and LaP_3O_9 plates: While R_1 remained constant, R_2 increased with decreasing hydrogen partial pressure. The variation in R_2 fits well to Eq. (6.5) with an α value of ~0.49. For these reasons, R_1 and R_2 can be assigned to the electrolyte resistance and charge transfer resistance, respectively. The impedance spectra measured in the ab plane also exhibited two arcs and the resistance corresponding to the high-frequency arc was taken as the electrolyte resistance.

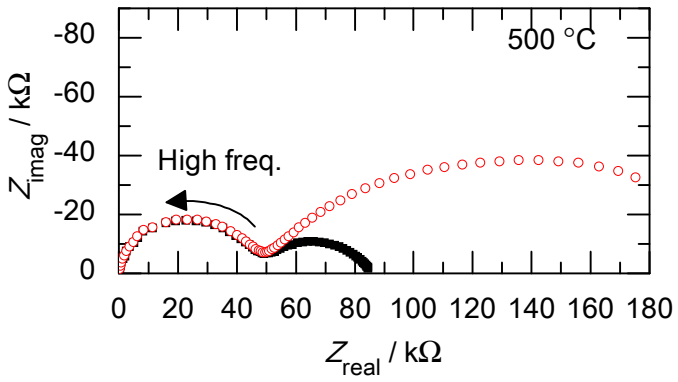

Atmosphere		p_{H2} / atm	p_{H2O} / atm
(1)	■	0.95	0.05
(2)	○	0.05	0.05*

*Balanced with Ar.

Figure 6.12 (a) Impedance spectra of a Sr-doped LaP_3O_9 single crystal measured along the c-axis at 500 °C.

Figure 6.13 shows the temperature dependence of the conductivities of Sr-doped LaP_3O_9 single crystals measured along the c-axis or in the ab plane, using two crystals for each direction. The specific crystallographic directions in the ab plane might be different because they were not identified. All the samples were synthesized in the same crucible. The measured conductivities were distributed over a range of 1 to 5 times the highest values reported by Amezawa *et al*. for Sr-doped LaP_3O_9. The activation energies for charge transport were calculated to be 0.78 ± 0.04 eV at 300–

500 °C and there was no significant dependence on the crystallographic direction. The obtained activation energies were also comparable with the value reported by Amezawa *et al.* for 1% Sr-doped LaP_3O_9 at 300–500 °C (0.84 eV) [5]. On the other hand, the absolute values for the conductivity tended to be higher along the c-axis than in the ab plane, though exact directions in the ab plane were not specified.

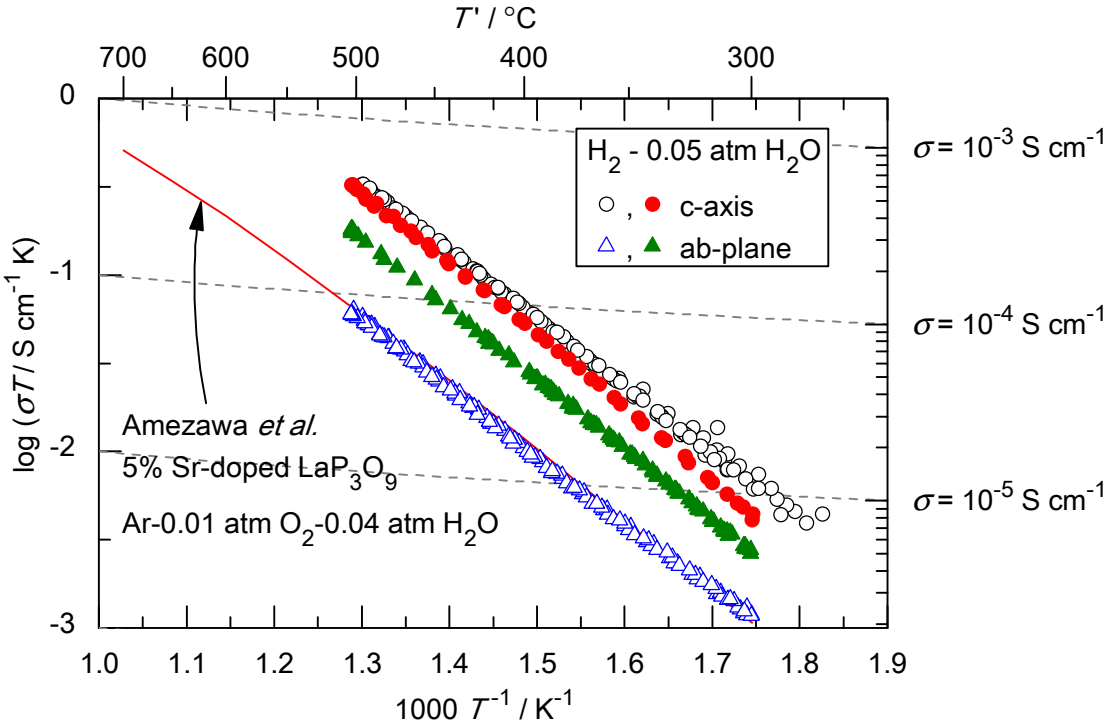

Figure 6.13 Temperature dependence of the conductivity of Sr-doped LaP_3O_9 single crystals.

These results provide a clue to determine the dominant proton conduction paths in Sr-doped LaP_3O_9. In the present measurements, the grain boundary conductivity is considered to be negligible compared with those of polycrystalline samples synthesized by solid state reaction, because the samples were composed of significantly larger crystals (even if they were not perfect single crystals). Therefore, the fact that Sr-doped LaP_3O_9 single crystals exhibited comparable or larger conductivities to those reported for polycrystalline samples suggests that, there are substantial proton conduction paths in the LaP_3O_9 lattice. The observed anisotropy of the conductivity also supports this

idea, since the crystal structure of LaP_3O_9 is highly anisotropic as shown in Chapter 1. If grain boundary conduction were more dominant than bulk conduction in polycrystalline LaP_3O_9, the increase in grain size should lead to the decrease in the conductivity. Thus, the present result would be difficult to be explained. Therefore, it can be concluded that grain growth and orientation control might be a promising strategy for improving the conductivity of Sr-doped LaP_3O_9 electrolytes.

6.4 Conclusions

In this chapter, dense, highly-oriented and coarse-grained polycrystalline plates of highly Sr-doped $LaPO_4$ and LaP_3O_9 were directly synthesized in phosphoric acid solutions by slow cooling or heating of the solutions. The thicknesses of the plates were 150–250 μm. Single crystals of Sr-doped LaP_3O_9 larger than 1 mm were also obtained by slow heating of the solution in the "high-humidity and high-temperature" condition.

The electrical conduction properties of the precipitates were investigated by impedance spectroscopy. For all samples, the resistance corresponding to the proton conduction in electrolytes was identified. It was demonstrated in principle that the Sr-doped $LaPO_4$ and LaP_3O_9 polycrystalline plates, which were directly synthesized in phosphoric acid solutions, also function as proton conducting electrolytes as well as those prepared by solid state reaction in previous studies.

The results on Sr-doped LaP_3O_9 single crystals suggested that there are substantial proton conduction paths in the LaP_3O_9 lattice. Therefore, it can be said that grain growth and orientation control might be a promising strategy for improving the conductivity of Sr-doped LaP_3O_9 electrolytes.

Finally, it should be noted that there is much room for further characterization of the proton conduction properties of Sr-doped $LaPO_4$ and LaP_3O_9 precipitates in terms of reproducibility, effects of doping level and crystallographic direction, and so on.

References

[1] N. Kitamura, K. Amezawa, Y. Tomii, T. Hanada, N. Yamamoto, T. Omata, S. Otsuka-Yao-Matsuo, J. Electrochem. Soc. 152 (2005) A658-A663.

[2] K. Amezawa, H. Maekawa, Y. Tomii, N. Yamamoto, Solid State Ionics 145 (2001) 233-240.

[3] K. Amezawa, Y. Tomii, N. Yamamoto, Solid State Ionics 176 (2005) 143-148.

[4] K. Amezawa, Y. Uchimoto, Y. Tomii, Solid State Ionics 177 (2006) 2407-2411.

[5] K. Amezawa, Y. Kitajima, Y. Tomii, N. Yamamoto, Electrochem. Solid-State Lett. 7 (2004) A511-A514.

Chapter 7
Summary

Lanthanum phosphates are attracting much attention due to their proton conduction. However, further proton conductivity enhancement is desirable, while the proton conduction mechanisms such as the dominant proton conduction paths are still unclear. Their thermodynamic characteristics, which are necessary for evaluating their stabilities, have also been scarce.

In this work, systematic investigations have been carried out to establish the new, low-temperature synthesis method of lanthanum phosphate electrolytes in phosphoric acid solutions. The synthesis method enabled significant increase in Sr doping levels as well as vigorous crystal growth compared with conventional solid state reaction method. This method may serve for revealing the proton conduction mechanisms, and enhancing the proton conductivity. The phase equilibria and thermodynamic properties of the La_2O_3–P_2O_5 system were also characterized and their stabilities were evaluated. Finally, the electrical conduction properties of lanthanum phosphate electrolytes synthesized in phosphoric acid solutions were investigated.

Chapter 2 Synthesis of Lanthanum Phosphates in Phosphoric Acid Solutions

In this chapter, the precipitation conditions of $LaPO_4$, LaP_3O_9, and LaP_5O_{14} in condensed phosphoric acid solutions were established under both atmospheric and humidified conditions. The obtained $LaPO_4$ had the monazite-type structure, which has been reported to exhibit proton conduction. Increasing water vapor pressure from 0.01 atm to 1 atm extended the precipitation regions of $LaPO_4$ and LaP_3O_9 toward higher temperatures by nearly 100 °C. The crystal growth of

$LaPO_4$ was significantly accelerated under such conditions (e.g. T=250 °C and p_{H2O} = 1 atm). The crystal growth of LaP_3O_9 was also promoted moderately by the increase in precipitation temperature. These results will serve as fundamental information for further optimization of growth parameters (*e.g.* temperature profile, precipitation period, and initial composition) and the direct synthesis of dense lanthanum phosphate electrolytes in phosphoric acid solutions.

Chapter 3 Phase Equilibria in the La_2O_3–P_2O_5 System

In this chapter, the phase equilibria in the La_2O_3–P_2O_5 system were re-examined to verify the known phase diagrams. Two intermediate phases, La_3PO_7 and $La_7P_3O_{18}$, were identified in the La_2O_3–$LaPO_4$ subsystem. La_5PO_{10} was not observed. Therefore, the phase diagram reported by Park and Kreidler seems more likely to be accurate in that. La_3PO_7 was formed at 1000 °C, while $La_7P_3O_{18}$ was only formed at 1200 °C and higher. At 1000 °C, neither the formation nor decomposition of $La_7P_3O_{18}$ took place within 1000 h. This behavior might be due to kinetic reasons, though it was not verified. In the $LaPO_4$–LaP_3O_9 subsystem, no intermediate phase such as $La_2P_4O_{13}$ was detected. Based on these results, the most likely representation of the phase diagram is given.

Chapter 4 Thermodynamic Properties of LaP_3O_9 and LaP_5O_{14}

LaP_3O_9 and LaP_5O_{14} have been demonstrated to decompose gradually at high temperatures. However, very little quantitative information is available about the decomposition reactions. In this chapter, for accurate assessment of the stabilities of LaP_3O_9 and LaP_5O_{14}, vapor pressure measurements on LaP_3O_9 and LaP_5O_{14} were carried out by the transpiration method. The equilibrium vapor pressures of P_4O_{10} over LaP_3O_9 and LaP_5O_{14} were obtained to be

$$\log (p_{P4O10} / \text{atm}) = (5.12 \pm 1.00) - (1.22 \pm 0.12) \times 10^4 \times (T / \text{K})^{-1}$$

(over LaP_3O_9, $1123 \leq T / \text{K} \leq 1323$);

$$\log (p_{P4O10} / \text{atm}) = (4.65 \pm 1.80) - (1.00 \pm 0.19) \times 10^4 \times (T / \text{K})^{-1}$$

(over LaP_5O_{14}, $923 \leq T / K \leq 1173$).

The standard enthalpies of the evaporation reactions are given as 117±12 kJ mol^{-1} and 96±18 kJ mol^{-1} in the corresponding temperature ranges. The data were evaluated with respect to the proposed use of LaP_3O_9 and LaP_5O_{14} as solid electrolytes in fuel cells. The maximum operating temperatures for the LaP_3O_9 and LaP_5O_{14} electrolytes were suggested to be about 600 °C and 450 °C in oxygen atmosphere. Taking into account their proton conductivities at these temperatures, it can be said that LaP_3O_9 based electrolytes are more promising than LaP_5O_{14} based ones. In the presence of water vapor or hydrogen, however, decomposition of LaP_3O_9 and LaP_5O_{14} is expected to be accelerated considerably.

Chapter 5 Synthesis of Highly Sr-doped $LaPO_4$ and LaP_3O_9

In Chapter 2, the precipitation conditions for undoped $LaPO_4$ and LaP_3O_9 in homogeneous phosphoric acid solutions were established. In this chapter, further attempts were made to synthesize Sr-doped $LaPO_4$ and LaP_3O_9 in phosphoric acid solutions. The condition dependence of the Sr doping level was analyzed to reveal the optimum condition for obtaining highly Sr-doped phosphates.

The Sr doping level in $LaPO_4$ and LaP_3O_9 depended on the precipitation ratio of La, R_{La}. The Sr doping level gradually decreased with the progression of the precipitation, which was especially noticeable for low Sr concentration solutions. In the case of $LaPO_4$, Sr in the solutions was thought to be exhausted in early stages of the precipitation. However, with high Sr concentrations in the solutions, such as $\left(\frac{Sr}{La+Sr}\right) \geq 20$ mol%, the change in the Sr doping level was relatively small. In such solutions, almost uniformly Sr doped samples are expected to be obtained. The maximum Sr doping levels attained for $LaPO_4$ and LaP_3O_9 were ~23 % and ~14 %, respectively. These values are several times higher than previously reported solubilities of Sr in $LaPO_4$ and LaP_3O_9.

The effectiveness of Sr doping in $LaPO_4$ was verified by observing unit cell volume changes by doping and the evaporation of H_2O which had been incorporated into $LaPO_4$ during the synthesis. Sr partially substituted for La in monazite-type $LaPO_4$ when synthesized in phosphoric acid solutions, as well as by solid state reaction as reported in literature. On synthesis, H_2O was certainly incorporated in the bulk by Sr doping.

The stability of Sr-doped $LaPO_4$ at high temperatures was also investigated. The solubility of Sr in $LaPO_4$ was found to be sufficiently high (at least 20.1 %) even at 600 °C, which is in the operating temperature range for the electrolyte. However, it becomes considerably lower than 13.4 % at 1200 °C. The reason why the solubility of Sr is higher at lower temperatures has not been clarified, but it is possible to speculate that Sr in the $LaPO_4$ lattice is destabilized with evaporation of water at high temperatures.

Chapter 6 Electrical Conduction Properties of Sr-doped $LaPO_4$ and LaP_3O_9

The proton conductivity enhancement in lanthanum phosphates is desirable, while the proton conduction mechanisms are still unclear. In this chapter, dense, plate-like precipitates of Sr-doped $LaPO_4$ and LaP_3O_9 were directly synthesized in phosphoric acid solutions by slow cooling or heating of the solutions. Single crystals of Sr-doped LaP_3O_9 larger than 1 mm were also obtained by slow heating of the solution in the “high-humidity and high-temperature” condition.

The electrical conduction properties of the precipitates were investigated by impedance spectroscopy. For all samples, the resistance corresponding to the proton conduction in electrolytes was identified. It was demonstrated in principle that the Sr-doped $LaPO_4$ and LaP_3O_9 plates which were directly synthesized in a phosphoric acid solutions also function as proton conducting electrolytes as well as those prepared by solid state reaction in previous studies.

The results on Sr-doped LaP_3O_9 single crystals suggested that there are substantial proton

conduction paths in the LaP_3O_9 lattice. Therefore, it can be said that grain growth and orientation control might be a promising strategy for improving the conductivity of Sr-doped LaP_3O_9 electrolytes.

List of Publications

Lanthanum Phosphates

Papers

- "Precipitation Behavior of Highly Sr-doped $LaPO_4$ in Phosphoric Acid Solutions"
  Naoyuki Hatada, Yoshitaro Nose, Akiko Kuramitsu, and Tetsuya Uda,
  J. Mater. Chem. 21 (2011) 8781-8786.
- "First-principles Thermodynamics of La_2O_3-P_2O_5 Pseudobinary System"
  Kazuaki Toyoura, Naoyuki Hatada, Yoshitaro Nose, Tetsuya Uda, and Isao Tanaka,
  Phys. Rev. B 84 (2011) 184301.
- "Phase Equilibria in the La_2O_3–P_2O_5 System"
  Naoyuki Hatada, Takashi Nagai, Yoshitaro Nose, and Tetsuya Uda,
  (in preparation).
- "Vapor Pressure Measurements on Lanthanum Polyphosphate and Ultraphosphate by Transpiration Method"
  Naoyuki Hatada, Kazuaki Toyoura, Yoshitaro Nose, and Tetsuya Uda,
  (in preparation).
- "Crystal Growth of LaP_3O_9 in phosphoric acid solutions"
  Takayuki Onishi, Naoyuki Hatada, Yoshitaro Nose, and Tetsuya Uda,
  (in preparation).
- "High proton conduction in heavily Sr-doped LaP_3O_9 single crystals"
  Naoyuki Hatada, Takayuki Onishi, Kazuaki Toyoura, Yoshitaro Nose, and Tetsuya Uda,
  (in preparation).

Oral Presentations

International Conferences

- "Synthesis of Lanthanum Polyphosphate in Condensed Phosphoric Acid Solutions"

  Naoyuki Hatada, Yoshitaro Nose, and Tetsuya Uda,

  Joint Symposium on Materials Science and Engineering for the 21st Century, Kyoto, Japan, September, 2009.

- "Synthesis of Lanthanum Orthophosphate and Polyphosphate in Condensed Phosphoric Acid Solutions"

  Naoyuki Hatada, Yoshitaro Nose, and Tetsuya Uda,

  2010 TMS Annual Meeting & Exhibition, Seattle, USA, February, 2010.

- "Synthesis of Highly Sr-doped Lanthanum Orthophosphate and Polyphosphate in Phosphoric Acid Solutions"

  Naoyuki Hatada, Akiko Kuramitsu, Yoshitaro Nose, and Tetsuya Uda,

  The 15th International Conference on Solid State Protonic Conductors, Santa Barbara, USA, August, 2010.

- "Synthesis of Sr-doped LaP_3O_9 Films in Phosphoric Acid Solutions and Their Proton Conduction Properties"

  Takayuki Onishi, Naoyuki Hatada, Kazuaki Toyoura, Yoshitaro Nose, and Tetsuya Uda,

  2011 TMS Annual Meeting & Exhibition, San Diego, USA, March, 2011.

- "Thermal Stability of LaP_3O_9 and LaP_5O_{14} Proton Conductors"

  Naoyuki Hatada, Kazuaki Toyoura, Yoshitaro Nose, and Tetsuya Uda,

  62nd Annual Meeting of the International Society of Electrochemistry, Niigata, Japan, September, 2011.

Domestic Conferences in Japan

- "Synthesis of Lanthanum Polyphosphate Crystals in High-Temperature Phosphoric Acid Solutions"

  Naoyuki Hatada, Yoshitaro Nose, and Tetsuya Uda,

  2009 Fall Meeting of the Japan Institute of Metals, Kyoto, September, 2009.

- "Synthesis of Sr-doped $LaPO_4$ in Phosphoric Acid Solutions under Atmospheric and Humidified Conditions"

  Naoyuki Hatada, Takahito Nakajima, Yoshitaro Nose, and Tetsuya Uda,

  2010 Spring Meeting of the Japan Institute of Metals, Tsukuba, March, 2010.

- "High Sr Doping of $LaPO_4$ and LaP_3O_9 by Synthesis in Phosphoric Acid Solutions"

  Naoyuki Hatada, Akiko Kuramitsu, Yoshitaro Nose, and Tetsuya Uda,

  2010 Fall Meeting of the Mining and Materials Processing Institute of Japan, Fukuoka, September, 2010.

- "Dependence of the Sr-doping level in $LaPO_4$ Precipitated in Phosphoric Acid Solutions on the Precipitation Ratio of La and Direct Synthesis of Plate-like Electrolytes"

  Naoyuki Hatada, Akiko Kuramitsu, Yoshitaro Nose, and Tetsuya Uda,

  The 36th Symposium on Solid State Ionics in Japan, Sendai, November, 2010.

- "Proton Migration Mechanism in LaP_3O_9 – A First Principle Study"

  Kazuaki Toyoura, Naoyuki Hatada, Takayuki Onishi, Yoshitaro Nose, and Tetsuya Uda,

  The 36th Symposium on Solid State Ionics in Japan, Sendai, November, 2010.

- "Synthesis of Sr-doped LaP_3O_9 in Condensed Phosphoric Acid Solutions and Its Electrical Conductivity"

  Takayuki Onishi, Naoyuki Hatada, Kazuaki Toyoura, Yoshitaro Nose, and Tetsuya Uda,

  The 7th Symposium for Young Researchers and Students of the Kansai Branch of the Mining and Materials Processing Institute of Japan, Kyoto, November, 2010.

- "Crystal Structures and Proton Conductivities in Lanthanum Phosphates"

  Kazuaki Toyoura, Naoyuki Hatada, Yoshitaro Nose, and Tetsuya Uda,

  The 78th Meeting of the Electrochemical Society of Japan, Yokohama, March, 2011 (cancelled).

- "Investigation of the Thermal Stabilities of Proton Conductors LaP_3O_9 and LaP_5O_{14} by Transpiration Method"

  Naoyuki Hatada, Kazuaki Toyoura, Yoshitaro Nose, and Tetsuya Uda,

  2011 Fall Meeting of the Mining and Materials Processing Institute of Japan, Sakai (Osaka), September, 2011.

- "Evaluation of the Thermodynamic Properties of LaP_3O_9 and LaP_5O_{14} by Third-Law Analysis"

  Naoyuki Hatada, Kazuaki Toyoura, Yoshitaro Nose, and Tetsuya Uda,

  2012 Spring Meeting of the Mining and Materials Processing Institute of Japan, Tokyo, March, 2012.

- "Phase Stabilities of the La_2O_3 – P_2O_5 Pseudo-Binary System Based on First Principle Thermodynamics"

  Kazuaki Toyoura, Naoyuki Hatada, Yoshitaro Nose, Tetsuya Uda, and Isao Tanaka,

  2012 Spring Meeting of the Japan Institute of Metals, Yokohama, March, 2012.

- "Evaluation of the Proton Conduction Properties of Sr-doped Lanthanum Polyphosphate Using Single Crystals"

  Takayuki Onishi, Naoyuki Hatada, Akiko Kuramitsu, Yoshitaro Nose, and Tetsuya Uda

  The 79th Meeting of the Electrochemical Society of Japan, Hamamatsu, March, 2012.

Poster Presentations

International Conferences

- "Synthesis of Lanthanum Polyphosphate Single Crystals"

  Naoyuki Hatada, Tetsuya Uda, Yoshitaro Nose, and Yasuhiro Awakura,

  Joint Symposium on Materials Science and Engineering for the 21st Century, Gyeongju, Republic of Korea, September, 2008.

- "Synthesis of Highly Sr-doped Lanthanum Orthophosphate in Phosphoric Acid Solutions"

  Naoyuki Hatada, Akiko Kuramitsu, Yoshitaro Nose, and Tetsuya Uda,

  Joint Symposium on Materials Science and Engineering for the 21st Century, Daejeon, Republic of Korea, June, 2010.

- "Vapor Pressure Measurements on LaP_3O_9 by the Transpiration Technique"

  Naoyuki Hatada, Yoshitaro Nose, and Tetsuya Uda,

  Joint Symposium on Materials Science and Engineering for the 21st Century, Singapore, June, 2011.

- "Correlation between Crystal Structures and Proton Conduction in Lanthanum Phosphates - A First Principles Study"

  Kazuaki Toyoura, Naoyuki Hatada, Yoshitaro Nose, and Tetsuya Uda,

  2011 MRS Fall Meeting & Exhibit, Boston, USA, November, 2011.

Trirubidium Hydrogen Bisulfate, $Rb_3H(SO_4)_2$

Paper

- "High Temperature Properties of $Rb_3H(SO_4)_2$ at Ambient Pressure: Absence of a Polymorphic, Superprotonic Transition"

  Lisa A. Cowan, Riham M. Morcos, Naoyuki Hatada, Alexandra Navrotsky, and Sossina M. Haile, Solid State Ionics 179 (2008) 305-313.

Cesium Metaphosphate, $CsPO_3$

Paper

- "Phase Relationship of CsH_2PO_4-$CsPO_3$ System and Electrical Properties of $CsPO_3$"

  Yu-ki Taninouchi, Naoyuki Hatada, Tetsuya Uda, and Yasuhiro Awakura,

  J. Electrochem. Soc. 156 (5) (2009) B572-B579.

Oral Presentation

Domestic Conference in Japan

- "Electrical conductivity and phase stability of dehydrated liquid of CsH_2PO_4"

  Yu-ki Taninouchi, Naoyuki Hatada, Tetsuya Uda, and Yasuhiro Awakura,

  The 74th Meeting of the Electrochemical Society of Japan, Noda (Chiba), March, 2007.

Poster Presentation

Domestic Conference in Japan

- "Electrical Conductivity Mechanism of Cesium Metaphosphate"

  Naoyuki Hatada, Yu-ki Taninouchi, Tetsuya Uda, and Yasuhiro Awakura,

  The 74th Meeting of the Electrochemical Society of Japan, Noda (Chiba), March, 2007.

Acknowledgments

This work was financially supported by MEXT Elements Science and Technology Project and a Grant-in-Aid for JSPS Fellows.

I would like to express my sincere gratitude to my advisor, Prof. Tetsuya Uda, for all of his guidance and support throughout the project. I would also like to express my gratitude to Prof. Yoshitaro Nose for valuable discussions and continuous encouragement. I am grateful to Prof. Isao Tanaka and Prof. Haruyuki Inui for reading my thesis.

I would like to thank Dr. Takashi Nagai at the University of Tokyo for useful discussions on thermodynamics, and Dr. Harumi Yokokawa at AIST for his valuable suggestions.

I am grateful to Mr. Tokuji Tanaka for his technical assistance, and Ms. Akiko Kuramitsu for sample preparation and analysis. I am thankful to Ms. Keiko Matsumoto for her help with daily affairs.

I am grateful to Dr. Kazuaki Toyoura, Dr. Yu-ki Taninouchi, Dr. Hidehiro Sekimoto, and Dr. Donglin Han for valuable discussions and advice. I would like to thank Mr. Takayuki Onishi, Mr. Tatsuya Miyazaki, Mr. Takahito Nakajima, Mr. Yohei Noda, Mr. Yoshinobu Adachi, and Mr. Akifumi Sumitani for their helpful assistance and useful discussions. Also, I would like to express my gratitude to all the members in Prof. Uda's group.

I am very grateful to Prof. Yasuhiro Awakura and Prof. Kazuhiro Matsuda for providing kind advice regarding my career before I started my doctoral work.

Lastly, this thesis would not have been possible without the continuous support and understanding of my family. I owe my deepest gratitude to my parents Fumio Hatada and Setsuko Hatada, and my sister Yuiko Hatada.